UNIVERSITY OF CALIFORNIA SAN DIEGO

Transient Dynamic Analysis of Modified Hopkinson Pressure Bar System for High Strain Rate Tensile Testing

A thesis submitted in partial satisfaction of the

Requirements for the degree Master of Science

in

Structural Engineering

by

John-Paul Laurente Pascua

Committee in charge:

Professor Hyonny Kim, Chair
Professor Petr Krysl
Professor Georgios Tsampras

2022

The thesis of John-Paul Laurente Pascua is approved, and it is acceptable in quality and form for publication on microfilm and electronically.

University of California San Diego

2022

TABLE OF CONTENTS

LIST OF FIGURES

LIST OF TABLES

ACKNOWLEDGEMENTS

I would like to thank my advisor, Professor Hyonny Kim, for the opportunity to be a part of his research group. While I was an undergraduate his passion for teaching aerospace structures inspired me to become an aerospace structures engineer. I am also forever grateful for his continued support and kindness throughout my master's program, as well as the doors he has opened for me towards my professional career.

I would also like to acknowledge Professor Daniel Whisler at California State University, Long Beach, for providing me with the additional resources and insight needed to carry out the presented work. His guidance in a time of remote instruction has been invaluable in helping me understand my research much more clearly. Chapter 5 of this thesis has been written with the aid of unpublished SOLIDWORKS material provided by Professor Whisler.

Thank you to Professor Petr Krysl and Professor Georgios Tsampras for being a part of my thesis committee as well. I have had the opportunity to learn various structural engineering concepts through them that have benefitted me throughout this project.

Finally, I want to thank my family and friends for their encouragement and support throughout my time at the University of California, San Diego.

ABSTRACT OF THE THESIS

Transient Dynamic Analysis of Modified Hopkinson Pressure Bar System for High Strain Rate Tensile Testing

by

John-Paul Laurente Pascua

Master of Science in Structural Engineering

University of California San Diego, 2022

Professor Hyonny Kim, Chair

High strain rate testing of specimens within a split Hopkinson pressure bar (SHPB) is a well-established experimental technique used to quantify the compressive properties of materials in high impact events. The aim of this thesis is to investigate high strain rate tensile testing of materials utilizing a modified Hopkinson pressure bar system containing a tension yoke that deforms a test specimen by impacting the yoke strike plate and converting the incident

compression wave into tension loading through the specimen. Credence towards the proposed design is built utilizing various finite element benchmark models and verification against the principles of SHPB systems is conducted using computational analysis to quantify the feasibility and performance of the system. Results show that the strain response in the Hopkinson pressure bar shows a strong correlation to the strain response in the test specimen, as assessed via comparison of peak forces and observing relatively low difference between the two quantities. Following this, effects of dispersion are explored further by modifying the impacting pulse shape and comparing results between different pulse shapes. Final stages of analysis reveal that momentum of the tension yoke largely affects the strain response of the tensile specimen relative to the applied pulse. However, the strong correlation of the force pulse developed within the tensile specimen and the force pulse transmitted into the Hopkinson bar remains very consistent, showing the potential of the proposed apparatus design to be used as a functional experimental system for converting impact into high strain rate tensile loading.

Chapter 1

Introduction

1.1 Background

One of the most traditional methods of quantifying material properties is through loading test specimens within the Split Hopkinson Pressure Bar (SHPB) system, which is shown in Figure 1.1 [1]. A detailed overview of the SHPB system is given in Chapter 2.

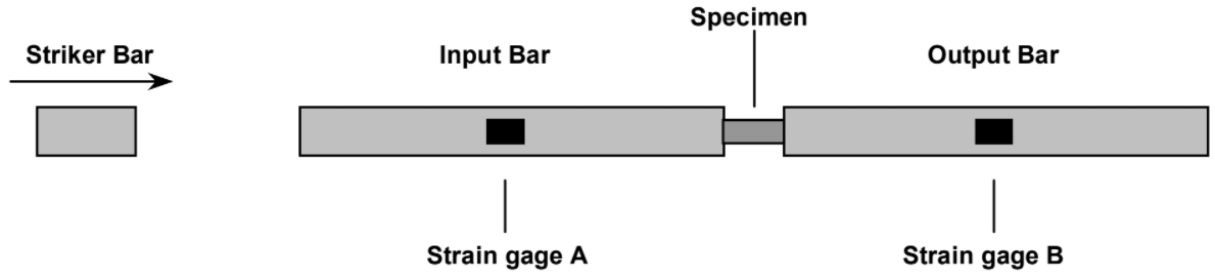

Figure 1.1 Split Hopkinson Pressure Bar System [1]

The purpose of the system is to determine the stress-strain response of various materials loaded at high strain rates [1]. High strain rates are commonly observed in structures that experience short-duration, high-intensity impact events, such as those observed in the strike of a baseball with a bat or a high-speed car collision. These types of events create a large amount of plastic deformation within the affected structures.

In contrast to dynamic compressive events, dynamic tensile events are not as prevalent. However, one example can be observed on aircraft carriers through the deployment of arresting

cables that decelerate high-speed aircraft, thereby allowing the aircraft to land safely on the carrier deck. A schematic of this equipment is shown in Figure 1.2 [2].

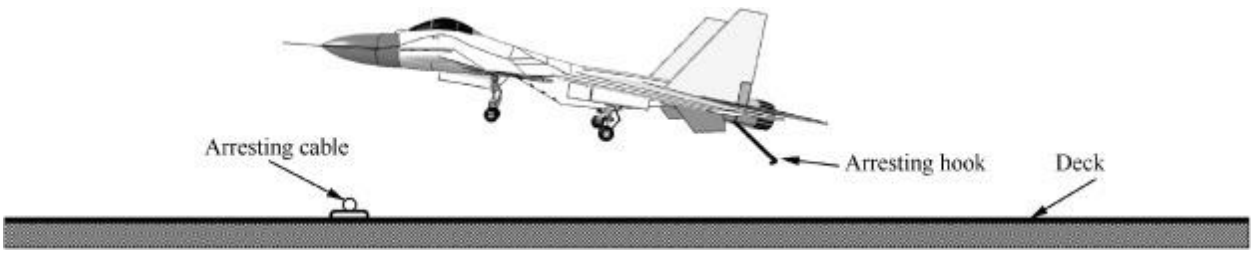

Figure 1.2 Arresting Hook and Cable Schematic on an Aircraft Carrier [2]

At high magnitudes of loading critical failure of either component can occur. This can cause the aircraft to lose stability when landing and can pose safety issues. In addition, if the cable were to snap, it can injure carrier deck workers. With the arresting hook and cable equipment in mind, quantifying the tensile properties of materials under similar high-speed conditions has been a topic of interest that remains an ongoing development today, with the goal of developing an intuitive and reliable experimental setup that can quantify the constitutive behavior of materials under these tensile conditions. Substantial study of these materials will enable the manufacturing of optimally designed components that experience high rates of strain to promote safety in the various applications they are used in [3].

1.2 Current Advancements in High Strain Rate Tensile Testing

The SHPB system is traditionally used to determine the high strain rate behavior of various materials in compression. Various technologies have been developed and analyzed that instead produce tension at high strain rates using the traditional SHPB as a referential design. Harding et

al [4] presented a tensile specimen test assembly that utilized a hollow tube containing an inner inertia bar, which were both connected by a thin specimen. Impacting the hollow tube would propagate a compression wave to the opposite end of the tube, creating tension within the specimen due to the wave reflection off the end. Staab and Gilat [5] developed a direct-tension split Hopkinson bar apparatus that induces tensile loading by utilizing a vise clamp that holds and releases the load an instant later. Zhou et al [6,7] developed an apparatus that utilizes compressive piston action to push into a rubber sleeve. A material ring is wrapped over the sleeve and the piston action radially expands the rubber sleeve, expanding the material ring itself in tension. Nicholas [8] and Ellwood et al [9] both present a modified SHPB system with a collar that surrounds the test specimen and is squeezed between the incident bar and transmitter bar. The test specimen is affixed by threading its ends into each bar. Striking the incident bar sends the compressive pulse from the bar through the collar and into the transmitter bar, effectively propagating past the specimen. Once the pulse reaches the free end of the transmitter bar, the induced tension pushes the transmitter bar forward, loosening the collar and thereby creating tension within the specimen [8]. Lindholm and Yeakley [10] introduce a hollow, hat-shaped specimen fitted between an incident bar and transmitter bar in another modified SHPB system. The specimen is hollow on one end, which is fixed on its outer surfaces against another fixture. The incident bar creates tension by striking the inside bottom rim of the specimen with the incident bar, pushing the specimen in tension, and transferring the pulse through the transmitter bar. Ogawa [11] presents another modified SHPB system utilizing a step-shaped anvil that can create a sequence of tension and compression within a specimen.

The technologies developed by these groups of researchers present novel methodologies of high strain rate tensile testing. Despite these advancements, some of these innovations involve

complex assemblies of several components which could lead to various issues. Some of the aforementioned designs present the use of components such as inertia bars or anvils which could create unwanted oscillations from the inertias of these components clashing with the inertia of the specimen, thus creating an unreliable wave signal [12]. Other designs present the use of multi-step loading conditions to convert compression into tension by having the wave propagate through a complex series of components, which could lead to increased chance of dispersion, eccentricity, or signal loss during data acquisition. Other innovations showed potential due to minimal modification of the existing SHPB system, which present a sense of familiarity with the traditional experimental testing setup. However, these innovations could be developed further by reducing the number of components, which would simplify the experimental testing setup. They could also be developed further by simplifying the loading conditions, the analytical methods, and by determining ways to reduce wave signal interference. Campbell [12] suggests that reducing burden on the system by reducing the number of components and simply leveraging the inertia of the specimen itself to generate stress waves can lead to improvements in data acquisition and accuracy of postprocessed results. Therefore, the aim of this research is to study the performance of a proposed modified Hopkinson pressure bar system that could simplify the experimental setup, loading conditions, and data acquisition methods, therefore improving upon the accuracy of the tensile forces developed in the test specimen as determined from high strain rate tensile testing.

Chapter 2

Literature Review

2.1 Early Developments of Measuring Impact Effects on Materials

The pioneer of the Hopkinson bar which was used to measure the response of materials under high-intensity impact events was John Hopkinson. In 1872, he observed that stress waves can be generated by fixing one end of an iron wire and impacting the opposite end with a moving mass [3,13-14]. His work was continued by Bertram Hopkinson in 1914, who theorized that impacting a cylindrical steel rod with a rifle bullet or mild explosive such as guncotton (nitrocellulose) imparts a compressive pressure wave through the rod at the velocity of sound [3]. The wave propagates to the opposite end of the rod and reflects back to the impacted end as a tension wave. From this information, the pressure at any point along the rod could be determined by summing the effects of the initial pressure wave and reflected wave [15]. Despite these observations, technology at the time was not reliable enough to collect data of the pressure waves experienced by the steel rod.

Even before the physical experiments conducted by Bertram Hopkinson, major figures such as Ludwig Pochhammer (1876) [16,21,26], John William Strut, 3rd Baron Rayleigh (1885) [17], Charles Chree (1886, 1889) [18-21], and Augustus Edward Hough Love (1911) [22-23,26] spearheaded the development of theory surrounding wave propagation in elastic solids, with later contributors such as Dennison Bancroft (1941) [21,24,26] and Jan Drews Achenbach (1971) [25] furthering the development of spectral analysis and wave propagation theory.

Following the Hopkinsons' initial discoveries, Rhisiart Morgan Davies (1948) developed a reliable method of collecting data to model the relationship between the pressure and time [21,26-27]. By rigging the cylindrical steel rod with electrical condenser units, impacting the steel rod in a similar manner to Hopkinsons' experimental setups causes the condenser units to capture the pressure waves as electrical signals. These waves can then be converted into a waveform signal displayed through a cathode ray oscilloscope [26]. Davies theorized that the recorded pressure waves the stress on the pressure bar was proportional to the displacement of the bar [26-27]. He additionally quantified the effects of dispersion, which is explained in the next section.

Herbert Kolsky (1949) followed up on the developments of both Davies and the Hopkinsons by devising the traditional split Hopkinson pressure bar system commonly seen today. Kolsky simply pressed a specimen of interest between two Hopkinson bars, then impacted one of the bars. By using similar condenser units to Davies, Kolsky was able to measure and derive equations governing the stress-strain response of the specimen by extracting the waveform data from the two Hopkinson bars using a cathode ray oscillograph [26,28-29].

Furthering this development were Krafft, Sullivan, and Tipper (1954), who implemented the use of strain gauges to study the yield stress of mild steel with compression in a similar Hopkinson bar system [30]. By measuring the voltage of the strain gauges attached to the system, the changes in a specimen's cross-sectional area and its length can be fully described. This technology eventually became a staple in experiments involving Hopkinson bar setups due to its reliability in collecting waveform data and accurate data representation [30]. Over the years, the split Hopkinson pressure bar system, with the implementation of attached strain gauges, became the standard of testing the stress-strain response of materials by inducing high strain rate compression through impact.

2.2 Principles of the Split Hopkinson Pressure Bar System

Due to its extensive historical development, the split Hopkinson pressure bar (SHPB) system is the most traditional experimental setup used for testing materials under the influence of dynamic, high-speed compressive impacts. A schematic of a typical SHPB system is shown labeled with its base components in Figure 2.1 [31].

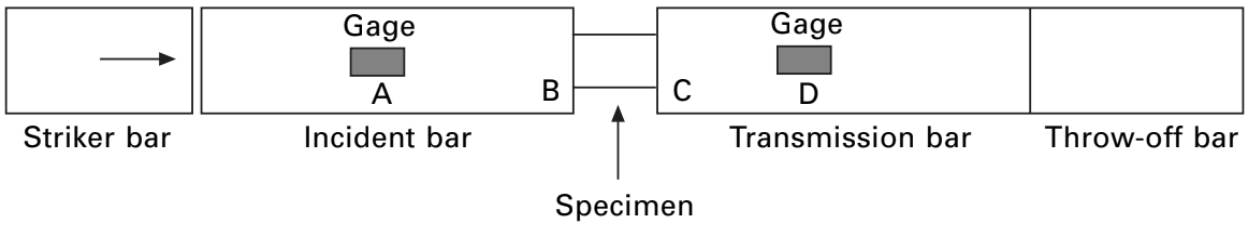

Figure 2.1 Schematic of Split Hopkinson Pressure Bar System [31]

Figure 2.1 shows a horizontal stack of various bars that are typically composed of the same material and of relatively the same size and shape. Two strain gauges are mounted, with one placed on the incident bar and the other on the transmission bar, and a specimen is pressed between the two. An impact event is created by striking the free end of the incident bar with the striker bar. A compressive waveform propagates through the incident bar, which causes the bar to compress the specimen, even plastically deforming it. A fraction of the waveform in the incident bar reflects from the incident bar and specimen interface back to the free end of the incident bar, while another fraction of the waveform propagates through the specimen and into the transmission bar. The transmission bar is then stopped by a throw-off bar or stopping block. As a result of the impact, several waveforms are captured by the strain gauges: an incident pulse and reflected pulse in the incident bar, and then a transmitted pulse and reflection of the transmitted pulse in the transmission bar, though the first three pulses are of most significance.

The system utilizes the constitutive stress-strain relationship of materials and one-dimensional wave propagation to measure the material behavior of the compressed specimen [3,26]. To accurately portray the wave propagation behavior, various assumptions and conditions must be made. Firstly, the Hopkinson bars are typically designed to have a length-to-diameter ratio greater than 10 [26], though some setups use ratios of 80 or more [1]. Once the length-to-diameter ratio is acceptable, the propagating waves are assumed to travel in only one direction [26]. Another assumption is that the bar materials are assumed to behave purely elastically, which allows the theory explored in the following sections to hold [26].

There are several consequences of dynamic loading. Though elastic assumptions are made for analytical purposes, materials under high strain rates almost never behave elastically, and impacts within SHPB systems cause materials to undergo large plastic deformation, which leads to specimen failure [32]. This causes imperfect waveforms to be captured by equipment such as oscilloscopes, making the wave signals appear noisy. Another consequence of dynamic loading is a phenomenon known as dispersion. This effect is caused by a waveform's velocity dependence on frequency [26-27]. Impacting the incident bar causes the bar to oscillate wildly, which excites various frequencies and leads to waves propagating at different velocities within the incident bar [26-27]. These frequencies also reduce the quality of the wave signals, making the strain gauges record a waveform that appears squiggly instead of looking like a clean, noise-free wave. Finally, another issue is eccentricity, which is the distance off the intended line of action where a load is applied. This also generates undesirable wave signals due to a loss in axiality of loading [12]. To alleviate this issue, various fixtures are used to mount the striker bars and align them. Additional measures can be taken to ensure striking projectiles are also aligned so that the impact occurs along the intended line of action.

2.2.1 Stress-Strain Response

Several strains are recorded by the strain gauges that are converted to obtain constitutive material behavior. First, when the incident wave passes the incident bar's strain gauge, an incident strain, ε_i, is recorded. The waveform then approaches the interface between the incident bar and specimen and reflects to the first strain gauge, recording a reflected strain, ε_r. The time it takes for the wave to reflect to the strain gauge is denoted by a time interval, Δt_{AB}. Thus, the two strain waves at any time can be represented as an overall incident bar strain, ε_I, which is treated as a function of time with either a subtraction or addition of the time interval Δt_{AB} [31].

$$\varepsilon_i = \varepsilon_I(t - \Delta t_{AB}) \tag{1}$$

$$\varepsilon_r = \varepsilon_I(t + \Delta t_{AB}) \tag{2}$$

Similarly, the transmitted strain, ε_t, can be represented as a function of the overall transmission bar strain, ε_T, which is treated as a function of time with an added time interval, Δt_{CD}, which is the time it takes for the wave to travel from the specimen and transmission bar interface to the strain gauge on the transmission bar [31].

$$\varepsilon_t = \varepsilon_T(t + \Delta t_{CD}) \tag{3}$$

With the three strains recorded, the stresses in the incident bar and transmission bar can be calculated using Equations (4) and (5), respectively. In these equations, E_I and E_T represent the Young's modulus of the incident bar and transmission bar, respectively [3,9,29,32-33].

$$\sigma_I = E_I(\varepsilon_i + \varepsilon_r) \tag{4}$$

$$\sigma_T = E_T\varepsilon_t \tag{5}$$

Utilizing the simple stress formulation of $\sigma = P/A$, the loads at the two interfaces at locations B and C in Figure 2.1 can be calculated with Equations (6) and (7), respectively. The

variables A_I and A_T represent the cross-sectional areas of the incident bar and transmission bar, respectively [1,3,9,29,31-33].

$$P_I = E_I A_I(\varepsilon_i + \varepsilon_r) \tag{6}$$

$$P_T = E_T A_T \varepsilon_t \tag{7}$$

For the equations to hold, assuming purely elastic behavior, the system must be in a state of stress equilibrium such that one of the following equivalence conditions are met [1,3,10,32]:

$$P_I \cong P_T \qquad OR \qquad \varepsilon_i + \varepsilon_r \cong \varepsilon_t. \tag{8}$$

The equivalence conditions state that either the forces in the incident and transmission bars must be equal or the sum of the incident strain and reflected strain equates to the transmitted strain. These conditions can be easily verified by summing the appropriate strains detected or by converting them to forces and summing the forces [10].

Finally, the strain within the specimen can be converted into a stress, σ_s, using the constitutive stress-strain relationship shown in Equation (9). Here, E_s and A_s represent the Young's modulus and cross-sectional area of the specimen, respectively. In many SHPB experiments, the gauge area is treated as the cross-sectional area of the specimen, assuming a specimen of non-uniform area is used in testing [1,3,33].

$$\sigma_s = E_s \frac{A_T}{A_s} \varepsilon_T \tag{9}$$

2.2.2 Wave Propagation in Elastically Isotropic Materials

In addition to the constitutive stress-strain response of the materials shown in the previous section, wave propagation theory is utilized to determine the direct waveform behavior as it propagates through the system. By taking an infinitesimal element, the stress-strain relationship within the element can be derived utilizing the diagram in Figure 2.2 [25].

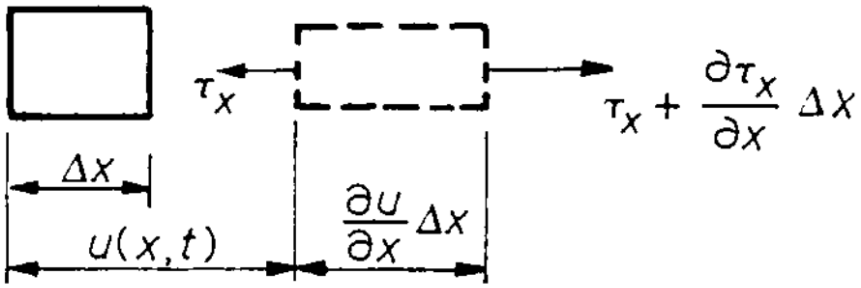

Figure 2.2 Infinitesimal Element in Uni-Axial Stress [25]

Under uni-axial stress conditions, the element is assumed to only deform in one direction, which is the x-direction in this case. Neglecting transverse deformation effects, the stress-strain relationship is defined as

$$\tau_x = E\varepsilon_x, \tag{10}$$

where E is the Young's modulus of the element [25]. Rewriting this relationship in terms of its corresponding equation of motion yields the following relationship:

$$\frac{\partial \tau_x}{\partial x} = \rho \frac{\partial^2 u}{\partial x^2}, \tag{11}$$

where ρ represents the material mass density [25]. Substituting Equation (10) into (11) gives

$$E \frac{\partial^2 u}{\partial x^2} = \rho \frac{\partial^2 u}{\partial t^2}, \tag{12}$$

and by rearranging Equation (12), the relationship of interest in Equation (13) is obtained [1,25,32].

$$C_o^2 \frac{\partial^2 u}{\partial x^2} = \frac{\partial^2 u}{\partial t^2} \tag{13}$$

The parameter C_o specifies the velocity of the propagating waveform through the element, which is explicitly calculated using Equation (14), which states that the wave velocity is the radical of the Young's modulus of the material divided by the material mass density [1,25,32-33].

$$C_o = \sqrt{\frac{E}{\rho}} \tag{14}$$

With the theory of SHPB systems derived, benchmark models in the next chapter will be designed and analyzed. The theory will be adapted for the modified SHPB design explored in this paper to verify and build credence on the principles of the traditional SHPB system.

Chapter 3

Benchmark Modeling and Analysis

3.1 Objective

To gain an understanding of the wave propagation behavior and stress-strain behavior in a tension-based Hopkinson bar system from a finite element analysis standpoint, various models of simpler geometry were developed and analyzed within Abaqus. This chapter describes the analyzed benchmark models and discusses the results of each analysis to build confidence in the analyses conducted in Chapter 6.

3.2 Finite Element Models

Three benchmark models that represent components of interest in the modified Hopkinson bar system were designed. The first model developed was a solid cylindrical bar with a radius of 1.5 inches and an extruded length of 10.5 feet (126 inches), which yielded a length-to-diameter ratio of 84. The solid bar model is shown in Figure 3.1.

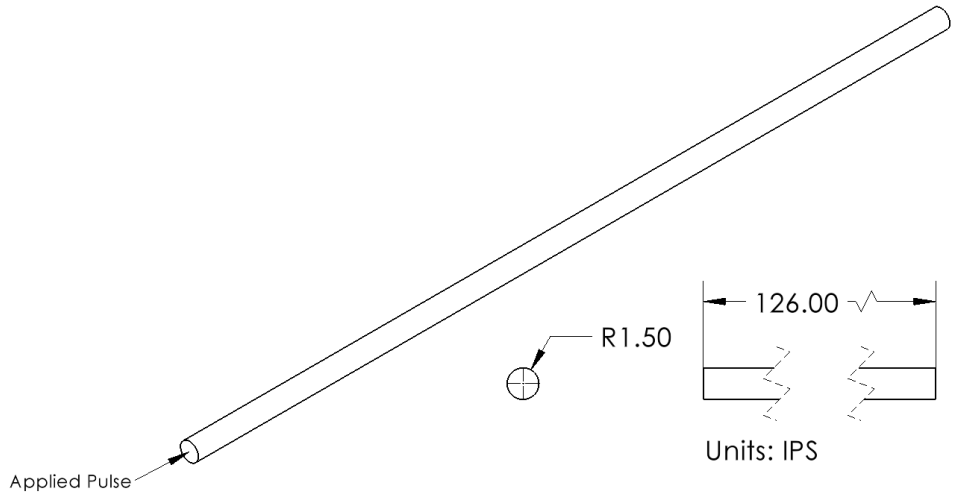

Figure 3.1 Solid Cylindrical Bar

The second benchmark model was composed of a 1-inch-thick end cap with a radius of 1.5 inches assembled to a 10.5-foot hollow cylindrical bar. The bar had an inner radius of 1.25 inches and an outer radius of 1.5 inches, yielding a wall thickness of 0.25 inches. This model is shown in Figure 3.2. The two cylindrical bar models were designed to test the elastic wave response of an applied impact with a specified pulse shape.

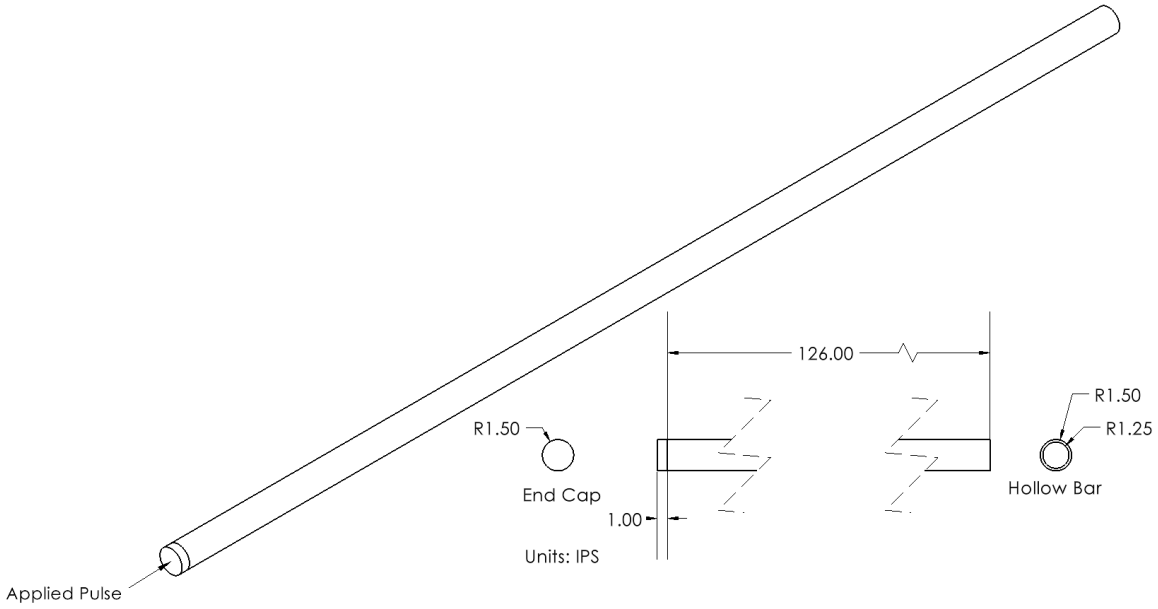

Figure 3.2 Hollow Cylindrical Bar

Finally, the third benchmark model was a cylindrical test specimen with a radius of 0.125 inches and an extruded length of 2 inches. This model is shown in Figure 3.3 and was designed to verify if perfectly-plastic behavior could be simulated within Abaqus.

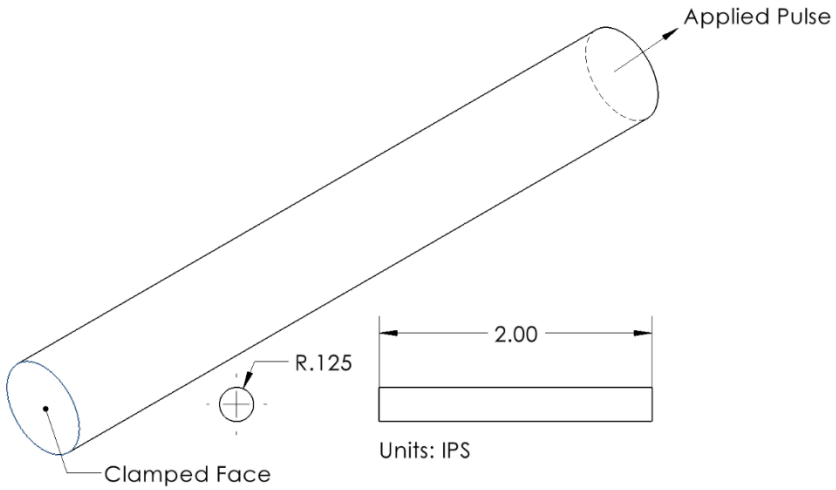

Figure 3.3 Cylindrical Test Specimen

3.3 Preprocessing

This section of the chapter briefly describes the finite element model setup in Abaqus to prepare the benchmark models for analysis.

3.3.1 Material Properties

Aluminum 6061-T651 [34-37] was selected to constitute the solid bar and hollow bar models, with the material properties being the same for both. For the test specimen, AISI 300M steel was chosen, which is a modified form of AISI 4340 steel [38-41]. The selected material properties for analysis are shown in Table 3.1. Note that the solid bar and hollow bar were assumed to behave purely elastically, so plasticity effects were not included in those models. For the plastic

behavior of AISI 300M steel, the first data set was obtained from pre-existing material information [38-41], while the second data set was arbitrarily chosen in order to create a much more prominent perfectly-plastic regime for the test specimen. Note that for AISI 300M steel its expected failure strain was taken to be 0.08 (8%) [40], but was not used during analysis since fracture behavior was not implemented into the models. However, this value will be used to explain the elastic-plastic results shown in Chapter 6.

Table 3.1 Selected Material Properties

Property	Test Specimen	Solid Bar, Hollow Bar
Material	AISI 300M Steel	Aluminum 6061
Density	0.284 lbs/in^3	0.0975 lbs/in^3
Young's Modulus	29,700 ksi	10,000 ksi
Poisson's Ratio	0.28	0.33
Yield Stress	Data Set 1: 230 ksi, 0 in/in Data Set 2: 230.5 ksi, 5 in/in	--

3.3.2 Analysis Steps

The cylindrical bars utilized the Abaqus/Explicit solver, using a Dynamic analysis and a step time of 1.5 milliseconds (ms). The field output was adjusted to ensure there was enough data sampling in order to accurately represent the propagating waves and stress-strain data. Similar to the cylindrical bars, the test specimen was also analyzed using Dynamic analysis, but with a step time of 0.2 ms and an adjusted level of output data sampling.

3.3.3 Boundary Conditions

For the benchmark models, a triangular pulse was applied with the tabular amplitude data detailed in Table 3.2 and plotted in Figure 3.4. The duration was selected to simulate a brief, high-

intensity impact event. This pulse was treated as the default testing condition and was later modified to compare the results of differing pulse shapes.

Table 3.2 Triangular Pulse Amplitude Data

Time (ms)	Amplitude
0	0
0.2	1
0.4	0

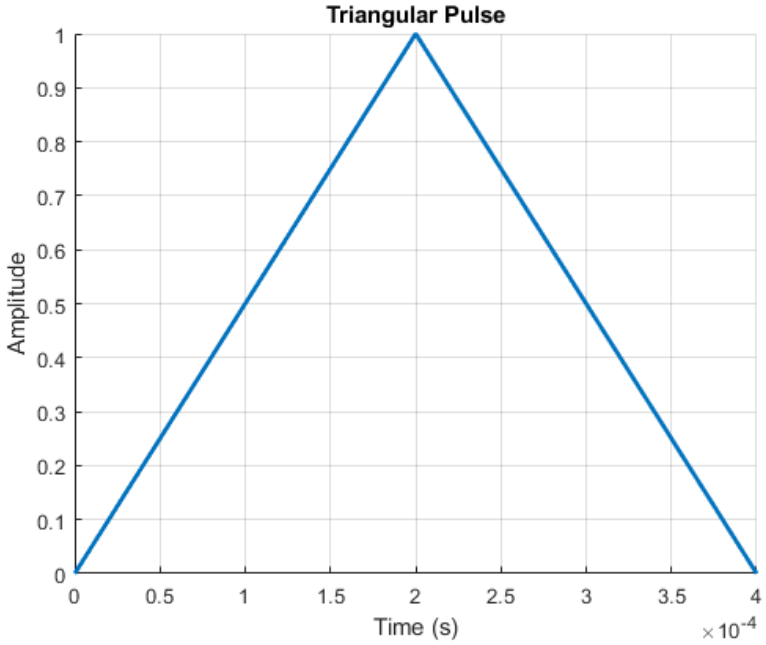

Figure 3.4 Plot of Triangular Pulse

A pressure was assigned this triangular pulse and arbitrarily given a magnitude of 10,000 psi before being applied to the two bar models. For the solid bar, it was applied perpendicular to one flat face of the model, while for the hollow bar, it was applied perpendicular to the exposed outer flat face of the end cap. The boundary conditions for the bars are shown in Figure 3.5, where the pressure is represented by the arrows pointing towards the face it is applied to.

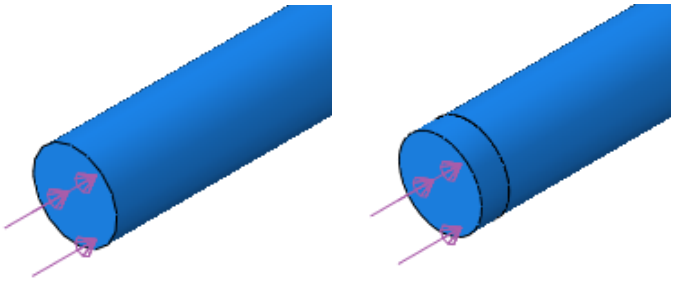

Figure 3.5 Boundary Conditions of Solid Bar (Left) and Hollow Bar (Right)

For the test specimen, one end face was clamped in place, while the opposite end face had a prescribed 0.25-inch displacement with the triangular pulse applied to it to simulate tensile strain. The boundary conditions for the test specimen are shown in Figure 3.6. The clamped boundary condition is represented by the blue and orange cones, which suppress all translation and rotation of the face it is applied to, while the prescribed displacement is represented by the orange arrows.

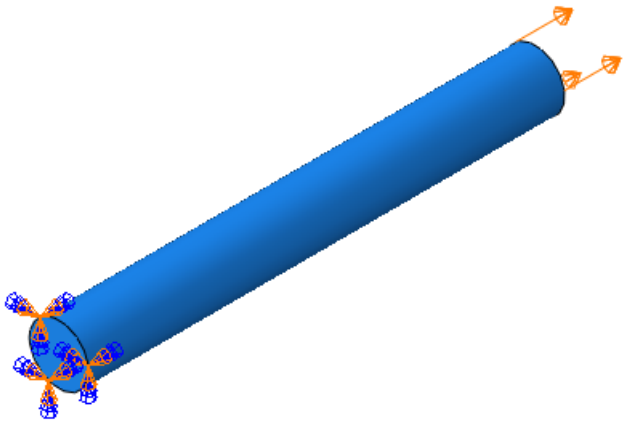

Figure 3.6 Boundary Conditions of Test Specimen

It is important to note that the applied loads on the bars generated a compression wave, while the displacement on the specimen created a tension wave. Regardless of the type of wave, all data was postprocessed accordingly to make it easier to compare.

3.3.4 Mesh Settings

Several finite element types were utilized for analysis to ensure a substantial level of comparison on the performance of the finite element models. These elements were the 10-node tetrahedral with modified formulation and four integration points, C3D10M, the 8-node hexahedral with eight integration points, C3D8, the 8-node hexahedral with incompatible modes and eight integration points, C3D8I, and the 8-node hexahedral with reduced integration and one integration point, C3D8R. The elements and their respective mesh densities in terms of nodes and elements are summarized in Table 3.3. Note that for every analysis, all mesh seed sizes were the same for all the finite element types to ensure that the finite element solutions were compared at the same level of sensitivity. For the bars, this seed size was specified as one inch. For the test specimen, the seed size was set to 0.05 inches. These seed sizes were chosen arbitrarily, as mesh convergence was not the focus when analyzing the benchmark models. Therefore, the results served primarily as a visualization of how the models behaved under an impact pulse by examining the waveforms, in the case of the cylindrical bars, or stress-strain data, in the case of the test specimen. After all the analyses, discussion was provided to show how each finite element performed in analyzing the benchmark models.

Table 3.3 Summary of Finite Elements Investigated

Model	Element Type	Number of Nodes	Number of Elements
Solid Bar	C3D10M	9,266	5,148
	C3D8, C3D8I, C3D8R	2,794	2,016
Hollow Bar	C3D10M	13,040	6,546
	C3D8, C3D8I, C3D8R	2,330	1,150
Test Specimen	C3D10M	8,702	5,422
	C3D8, C3D8I, C3D8R	1,681	1,280

3.4 Postprocessing

At the end of each benchmark analysis, data was extracted from Abaqus using provided data collection tools within the software. If the modified Hopkinson pressure bar system were to be manufactured, it was planned that two strain gauges would be mounted approximately 18 inches away from one end of the Hopkinson bar, with one at the top of the bar and one at the bottom of the bar. To obtain data in Abaqus that accurately portrayed the physical location of these strain gauges, strain data for the two bar models was obtained by querying the strain-time history at two mesh elements 18 inches away from the end of the bars closest to where the pressure was applied, which is shown in Figure 3.7 and Figure 3.8.

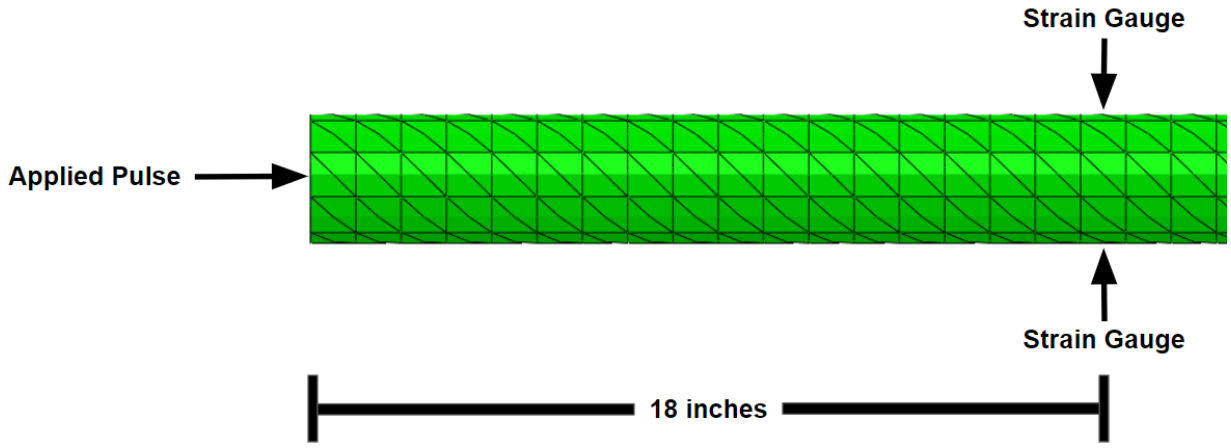

Figure 3.7 Data Extraction Locations for Solid Bar, Tetrahedral Mesh

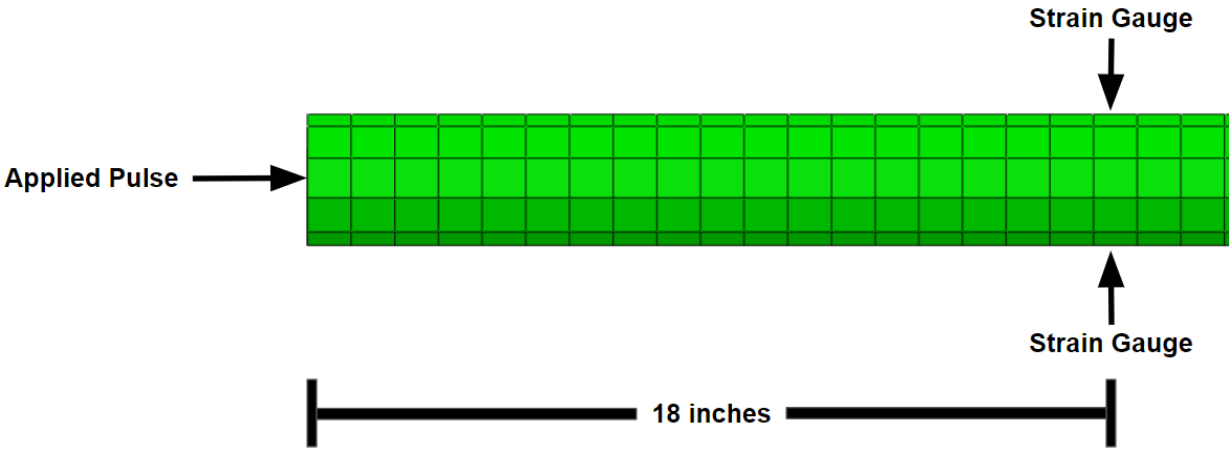

Figure 3.8 Data Extraction Locations for Solid Bar, Hexahedral Mesh

For the hollow bar, since the end cap was one inch thick, this meant querying the data at two elements 19 inches away from where the pressure was applied, which is shown in Figures 3.9 and 3.10. Only the strain data was extracted from the two bar models since the models only had elastic properties applied, rendering stress-strain data insignificant for discussion. Instead, converting the strain data into pulse waveforms that could be compared was the key point of interest.

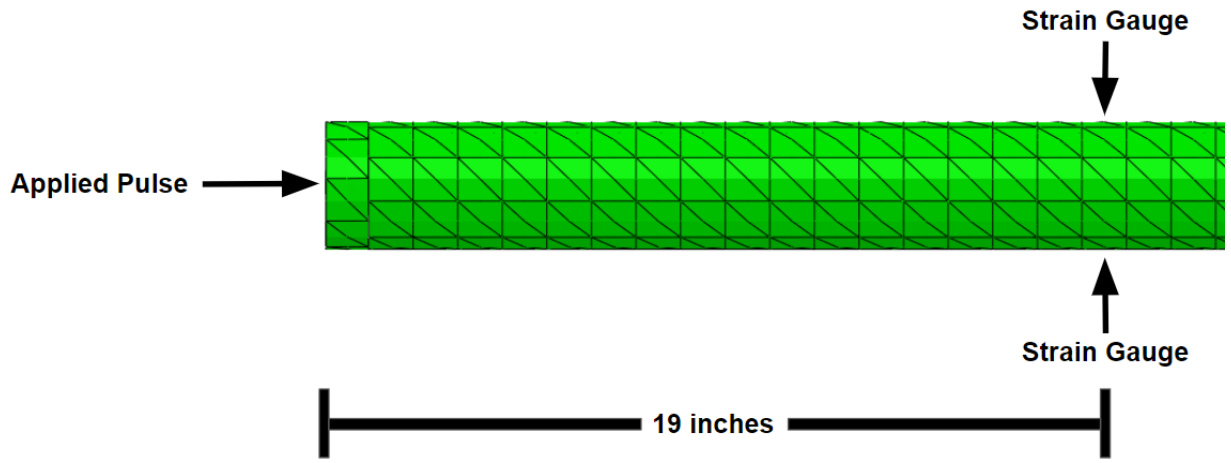

Figure 3.9 Data Extraction Locations for Hollow Bar, Tetrahedral Mesh

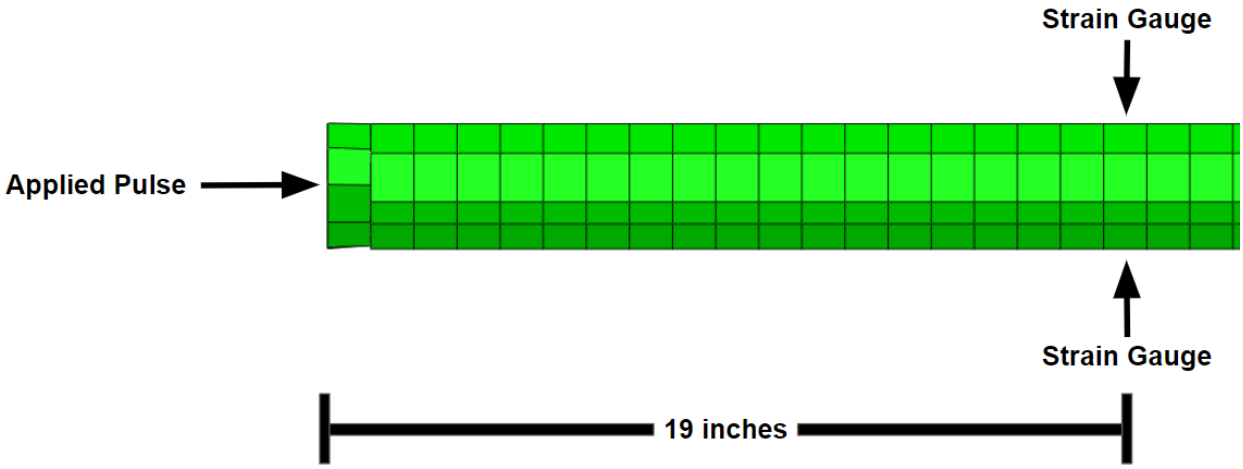

Figure 3.10 Data Extraction Locations for Hollow Bar, Hexahedral Mesh

For the test specimen stress and strain data was extracted from two elements in the necking region of the model so that its stress-strain curve could be plotted and compared for all finite element types investigated. The data extraction locations are shown in Figures 3.11 and 3.12 for the specimen in its deformed shape.

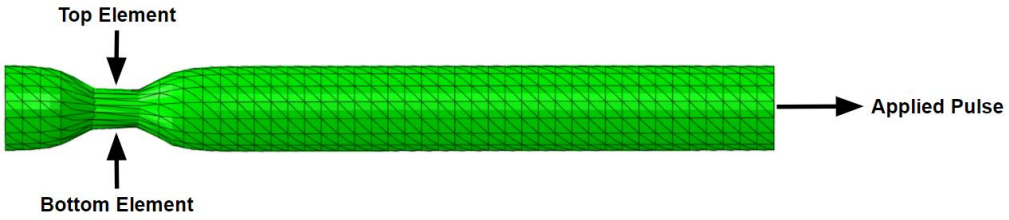

Figure 3.11 Data Extraction Locations for Test Specimen, Tetrahedral Mesh

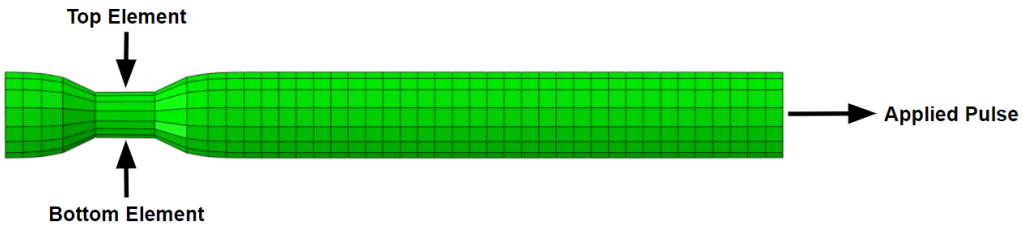

Figure 3.12 Data Extraction Locations for Test Specimen, Hexahedral Mesh

Once the data was extracted it was organized using a spreadsheet. The data was then averaged to create numerical values of stress and strain that were representative of all the integration points of the two elements queried for each model. Finally, it was imported and analyzed using the MATLAB computing environment to help visualize results and draw conclusions. This procedure was repeated for every analysis conducted.

3.4.1 Elastic Pulse Behavior in the Solid Bar Model

The propagating waveforms can be viewed in Abaqus by loading the strain data calculated in the direction of the applied pulse. For both the solid bar and hollow bar, the pulse was applied along the third axis direction. Note that in Abaqus/Explicit, logarithmic strain (LE) is the main strain output provided, but because the strains were relatively small in magnitude, it was assumed the logarithmic strain outputs were similar in value to engineering strain.

Figure 3.13 shows the results of the solid bar analysis for the C3D10M tetrahedral mesh and C3D8I hexahedral mesh at 0.1 ms. The meshes for the C3D8 and C3D8R were visually similar to the C3D8I mesh. The C3D10M mesh and C3D8I mesh show slightly different visualizations of the strain contours due to their differing levels of interpolation.

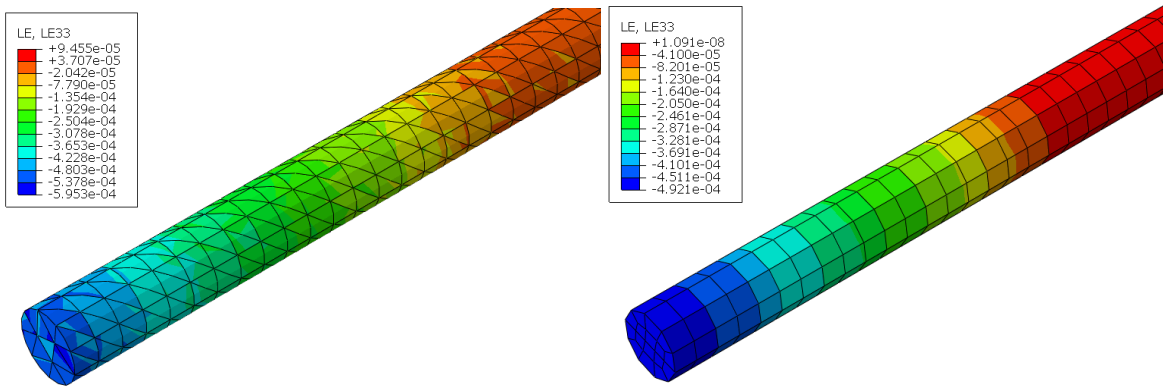

Figure 3.13 C3D10M Mesh (Left) and C3D8I Mesh (Right) Results of Solid Bar at 0.1 ms

Figure 3.14 through Figure 3.16 shows the progression of the incident wave as it travels along the solid bar to its opposite end for the C3D8I element type, which provided the clearest wave propagation contours. It was assumed that the wave propagation behavior was similar for the other three finite element types. The incident wave can be distinguished as a compression wave by looking at the values of the legend, which show mainly negative strain values. These negative values are interpreted as compressive strain.

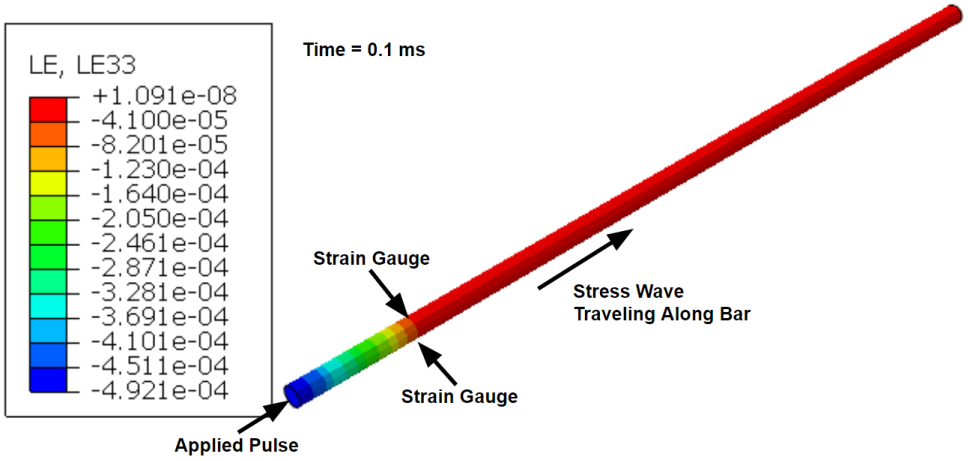

Figure 3.14 Incident Wave Propagation in Solid Bar at 0.1 ms

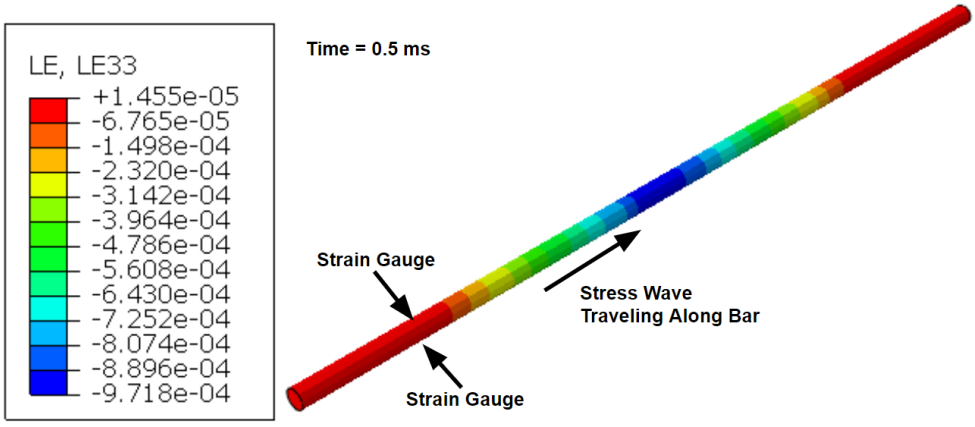

Figure 3.15 Incident Wave Propagation in Solid Bar at 0.5 ms

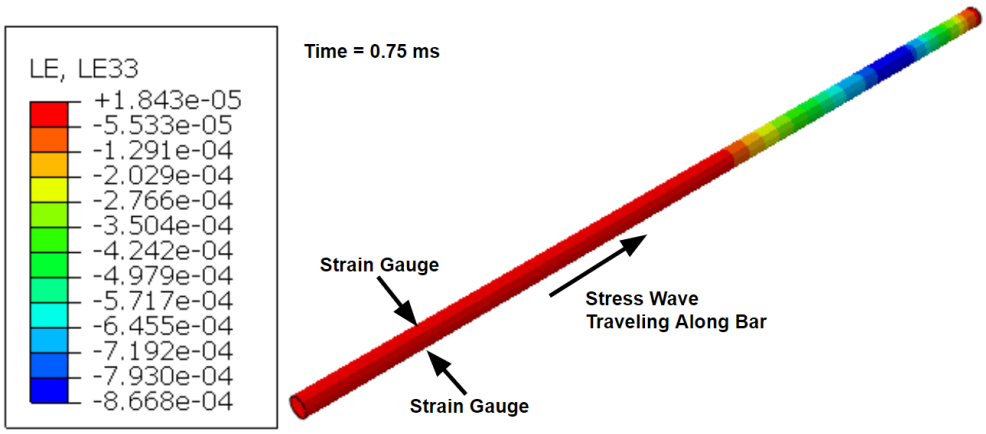

Figure 3.16 Incident Wave Propagation in Solid Bar at 0.75 ms

Similar to the results at the 0.1-ms mark, Figure 3.17 shows the results of the solid bar analysis for the C3D10M tetrahedral mesh and C3D8I hexahedral mesh at 0.9 ms. Figure 3.18 through Figure 3.20 shows the reflected wave as it travels back to the end of the bar where the pressured was first applied for the C3D8I element type. It can be distinguished as a tension wave by the values in the legend, which are mainly positive, indicating tensile strain. In general, the propagating waves are analogous to the band of colors on the contour plots moving across the bars, as evident by the gradual transition in color from red to blue for compression, and blue to red for tension.

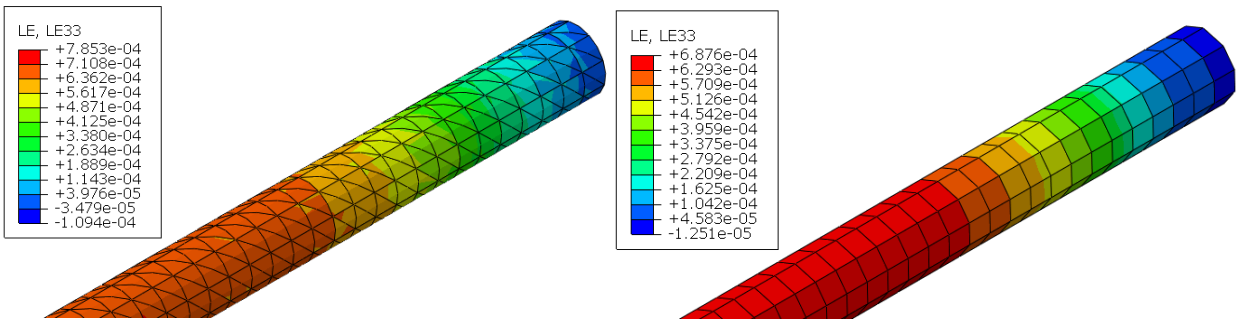

Figure 3.17 C3D10M Mesh (left) and C3D8I Mesh (right) Results of Solid Bar at 0.9 ms

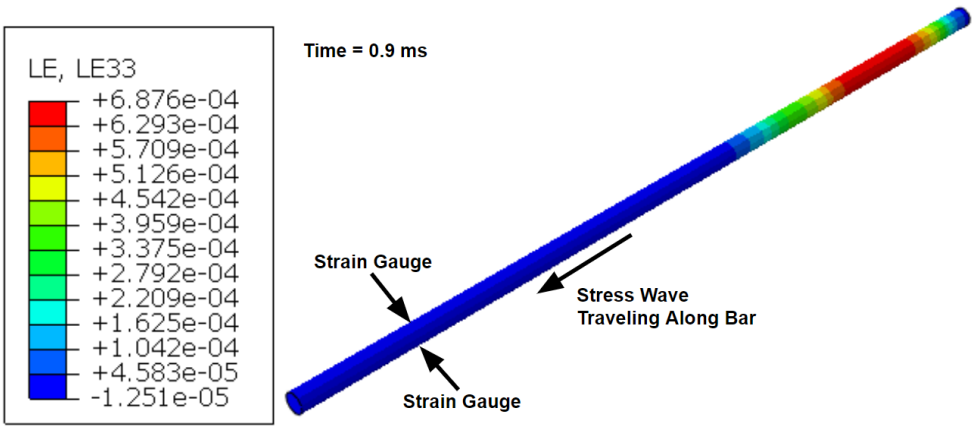

Figure 3.18 Reflected Wave Propagation in Solid Bar at 0.9 ms

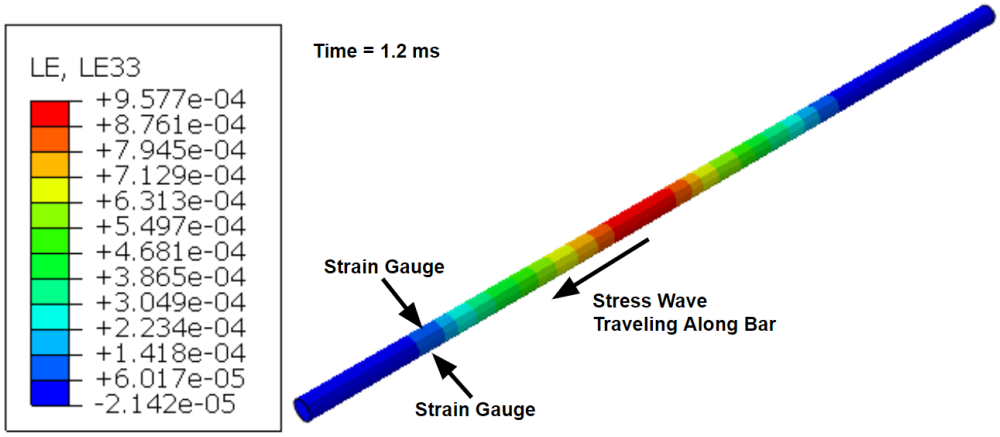

Figure 3.19 Reflected Wave Propagation in Solid Bar at 1.2 ms

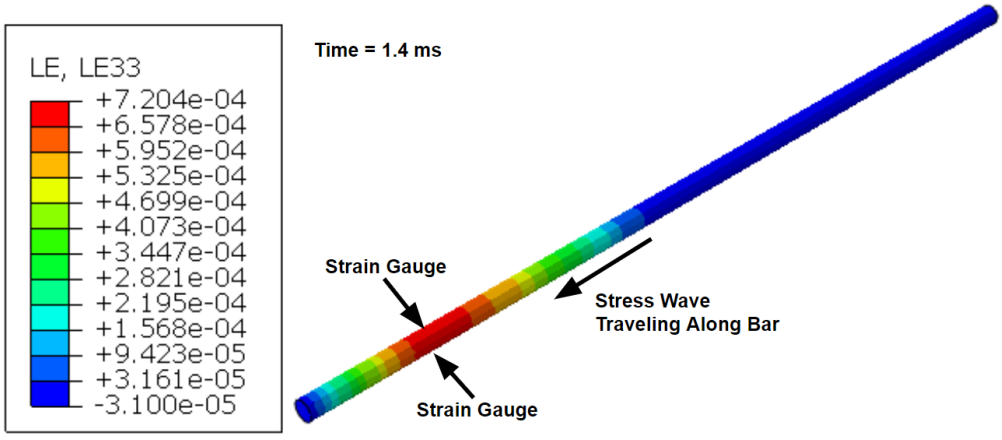

Figure 3.20 Reflected Wave Propagation in Solid Bar at 1.4 ms

The contour plots shown in Figure 3.13 through Figure 3.20 show a successful experiment of propagating an incident compression wave into the solid bar that reflect as a tension wave from the opposite end of the bar. Another visualization of the waveforms can be seen when extracting the strain-time history of the model, as seen in Figure 3.21. It is clear to see that the incident compression wave was recorded first, indicated by its negative strain values, followed by the reflected tension wave at the tail end of the analysis, indicated by its positive strain values.

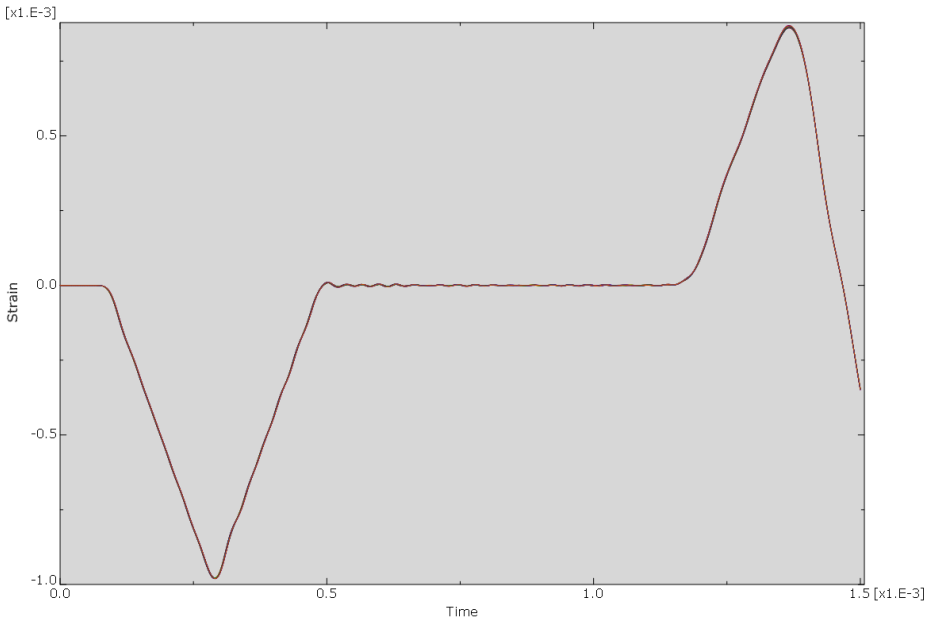

Figure 3.21 Strain-Time History in Solid Bar

To better visualize how well the incident waveform in the solid bar matched the applied impact with the triangular pulse, the impact wave was converted into a force wave by multiplying the pressure and the cross-sectional area of the face it was applied to. Additionally, the strain data was converted into force data using Equation (7) corresponding to a transmission bar on a traditional SHPB system. Any data pertaining to a compression wave was converted to positive

tension data to match the triangular pulse, which was positive, by multiplying the data by a factor of negative one. The main waveform of interest was the incident waveform, in accordance with the transmission bar force equation. The reason the transmission bar equation was used instead of the incident bar equation was because the bar models are analogous to the transmission Hopkinson bar in the proposed modified Hopkinson bar system that will be shown in Chapter 5. To check if the pulses satisfied the force equivalence condition in Equation (8), the transmitted waves were compared to the applied pulse, which was treated as the incident wave in this case. Therefore, the reflected waveform was omitted as it was not significant to the discussion. The applied pulse and the incident waveforms obtained from Abaqus analysis are plotted in Figure 3.22. The time lag labeled in the plot represents the time between when the compression wave is generated and when it first passes the 18-inch mark where the strain data was obtained on the solid bar.

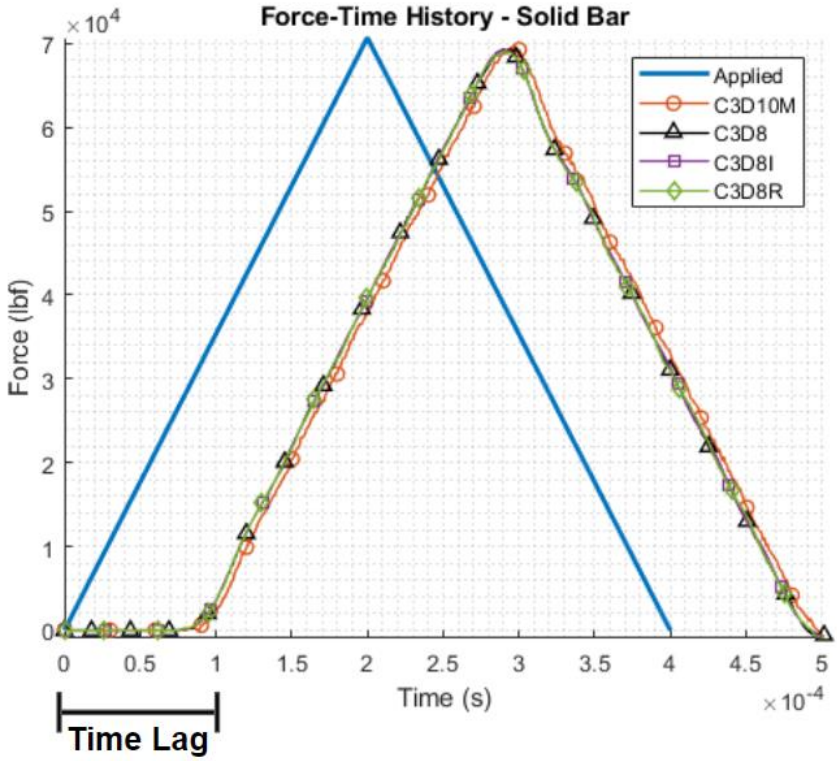

Figure 3.22 Force Wave Data in Solid Bar

By querying the peak forces of each curve, comparison of how much of the force is retained in the bar after impact can be discussed. The values of these peak forces and their respective differences relative to the applied force are compiled into Table 3.4. As an additional check, the wave speeds through the solid bar were calculated and compared to the exact wave speed through the material. The applied wave speed was calculated by taking the radical of the Young's modulus of the bar material divided by the mass density of the material, as shown in Equation (14). To calculate the wave speed from the extracted Abaqus data, the time lag had to be recorded, which was the time interval from when the applied pulse strikes and when the propagating wave first reaches the location of the strain gauges, which is the time where the wave rises at an approximately linear rate towards its peak, as seen in Figure 3.22. The wave speed was then calculated by dividing 18 inches by the time lag.

Table 3.4 Analysis Summary of Solid Bar Model

Curve	Peak Force (lbf)	Peak Force Difference	Time Lag (ms)	Wave Speed (in/s)	Wave Speed Difference
Applied	70,686	--	--	199,075	--
C3D10M	69,539	1.62%	0.081	193,048	3.03%
C3D8	69,322	1.93%	0.075	199,261	0.09%
C3D8I	69,245	2.04%	0.070	203,808	2.38%
C3D8R	69,056	2.31%	0.089	201,310	1.12%

Table 3.4 shows a good correlation with the peak forces and the wave speeds captured by the four finite elements relative to the applied pulse, with a difference of approximately 5% or less considered an acceptable deviation. This shows good results especially since the mesh was relatively coarse. A key difference was that the waveforms as determined from the strains in the solid bar were not output as sharp triangles like the applied pulse. This was due to the fact that a propagating waveform is more akin to a sinusoid rather than a sharp triangular wave. In addition,

data sampling caused a higher density of strain data points to be extracted near the peak of each wave, so not one point dominated the peak of the curve, causing a rounded interpolation of the strain wave data around the peak. This difference in the shape of the waves can also be seen by aligning them like in Figure 3.23. It was inferred that if a lower level of data sampling was used that the waveforms in Abaqus would appear much sharper, as less points would be captured near the peak of each wave. Nevertheless, the wave profiles of the four finite element types correlated very well with the wave profile of the applied pulse.

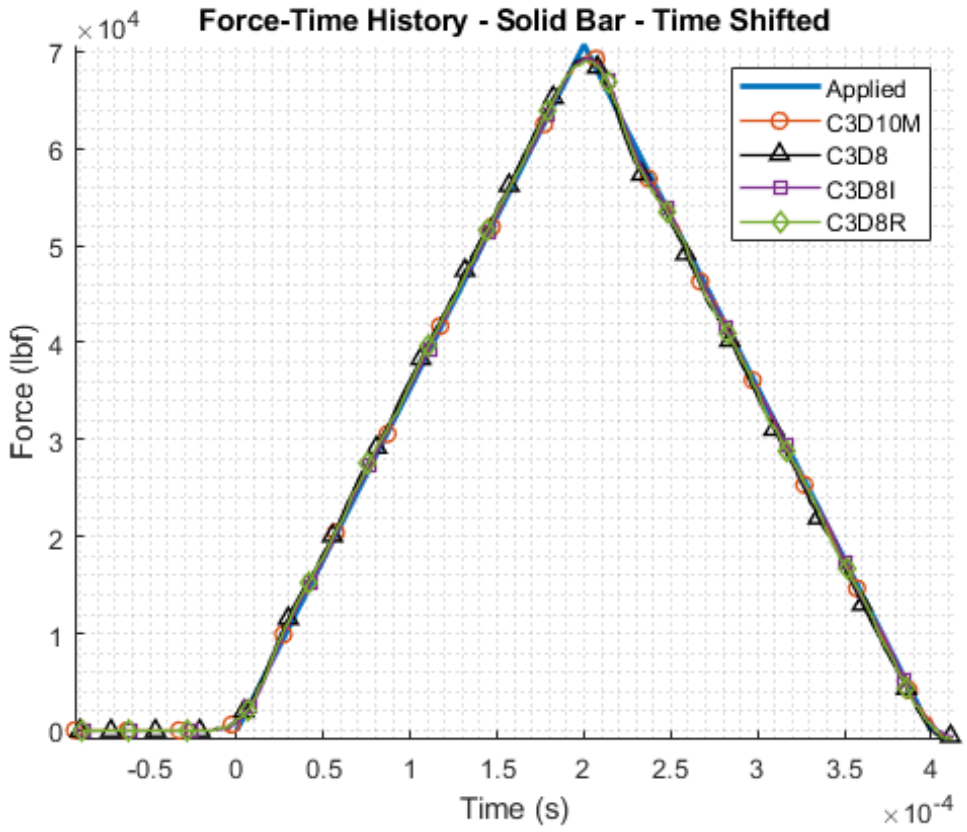

Figure 3.23 Aligned Force Wave Data in Solid Bar

3.4.2 Elastic Pulse Behavior in the Hollow Bar Model

It was assumed that the propagating waves in the hollow bar model behaved similarly to the solid bar model, so the hollow bar data was postprocessed and plotted in a similar manner and is shown in Figure 3.24. Comparisons of the peak forces and wave speeds are provided in Table 3.5.

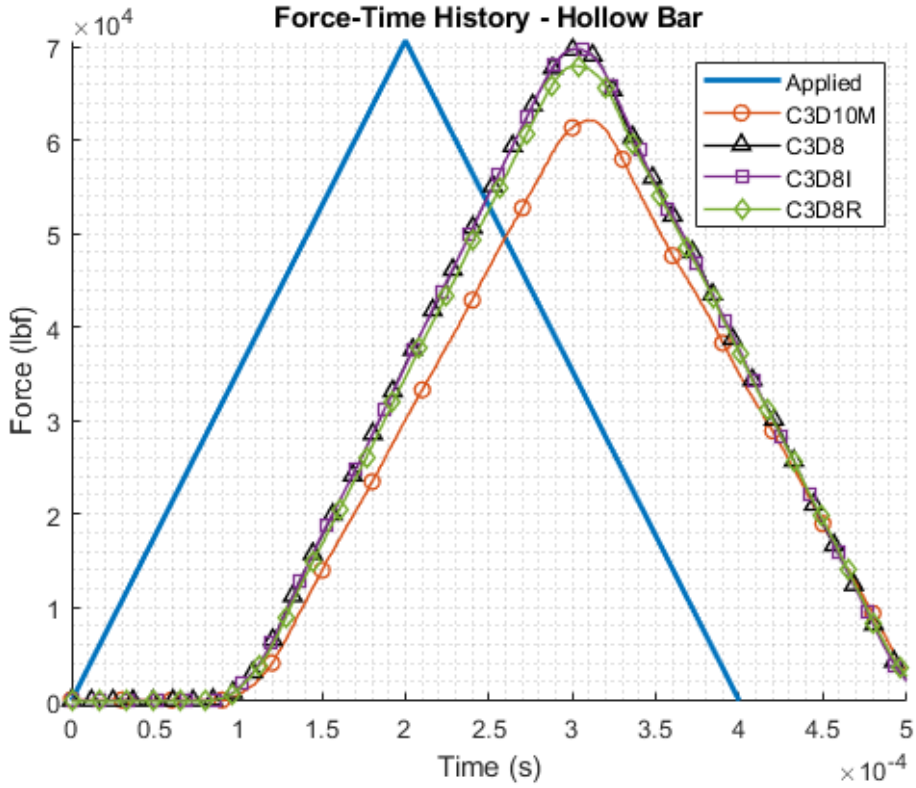

Figure 3.24 Force Wave Data in Hollow Bar

Table 3.5 Analysis Summary of Hollow Bar Model

Curve	Peak Force (lbf)	Peak Force Difference	Time Lag (ms)	Wave Speed (in/s)	Wave Speed Difference
Applied	70,686	--	--	199,075	--
C3D10M	62,212	11.99%	0.109	165,032	17.10%
C3D8	69,766	1.30%	0.102	176,800	11.19%
C3D8I	69,808	1.24%	0.103	175,372	11.91%
C3D8R	67,996	3.81%	0.103	174,348	12.42%

Deviations within the finite elements became more apparent in the hollow bar model. The peak force and wave speed in the quadratic tetrahedral C3D10M element deviated the most. This was due to element distortions throughout the mesh that led to inaccuracies in the solution. Even with element distortions due to the coarse seed size of one inch, the C3D10M waveform still had similar curvature to the applied pulse despite its large difference. In contrast, all three linear hexahedral elements (C3D8, C3D8I, C3D8R) calculated waveforms with similar levels of deviation relative to the applied pulse. The C3D8R element, while still being within an acceptable difference of 5%, had a higher difference in peak force compared to the C3D8 and C3D8I elements. This was due to the characteristic nature of the reduced integration hexahedral. Since there is only one integration point in each element, the strain response is represented by a singular, constant value in each element. As a result, slight differences in strain within an element will not be captured since only one value is calculated. The fully-integrated C3D8 and C3D8I elements counteract this effect and more accurately capture slight changes in strain within one element due to its multiple integration points. Despite the peak forces for the hexahedral elements showing a good correlation with a peak difference of 3.81%, the wave speeds in these elements had larger differences, with a peak difference of 12.42%. This was believed to be a result of the coarse mesh like with the C3D10M element, which had a seed size of one inch for the entire model, and due to the change in geometry from the end cap to the hollow bar, causing slight dissipation in the wave propagating through the hollow bar wall. The deformation and dynamics of the end cap both have an effect on how the applied pulse transmits into the hollow bar. Comparing Table 3.4 and Table 3.5 show that the solid bar matched the applied pulse much more accurately for all finite element types, indicating that there were much less factors interfering with the strain response in the solid bar since it was the only component in its finite element model. Nevertheless, the waveforms in the

hollow bar correlated in shape to the applied pulse in an acceptable manner just like the solid bar, proving the principles of wave propagation. Modifications to the mesh density will be explored in Chapter 6 to address the large differences of the finite element solutions from the applied pulses.

3.4.3 Plastic Behavior in the Solid Test Specimen Model

The last analysis pursued to build a good foundation for analyzing the proposed modified Hopkinson bar design was to check if the perfectly-plastic behavior in the test specimen was simulated accurately based on the user-defined yield stress and plastic strain data sets shown in Table 3.1. In Abaqus, the strain along the axial direction of the specimen can be seen in Figure 3.25. A large amount of necking was observed near the clamped end of the specimen, with a peak strain of over 1.0 (100%), but this was due to the large displacement boundary condition specified earlier. The positive values in the legend indicate the specimen experienced tensile strain.

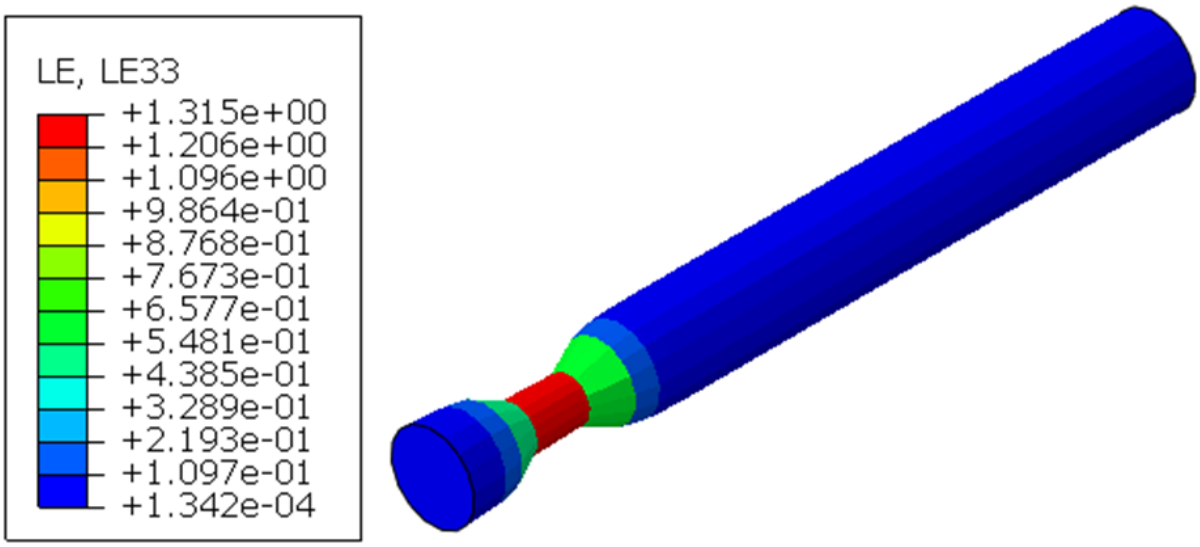

Figure 3.25 Strain Contours in Test Specimen

To check the material behavior of the specimen, stress-strain data was extracted from an element at the top and bottom of the necking zone as shown in Figure 3.11 and Figure 3.12. The data was averaged, then the stress-strain curves of the test specimen were plotted in Figure 3.26. The perfectly plastic behavior can be distinguished by a portion of the curve looking mostly parallel with the x-axis of the plot. From the user-defined plastic material properties for the specimen, the slope of the perfectly plastic portion of the model was expected to be 0.1.

For the triangular pulse, the most significant discrepancy was the large amount of dispersion present in all the finite elements investigated, making it difficult to see what the curve actually looked like. This was due to the fact that a triangular pulse inherently induces a sharp rise time and a sharp transition at its peak, which tends to generate multiple oscillations that reduce the quality of the captured material behavior, giving it a noisier appearance when plotted.

Another issue occurred during the averaging of the data pertaining to the C3D10M element. Some integration points of the two queried elements experienced larger plastic deformation than other integration points, increasing the calculated strain and making the element appear more compliant. A quick calculation of the slope between the two points shown in Figure 3.27 in the elastic portion of the C3D10M curve showed that the Young's modulus of the material was predicted to be 11,790 ksi. This was a much lower than the user-defined stiffness, which was 29,700 ksi, leading to a difference of 60%. Looking at Figure 3.27 again and taking the slope of the elastic portion of the C3D8R curve showed the Young's modulus of the material to be 29,260 ksi, giving a more acceptable 1.5% difference of the calculated stiffness relative to the defined stiffness. Since all the linear hexahedral elements' elastic regimes were essentially aligned, the stiffnesses of the C3D8 and C3D8I elements were assumed to be of similar magnitude to the C3D8R element. This showed how the C3D10M element inaccurately predicted the stress-strain

behavior of the test specimen due to its element distortions, making it appear more compliant, while the linear hexahedral elements excellently captured the stiffness of the specimen material.

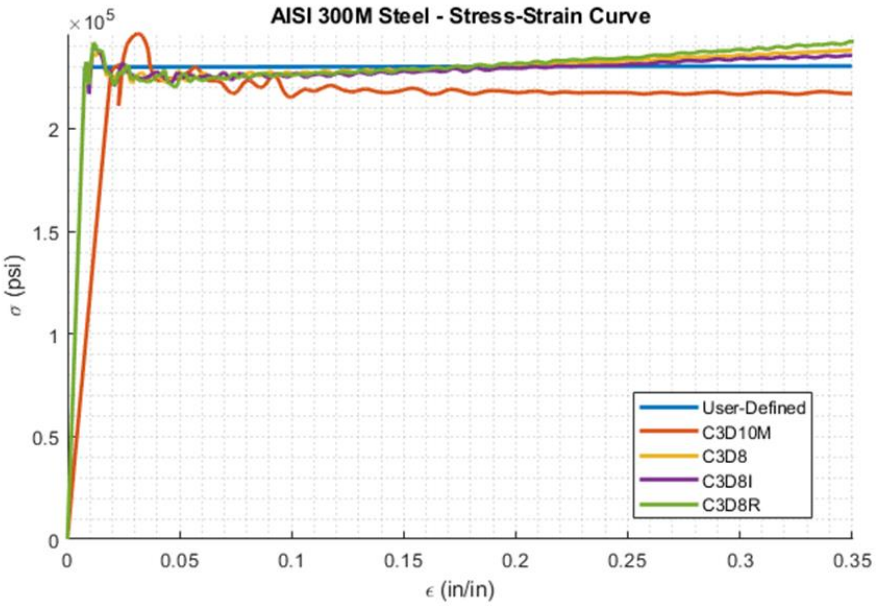

Figure 3.26 AISI 300M Steel Material Behavior, Triangular Pulse

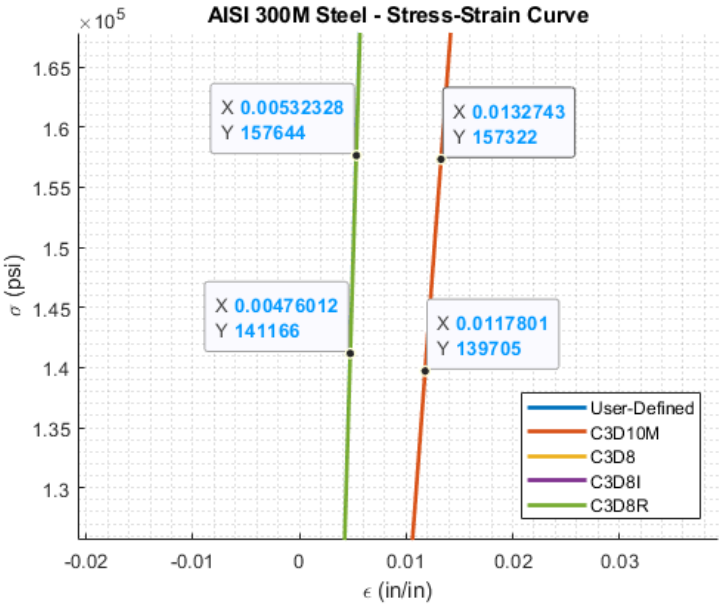

Figure 3.27 Data Points for Stiffness Calculation, Triangular Pulse

To address the issue of dispersion and noise induced by sharp transitions, the pulse was modified to a sinusoidal pulse from the default triangular pulse so the applied loading could have a much more gradual rise time. The sinusoidal pulse is plotted in Figure 3.28.

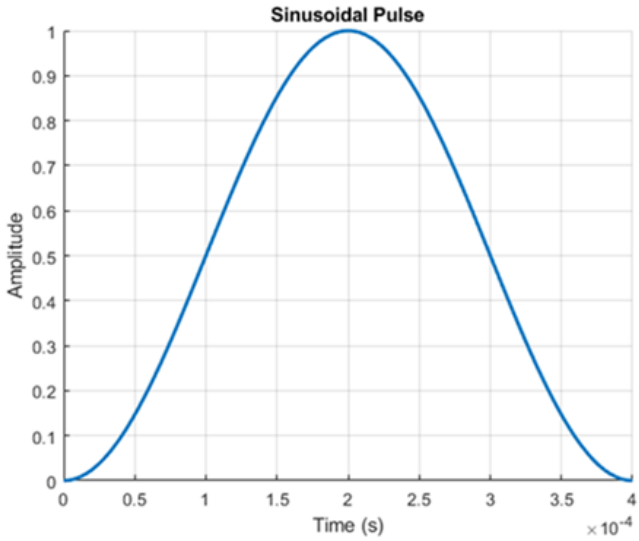

Figure 3.28 Plot of Sinusoidal Pulse

With this change, Figure 3.29 shows the reduced dispersion in the stress-strain curves. This made the plastic behavior of the material look more like the user-defined constitutive behavior, proving that the analysis was successful in replicating the stress-strain curve based on the elastic-plastic material properties implemented into the model. Stiffness calculations were carried out similar to the case of the triangular pulse using the data points in Figure 3.30, yielding a stiffness of 11,975 ksi for the C3D10M element and a stiffness of 29,773 ksi for C3D8R element, which was assumed to be of a similar value if calculated for the C3D8 and C3D8I elements. This led to percent differences relative to the defined stiffness of 60% and 0.25%, respectively. This showed once again how the C3D10M element predicted the specimen to be uncharacteristically more compliant compared to the linear hexahedral elements regardless of the pulse shape.

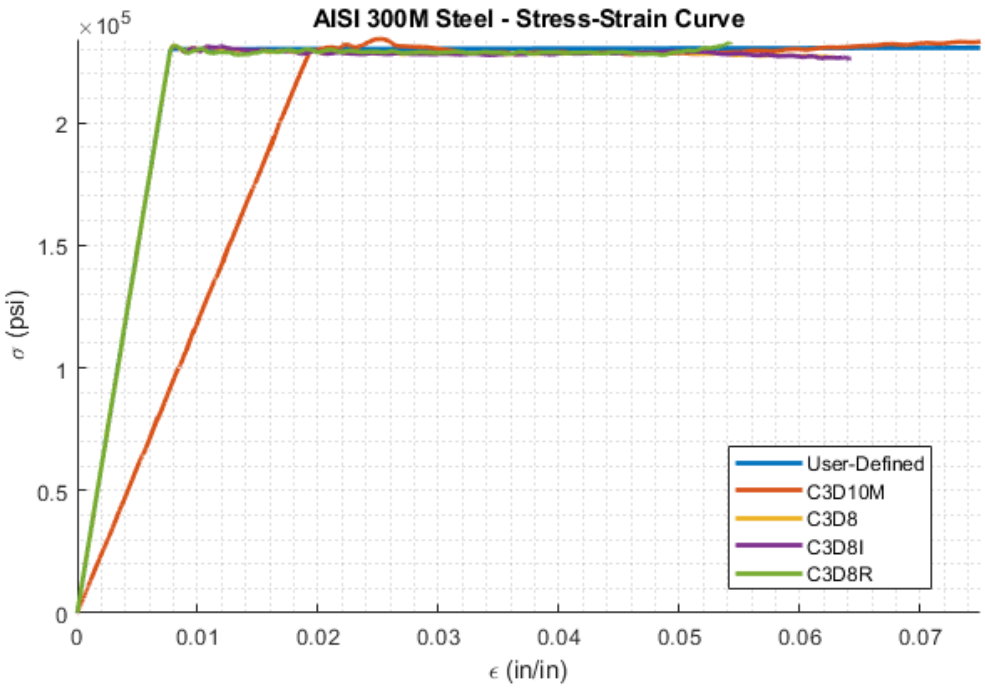

Figure 3.29 AISI 300M Steel Material Behavior, Sinusoidal Pulse

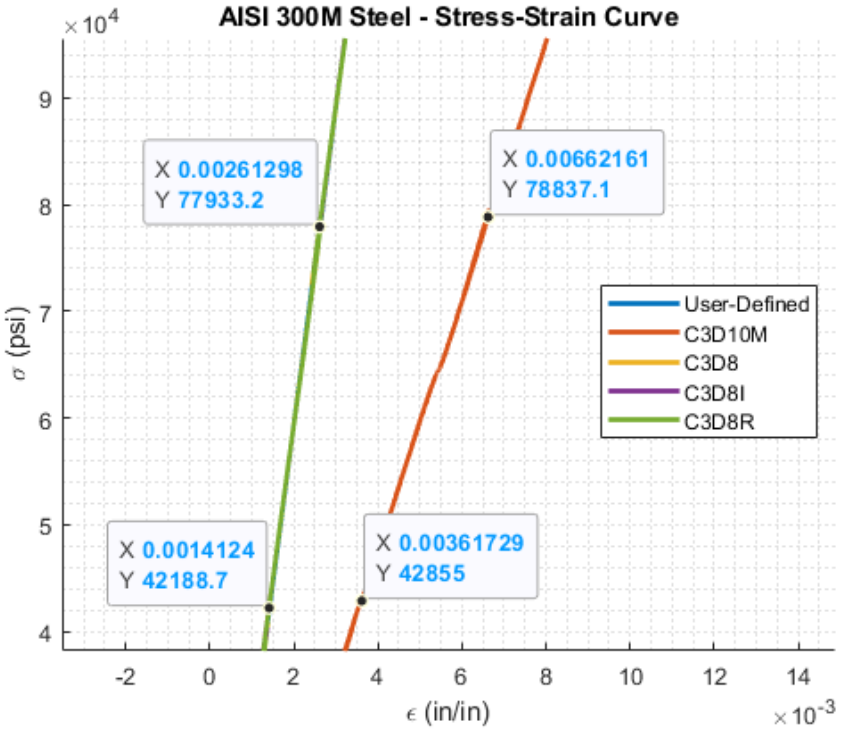

Figure 3.30 Data Points for Stiffness Calculation, Sinusoidal Pulse

3.5 Closing Remarks

It was shown that the linear hexahedral element types showed similar behaviors of wave propagation, while the quadratic tetrahedral element started to deviate as the benchmark analysis progressed. These deviations in the quadratic tetrahedral element were mostly attributed to issues pertaining to element distortions, which adversely affected the results. The element distortions arose from the coarse mesh, so it was assumed refining the mesh would eliminate those distortions and improve the accuracy of the solution. Regardless, all elements were taken into the next stage of the research. Chapter 6 will focus on the selection of the element type for the final stages of the analytical research, providing substantial discussion as to why a specific element was selected.

Since the test specimen and hollow rod best captured the intended shape of the actual tensile specimen and modified Hopkinson bar, the next chapter will focus on the use of symmetry planes to determine how well the accuracy of portraying the wave propagation is retained while achieving a reduction in the size of the model and potentially a reduction in analysis time.

Chapter 4

Investigations of Analytical Symmetry

4.1 Objective

The modified Hopkinson pressure bar system that will be explored in Chapter 5 was expected to require a large number of nodes, which would not only lengthen the analysis time, but prevent substantial mesh convergence studies from taking place that ensured the pulse responses in the system were being captured accurately. In the following sections of this chapter, usage of symmetry planes in the hollow bar model and test specimen model were investigated to examine the effects of symmetry on the structure and verify the analytical results using the same equations from Chapter 3.

4.2 Preprocessing

The tensile specimen and Hopkinson bar were the two components of interest, as it will be shown in the next two chapters that the force response in the specimen was compared to the force response in the Hopkinson bar to determine if the Hopkinson bar can be used as an accurate measure of the forces developed in the specimen. Using a singular symmetry plane, both the hollow bar and the test specimen were cut in half in a top-to-bottom fashion, as can be seen in the case of the hollow bar in Figure 4.1. In the figure, a plane parallel to the YZ plane was used as the cutting plane.

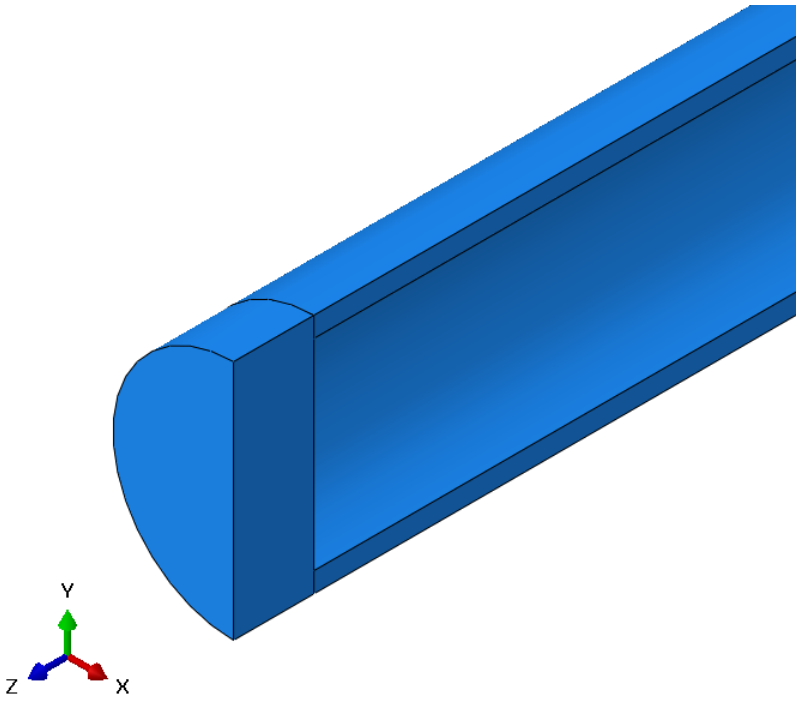

Figure 4.1 Subsection of the Half Symmetric Hollow Bar

To ensure that the cut models behaved like their corresponding full models, a zero-displacement condition was applied perpendicular to the internal faces normal to the plane cut, which can be seen as orange cones in Figure 4.2, in the case of the test specimen. Both models utilized similar symmetry conditions but just on different internal faces. This ensured that the applied pressure did not cause the models to deform out-of-plane uncharacteristically. Finally, the mesh was re-applied using the same seed size as the mesh of the full models. Other than the modified boundary conditions and mesh settings, the material properties, analysis steps, and other settings were retained.

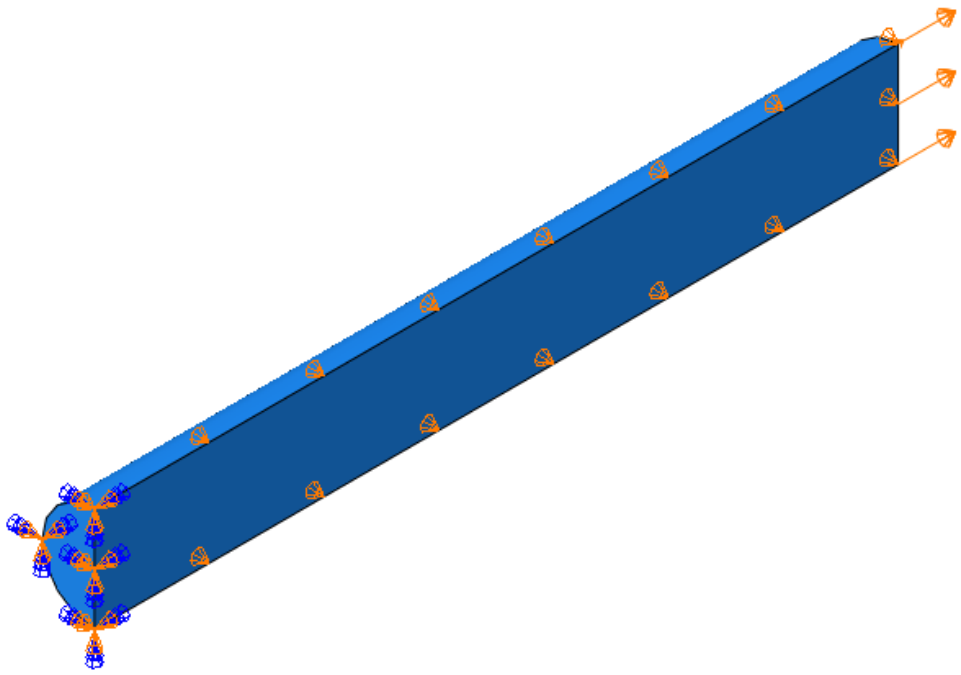

Figure 4.2 Visualization of Symmetric Boundary Conditions on Test Specimen

4.3 Postprocessing

Upon conclusion of all symmetric analyses, data was acquired, organized, and postprocessed using the same methods as described in Chapter 3.

4.3.1 Results with One Symmetric Plane Cut

The compression wave propagating through the halved hollow bar model is shown in Figure 4.3 at a time of 0.5 ms for the C3D8R element, which was similar to the wave propagation for the full hollow bar model. It was assumed the propagation was similar for the other element types investigated. The transitional color band was retained, showing that the wave propagated through the bar as if the hollow bar was not cut. It also showed a successful experiment of wave propagation from the applied pulse within a model that was cut using one plane of symmetry.

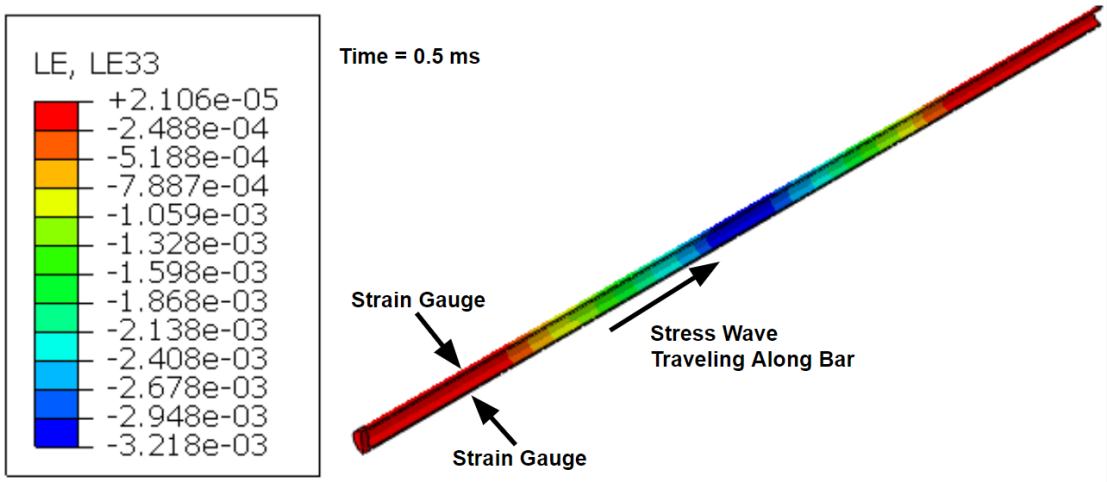

Figure 4.3 Compressive Wave Propagation in Half Symmetric Hollow Bar, 0.5 ms

Converting the applied pressure and strain data into forces yields Figure 4.4. Overall, the waveforms were similar to the applied pulse, much like the full model version of the hollow bar.

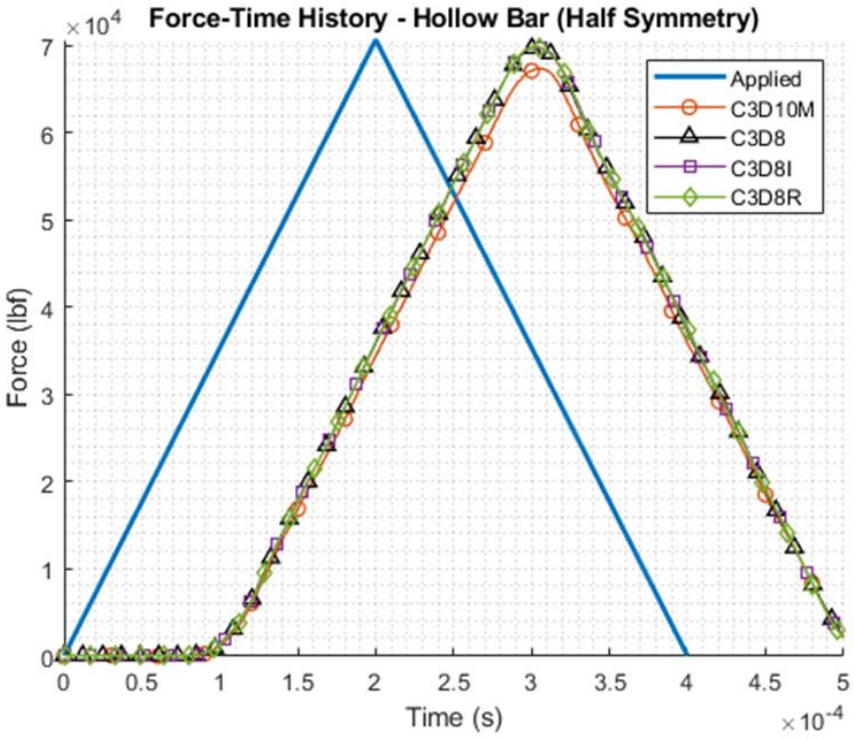

Figure 4.4 Force Wave Data in Half Symmetric Hollow Bar Model

Results of the half symmetric model of the hollow bar are shown in Table 4.1. The peak forces and wave speeds showed a strong similarity to the performance of the full model of the hollow bar, even showing an improvement in the peak force difference and wave speed for the C3D10M element, which was attributed to a smaller number of element distortions, and thus an increase in accuracy of the solution. Even with a coarse mesh density, results of the hollow bar with a symmetric plane cut proved that the Hopkinson bar in Chapter 5 will perform as expected if also using symmetry.

Table 4.1 Analysis Summary of Half Symmetric Hollow Bar Model

Curve	Peak Force (lbf)	Peak Force Difference	Time Lag (ms)	Wave Speed (in/s)	Wave Speed Difference
Applied	70,686	--	--	199,075	--
C3D10M	67,446	4.58%	0.103	174,586	12.30%
C3D8	69,766	1.30%	0.102	176,800	11.19%
C3D8I	69,808	1.24%	0.103	175,372	11.91%
C3D8R	69,910	1.10%	0.104	173,873	12.66%

Using a sinusoidal pulse for the half symmetric model of the test specimen, the stress-strain curves were plotted in Figure 4.5. Dispersion was highly reduced in the half symmetric model for all the finite element types, with their curves looking much more similar to the simulated perfectly plastic curve than in the case of the fully-sized test specimen. All finite elements captured the material behavior so similarly that their curves aligned over the elastic regime of the stress-strain curve. The element that deviated the most was the C3D8R element, which had a peak stress deviation of 2.59% compared to the user-defined yield stress of 230 ksi, though this was considered an acceptable difference since it was under 5%. In combination with the pulse behavior in the half symmetric hollow bar, the half symmetric test specimen investigated in this chapter makes a strong case for using symmetry in the modified Hopkinson pressure bar design that will be explored in

Chapter 5 and analyzed in Chapter 6. Thus, the remainder of this thesis will focus mainly on the half symmetric version of the proposed design instead of its full models (no symmetry taken advantage of).

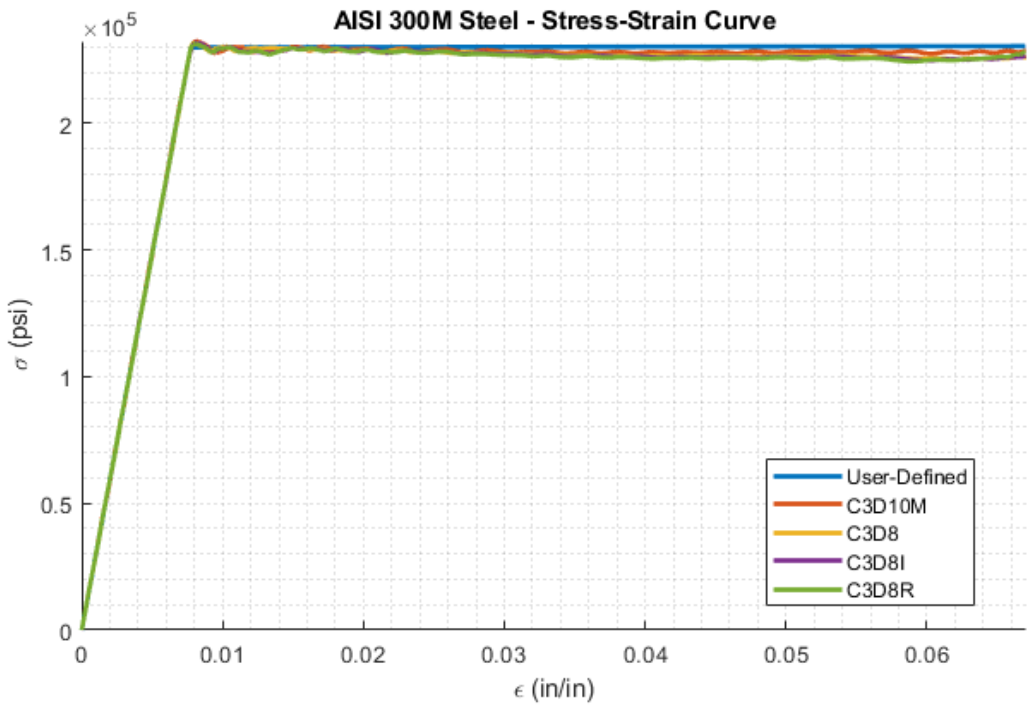

Figure 4.5 Material Behavior of Half Symmetric Test Specimen Model, Sinusoidal Pulse

Chapter 5

Design of Tension Yoke Apparatus

5.1 Overview

With an understanding of the effects of dynamic loading from benchmark analyses, research progressed onto the modified Hopkinson pressure bar system. The modified design is composed of a Hopkinson bar which is similar geometrically to the hollow bar benchmark model, and a tension yoke apparatus which contains the specimen. The tension yoke is shown in Figure 5.1 and Figure 5.2.

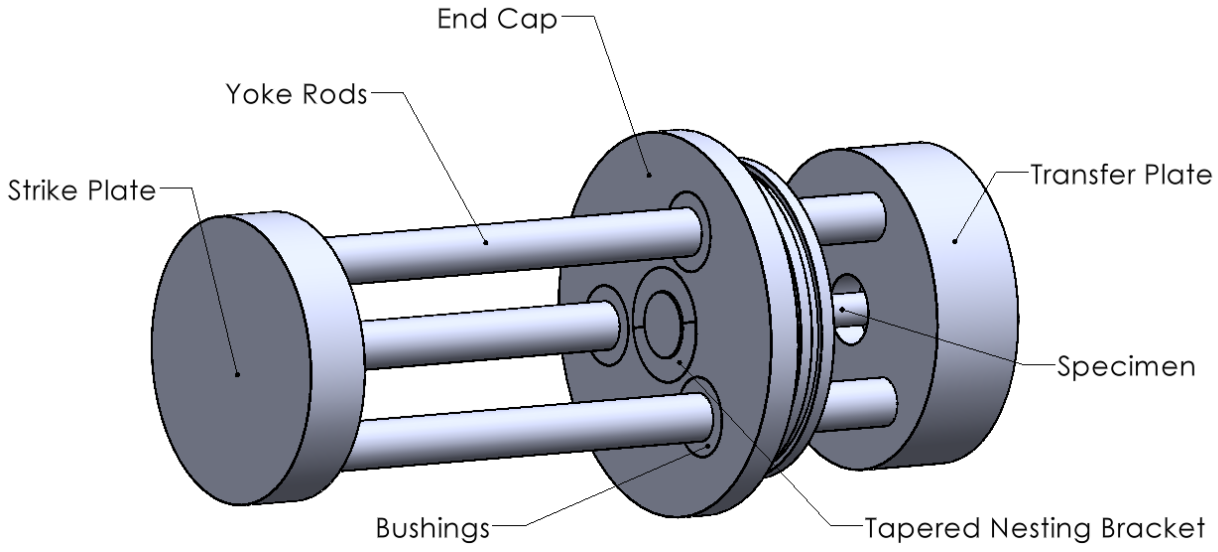

Figure 5.1 Frontal Dimetric View of Tension Yoke

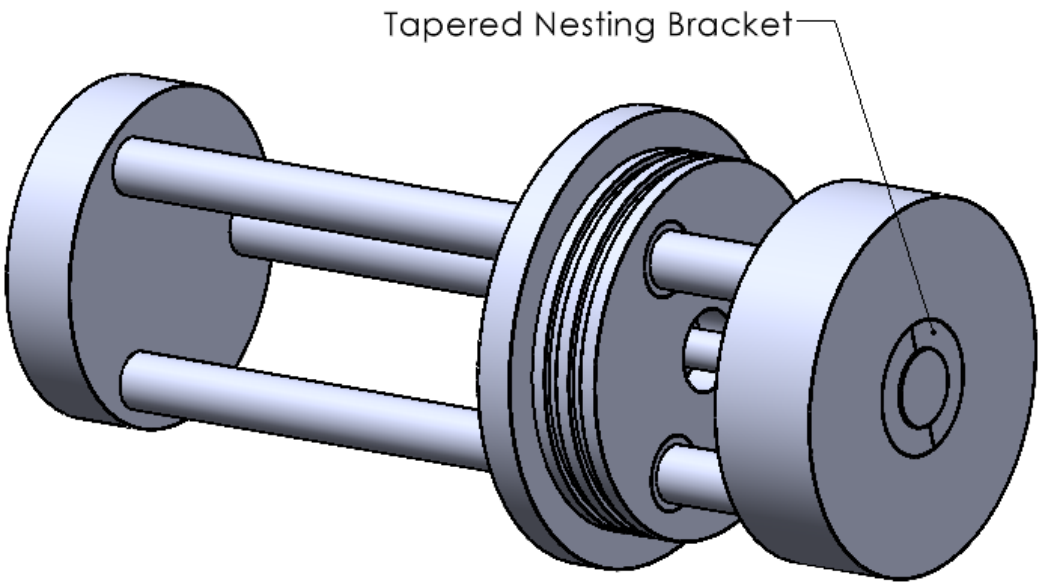

Figure 5.2 Back Dimetric View of Tension Yoke

The yoke is composed of a strike plate and a transfer plate connected by three rods separated 120˚ apart from each other, which were proposed to alleviate issues of eccentricity. Using three holes in a modified end cap, the rods can slide freely through the end cap bushings, moving both plates simultaneously while also restricting motion such that the yoke only moves along the rods' longitudinal axes. The transfer plate and the end cap both contain tapered nesting brackets which fix the test specimen to each of these components. The outer diameter of the transfer plate is slightly smaller than the inner diameter of the Hopkinson bar to allow free motion. The end cap seats directly onto the Hopkinson bar as seen in Figure 5.3. A cutout will be made in the Hopkinson bar to allow direct observation of the deforming specimen using high speed cameras, and allow for vision-based metrology, namely digital image correlation. Note that the cutout shown in Figure 5.3 was exaggerated to see the inside of the bar more clearly, and its dimensions can be adjusted to meet manufacturing needs for the actual experimental setup.

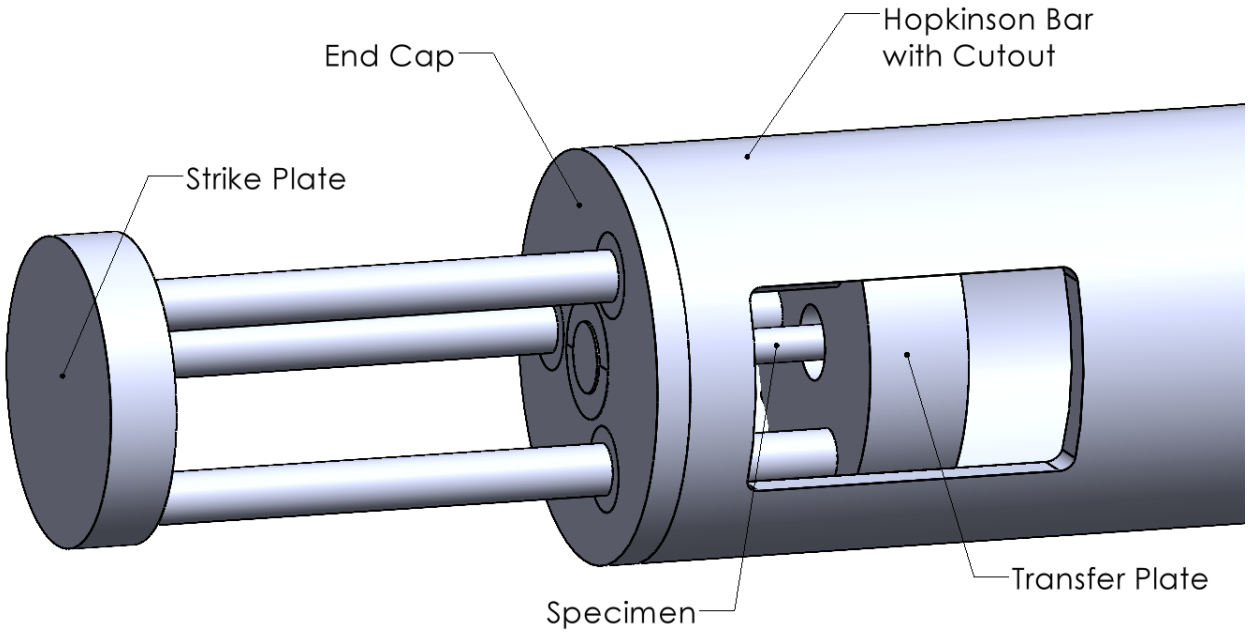

Figure 5.3 Modified Design with Cut Hopkinson Bar for High-Speed Camera

The tensile specimen designed for the yoke is shown in Figure 5.4. It has larger ends that allow it to be clamped within the nesting brackets of the end cap and the transfer plate. The specimen then tapers to a middle gauge section with a cross-sectional radius of 0.125 inches.

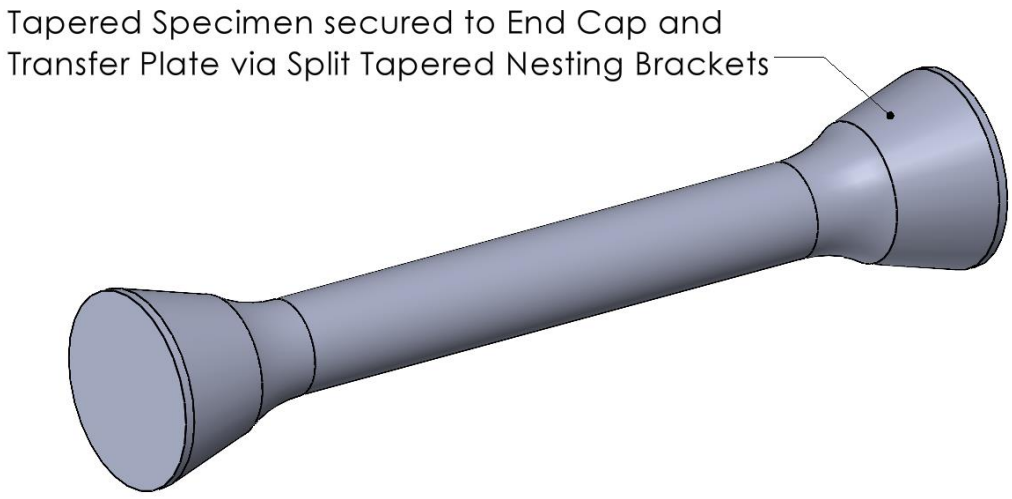

Figure 5.4 Proposed Tensile Specimen

The dynamic loading action is best described by the schematic shown in Figure 5.5. To create tension in the specimen, a projectile is launched and impacts the strike plate of the yoke, either directly or via an intermediate transfer shaft. The impact imparts a compressive wave from the projectile that travels through the rods and into the transfer plate of the yoke. With the end cap assumed to be fixed in place (mounted to the end of the Hopkinson bar), tension is generated in the specimen at the interface between the specimen and the transfer plate, creating a tension wave that propagates back through the specimen towards the end cap. Finally, the tension wave transfers from the end cap into the end of the Hopkinson bar, imparting a compression wave which is finally measured by strain gauges located 18 inches from the interface between the end cap and the Hopkinson bar. In summary, the yoke experiences compression from the projectile, propagating in tension through the test specimen until reflecting off the end cap, then propagating in compression once again from the end cap into the Hopkinson bar.

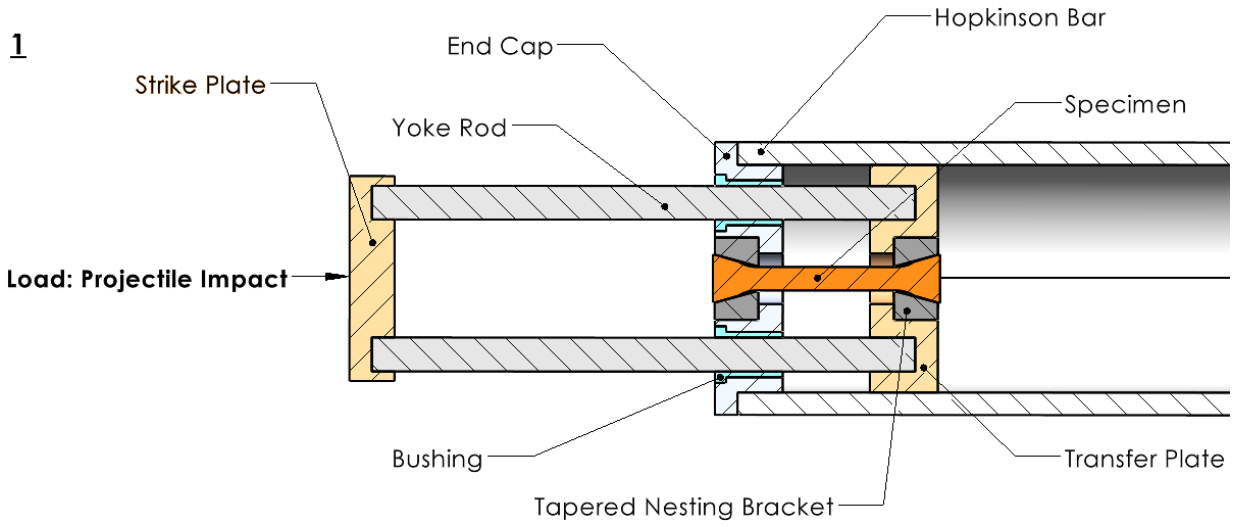

Figure 5.5 Tension Yoke Loading Action

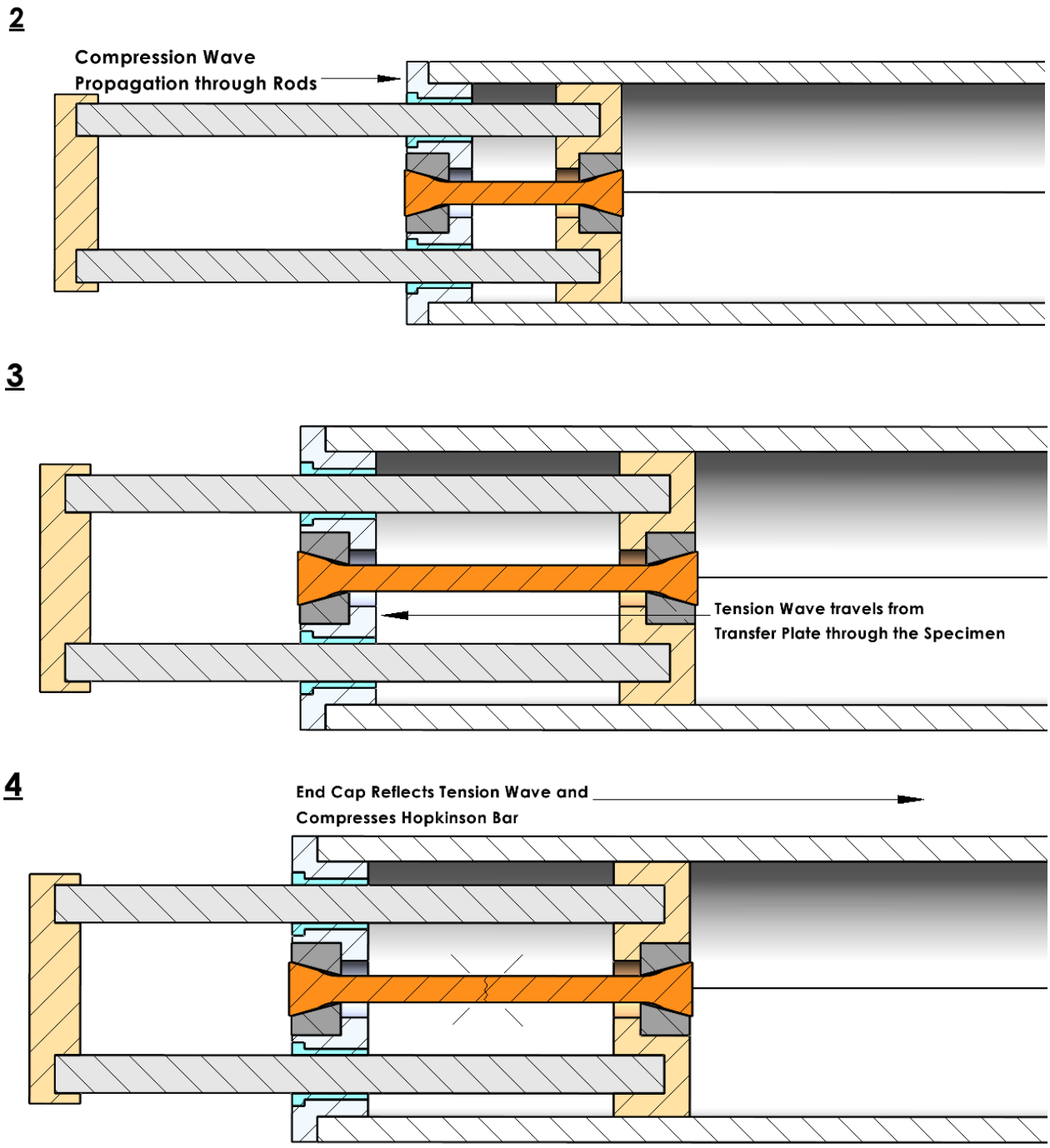

Figure 5.5 Tension Yoke Loading Action (Continued)

5.2 Defeatured Adaptation

Several features of the proposed design present geometric complexities that would make the finite element model difficult to prepare for analysis. To simplify the design, the Hopkinson bar system was defeatured by removing aspects that were not as necessary for analysis. Other than filling in the cut for the high-speed cameras in the Hopkinson bar, it had no major features to remove, so most of the defeaturing was done on the tension yoke. The defeatured model is shown with the Hopkinson bar in Figure 5.6 and without the Hopkinson bar in Figure 5.7. First, all the holes in the strike plate and transfer plate were removed. This removed the nesting bracket on the transfer plate. Similarly, the nesting bracket was removed from the end cap. As a result, the yoke rods and tensile specimen were constrained to the outer faces of the plates and end cap. Additionally, the rod bushings were removed and the diameter of the holes in the end cap for the yoke rods were reduced to match the diameter of the yoke rods themselves. Chapter 6 will explore analyses of the modified system with this defeatured adaptation of the yoke.

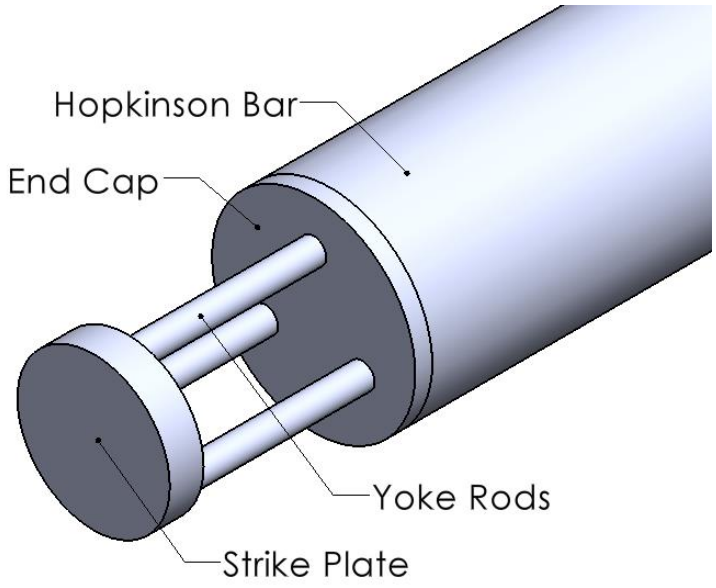

Figure 5.6 Fully Defeatured Hopkinson Pressure Bar Design

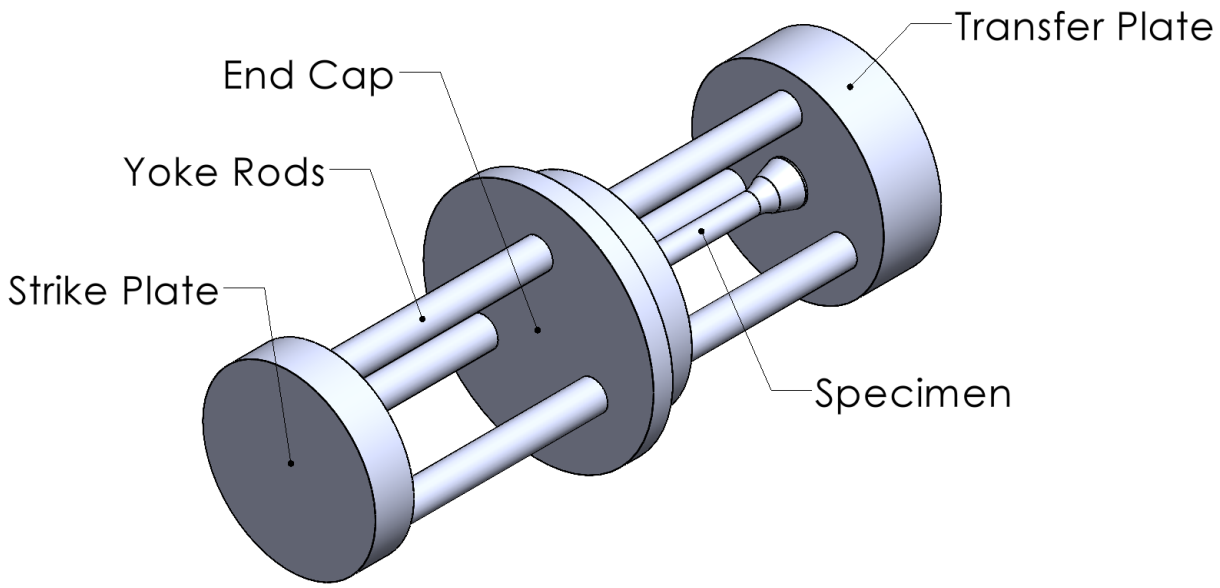

Figure 5.7 Frontal Isometric View of Defeatured Tension Yoke

Chapter 6

Tension Yoke Analysis

6.1 Preprocessing

Utilizing the same settings as the benchmark models, namely the material properties, a few preprocessing settings were adjusted and applied to the modified Hopkinson pressure bar design. To reduce computational time, all applicable components were reduced using symmetry as previously mentioned in Chapter 4. Additionally, the step time was reduced to 0.65 ms since the reflected waveform of the Hopkinson bar was not significant to the analysis beyond verifying that the wave returns after reflecting from the far end. This time duration was selected to ensure the complete transmitted waveform in the tensile specimen and Hopkinson bar was captured.

6.1.1 Boundary Conditions

The boundary conditions of the finite element model can be seen in Figure 6.1. Instead of applying the load directly on the end cap, the pressure was instead applied onto the strike plate in a manner similar to the schematic in Figure 5.5. This would create the desired tension yoke action. Various pressure magnitudes were applied to load the specimen such that both purely elastic and elastic-plastic behavior was excited. These behaviors will be explored in more detail in the latter sections of the chapter. Much like the symmetric models in Chapter 4, the exposed internal faces of all the cut components were assigned a zero-displacement boundary condition, as indicated by the orange cones in Figure 6.1, to ensure the model did not deform uncharacteristically normal to the symmetry plane. This preserved the uni-axial motion observed in traditional SHPB systems.

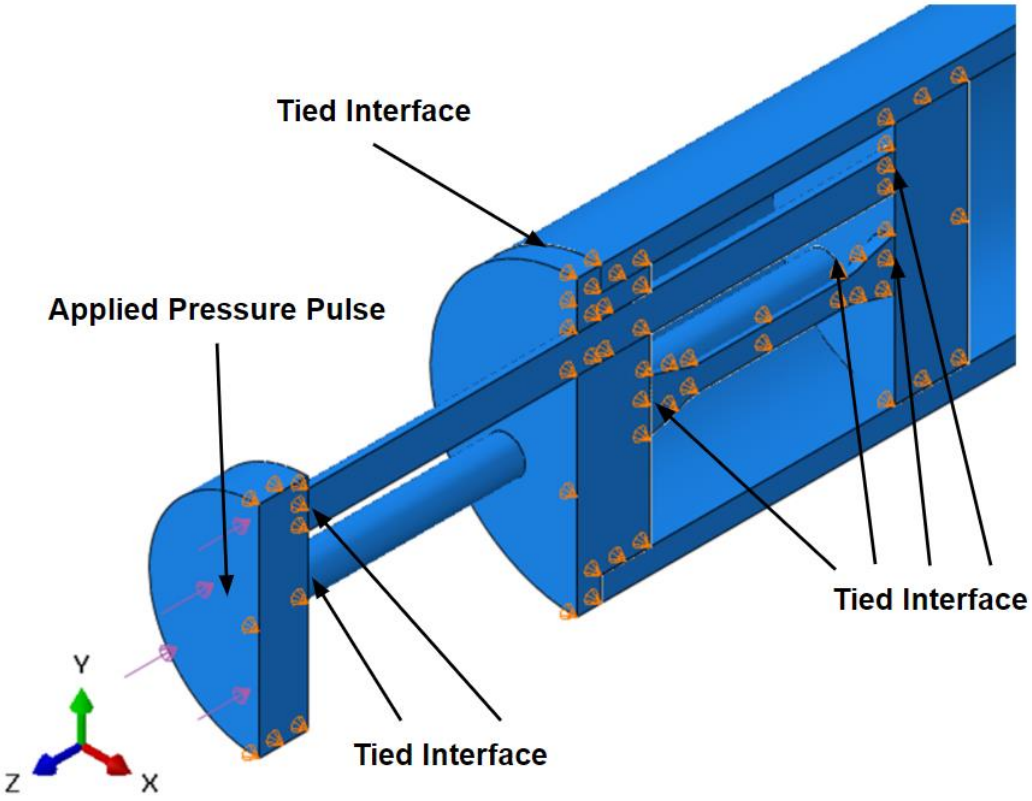

Figure 6.1 Boundary Conditions and Constraints of Modified Design

6.1.2 Constraints

To simulate required contact in the model, tie constraints were applied between the tension yoke rods and the strike and transfer plates, allowing the entire yoke to translate as one component. Similar constraints were applied to the tensile specimen, which connects the end cap with the transfer plate. Additionally, a tie constraint was applied between the end cap where it mates with the Hopkinson bar. These constraints are labeled in Figure 6.1.

6.2 Analytical Methods

As with nearly all finite element models, the finite element solution typically improves in accuracy with increasing mesh density. For the modified design, this meant ensuring the waveform

of the Hopkinson bar was shaped with a high level of accuracy while remaining similar in shape to the waveform in the tensile specimen. Thus, the peak force equivalence condition shown in Equation (8) in Chapter 2 must be satisfied by the model between the Hopkinson bar and the tensile specimen within acceptable error limits. The necessary data was obtained per the methods in Chapter 3 and Chapter 4, querying stresses and strains at an element at the top and bottom of the specimen, at 1.25 inches across its span, as shown in Figure 6.2. This was repeated similarly for the Hopkinson bar approximately 18 inches away from the interface of the end cap and the bar as shown in Figure 6.3. This location was the same location of the strain gauges on the solid bar and hollow bar benchmark models.

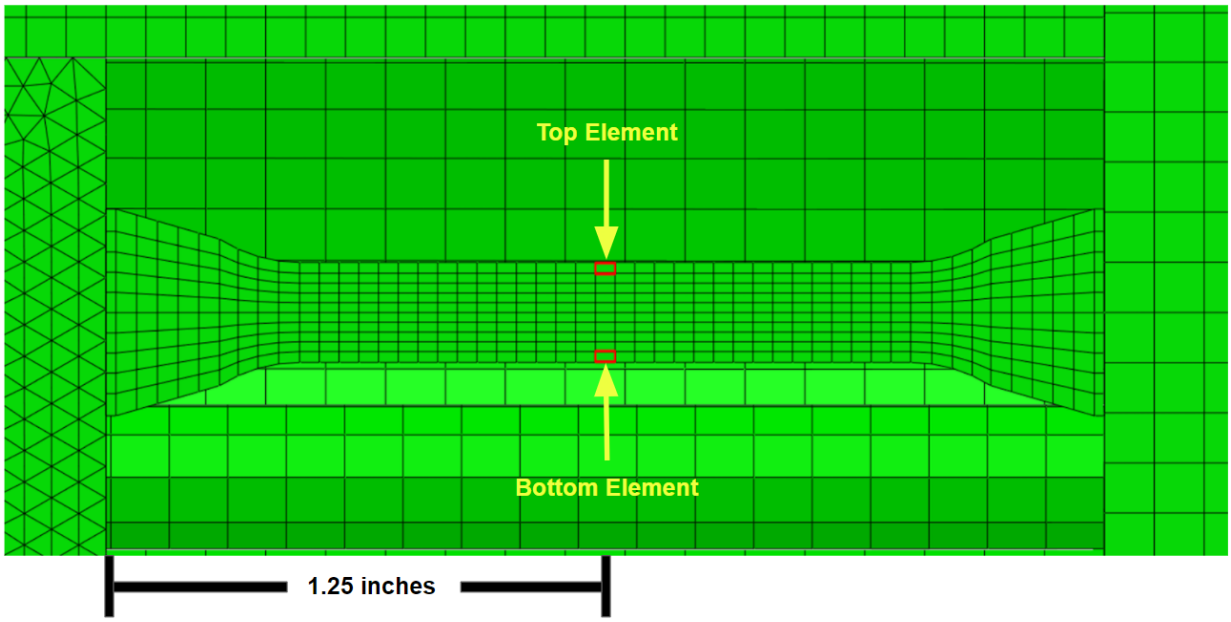

Figure 6.2 Location of Queried Elements on Specimen

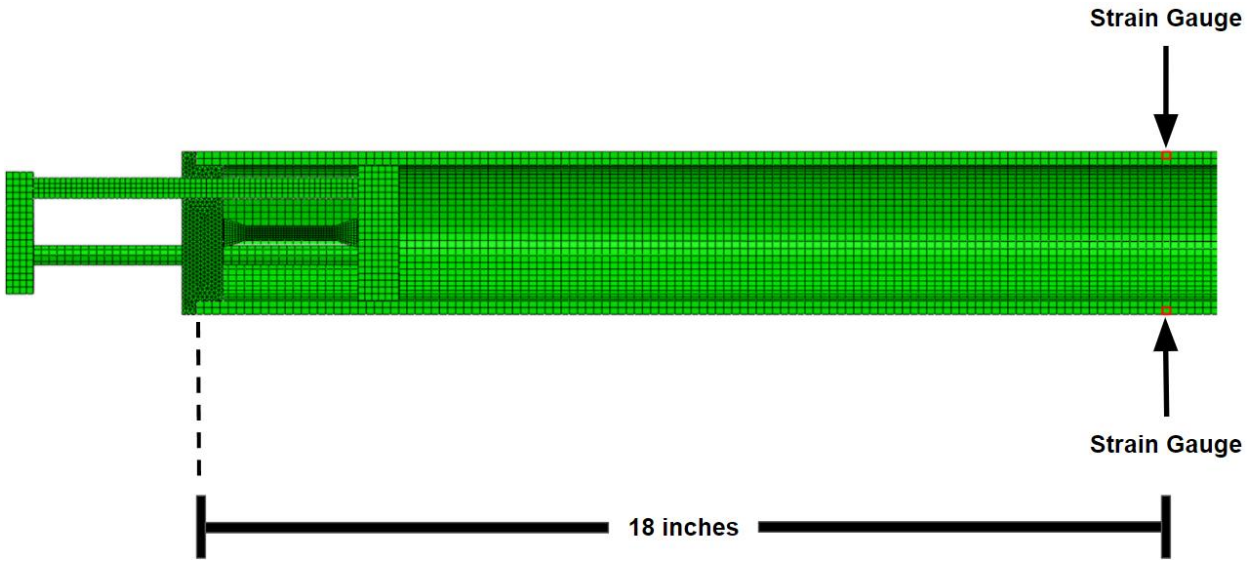

Figure 6.3 Location of Queried Elements on Hopkinson Bar

Both the tensile specimen and Hopkinson bar behaved as transmission components in the modified design, so any extracted strain data from the two components was converted into equivalent forces using Equation (7) corresponding to a transmission bar seen on a typical SHPB system. For the Hopkinson bar, which experienced a transmitted compression wave, the strains were multiplied by a factor of negative one to convert compressive data into tensile data. Finally, the peak forces of the waveforms were compared to determine if the Hopkinson bar can be used as an accurate measurement of the forces developed in the tensile specimen.

6.2.1 Mesh Convergence Studies

Using a half symmetric model allowed for substantial mesh convergence studies. Since the tensile specimen and the Hopkinson bar were the two components of interest, mesh convergence studies were conducted separately on the two components. The loading conditions on the strike plate were maintained at a magnitude of 10,000 psi for each mesh density, similar to how the

benchmark bar models had an applied pressure of 10,000 psi. Additionally, only elastic material properties were simulated during mesh convergence to make the data easier to postprocess and compare. This was done since implementing plastic effects would have led to a higher probability of data fluctuation that would make it difficult to determine if the peak strain was converging for the two primary components. The remaining components of the model were assigned relatively coarse meshes compared to the two primary components since data was not obtained from these components, but they were meshed with enough density to ensure good accuracy of the strain produced in the model.

Strain data was consistently extracted from the model results, organized, and postprocessed using spreadsheet software. Mesh convergence plots were created for the tensile specimen and the Hopkinson bar, comparing the peak strain along the longitudinal direction of the model versus the number of nodes used in the meshes of each component. These plots are shown in Figure 6.4 and Figure 6.5. Figure 6.4 shows strong convergence past the 40,580-node mark for the 10-node quadratic tetrahedral C3D10M element and the 11,592-node mark for the three 8-node linear hexahedral elements (C3D8, C3D8I, C3D8R). Figure 6.5 shows a slight increase in the peak strain for the C3D10M element. The peak strain for this element type was 0.0041 at 180,580 nodes, while the previous mesh containing 136,944 nodes had a peak strain of 0.00403. Nevertheless, the percent difference between the two solutions was 1.68%, an acceptable difference that still showed good convergence.

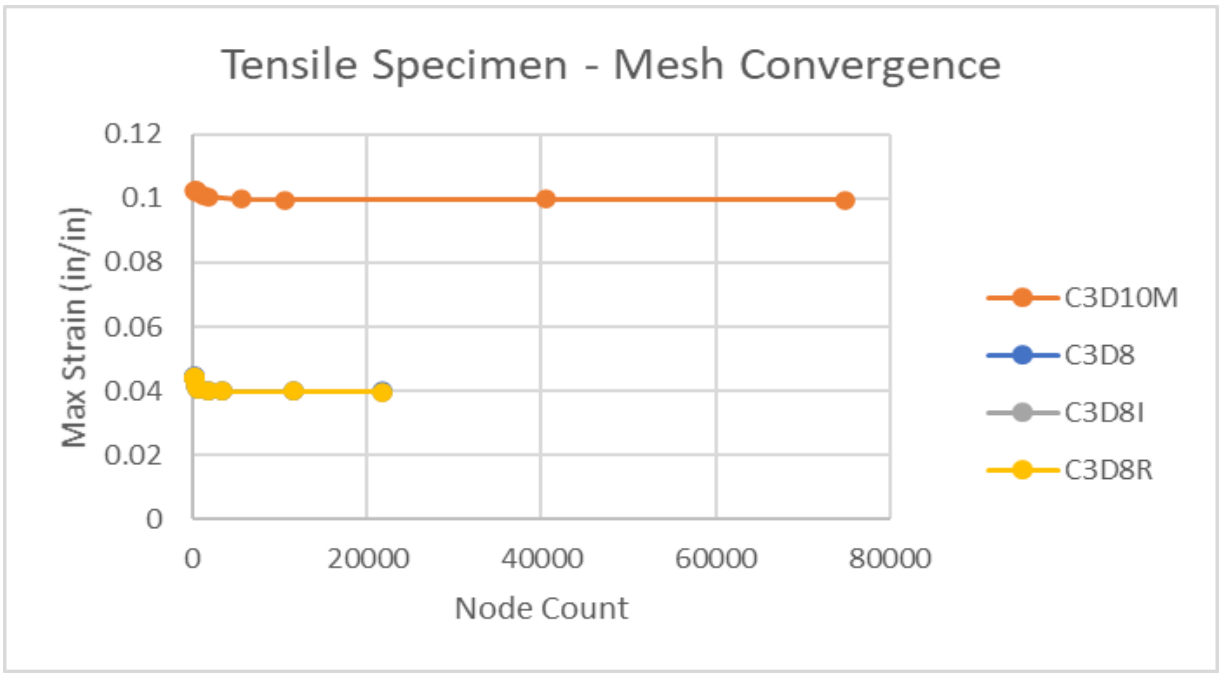

Figure 6.4 Tensile Specimen Mesh Convergence Plot

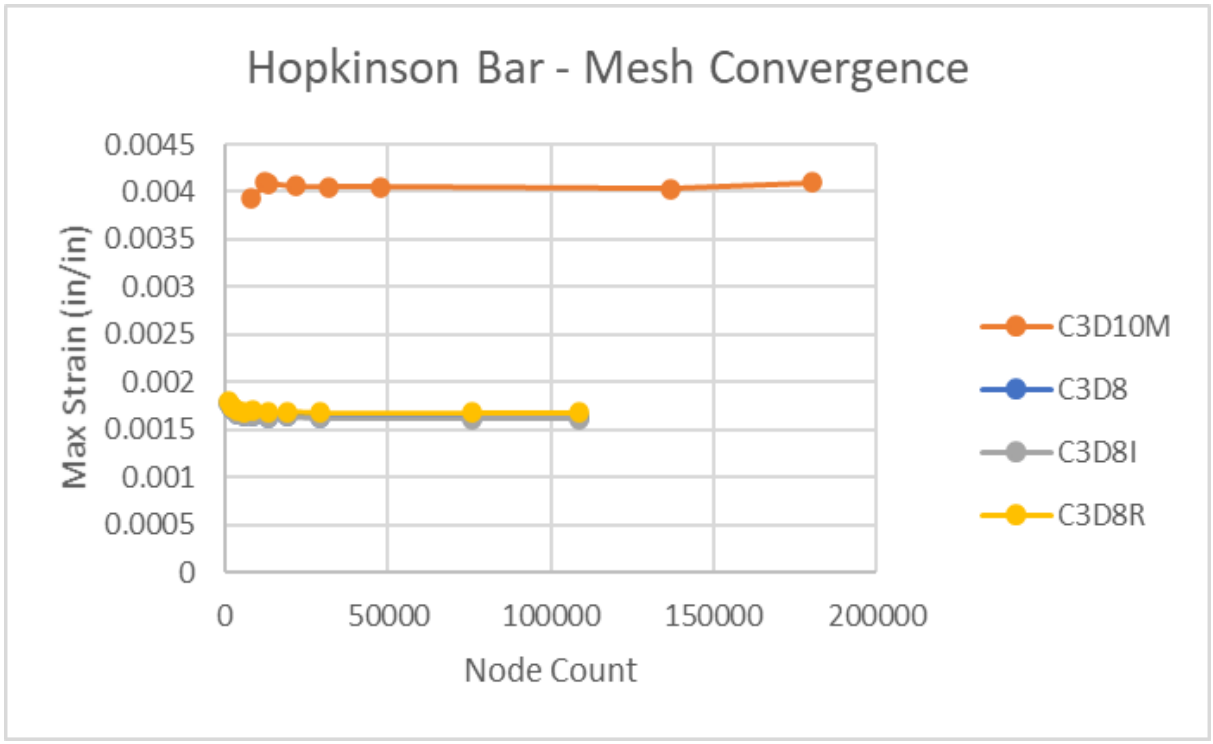

Figure 6.5 Hopkinson Bar Mesh Convergence Plot

All the 8-node linear hexahedral elements (C3D8, C3D8I, C3D8R) recorded similar magnitudes of strain through all the trials. Due to the similarity in solution of all the linear hexahedral elements at each mesh density, effects of shear locking, volumetric locking, and hourglassing were not determined to pose significant analytical issues, making them suitable elements for further analysis. In contrast, the 10-node quadratic tetrahedral C3D10M element, despite its modified formulation, predicted larger strains in both components, making the model appear less stiff than expected. Although it would be easy to infer that the force data between the tensile specimen and Hopkinson bar would match in the case of the C3D10M element alone, the lower stiffness would not be an accurate measure of the stiffness of the physical model if the design were to be manufactured, despite the conservative nature of the results. Hence, the linear hexahedral was a much more desirable element type due to its higher rate of convergence and accuracy in modeling the material behavior of the two primary components. It was additionally a much more desired element because defeaturing the modified design made the geometry easier to mesh. Hexahedral meshes are typically desired if the geometry is relatively simple to mesh and if the mesh elements are mostly rectangular in shape. Thus, with simpler geometry and a high rate of convergence, this ultimately led to the decision of omitting any data obtained that corresponded to the C3D10M element and meshing with hexahedral elements whenever possible.

In addition to disqualifying the C3D10M element type, the C3D8 and C3D8R element types were also omitted, leaving the C3D8I element type as the element to use for analysis. This element was selected due to its implementation of incompatible modes, which capture bending effects much more accurately than the default, fully-integrated C3D8 element type or the reduced integration C3D8R element type. Since the mesh convergence plots for the tensile specimen and Hopkinson bar showed that the peak strains were nearly similar for all three 8-node linear

hexahedral element types, the C3D8I element type was additionally chosen to ensure the most accurate deformation behavior of the model was recorded. Using this element meant that there would be an increase in the computational time, so compromises on the mesh density were made to reduce it, which will be explained later in this section.

The end cap was unable to accept a hexahedral element mesh due to its more complex geometry, and despite trying partitioning schemes to try and make it accommodate hexahedra. To account for this, the end cap was assigned a much smaller seed size with the C3D10M element type to ensure good accuracy of the strain behavior in the end cap.

Based on the mesh convergence plots for the primary components for the C3D8I element type, the solution showed small changes between two different mesh densities at 3,380 nodes and 11,592 nodes for the tensile specimen. The seed sizes for these two mesh densities on the tensile specimen were 0.05 inches and 0.03125 inches, respectively. The mesh with 3,380 nodes recorded a peak strain of 0.04, while the mesh with 11,592 nodes recorded a peak strain of 0.0398, which was a difference of 0.5%. Similarly, there were small changes in the solution between 75,690 nodes and 108,972 nodes for the Hopkinson bar. The seed sizes for these two mesh densities on the Hopkinson bar corresponded to 0.15 inches and 0.125 inches, respectively. The mesh with 75,690 nodes recorded a peak strain of 0.00162, while the mesh with 108,972 nodes recorded a peak strain of 0.00161, which was a difference of 0.05%. The model with 3,380 nodes on the tensile specimen and 75,690 nodes on the Hopkinson bar is shown in Figure 6.6. The model with 11,592 nodes on the tensile specimen and 108,972 nodes on the Hopkinson bar is shown in Figure 6.7.

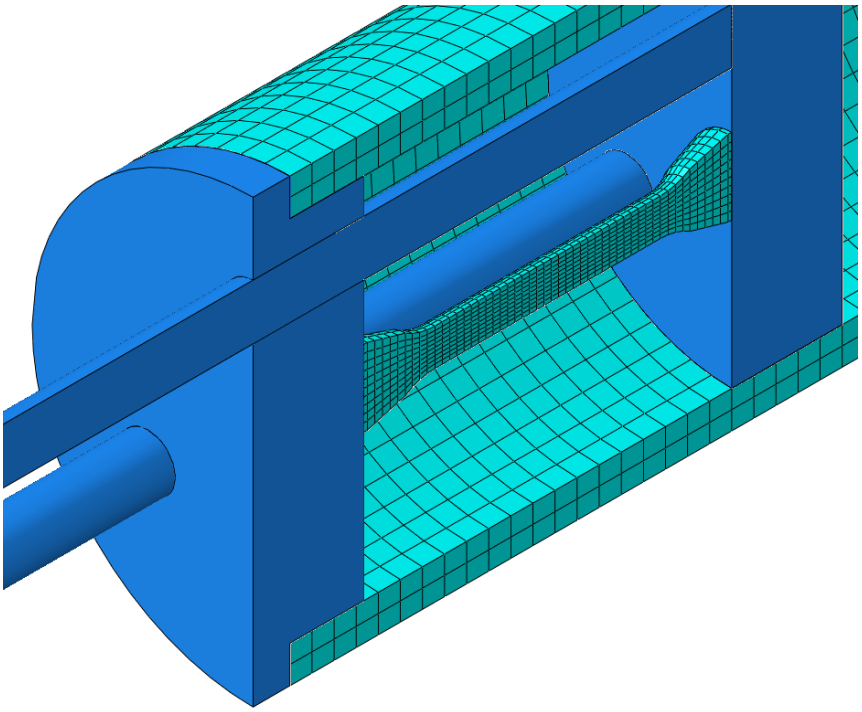

Figure 6.6 3,380-Node Tensile Specimen and 75,690-Node Hopkinson Bar

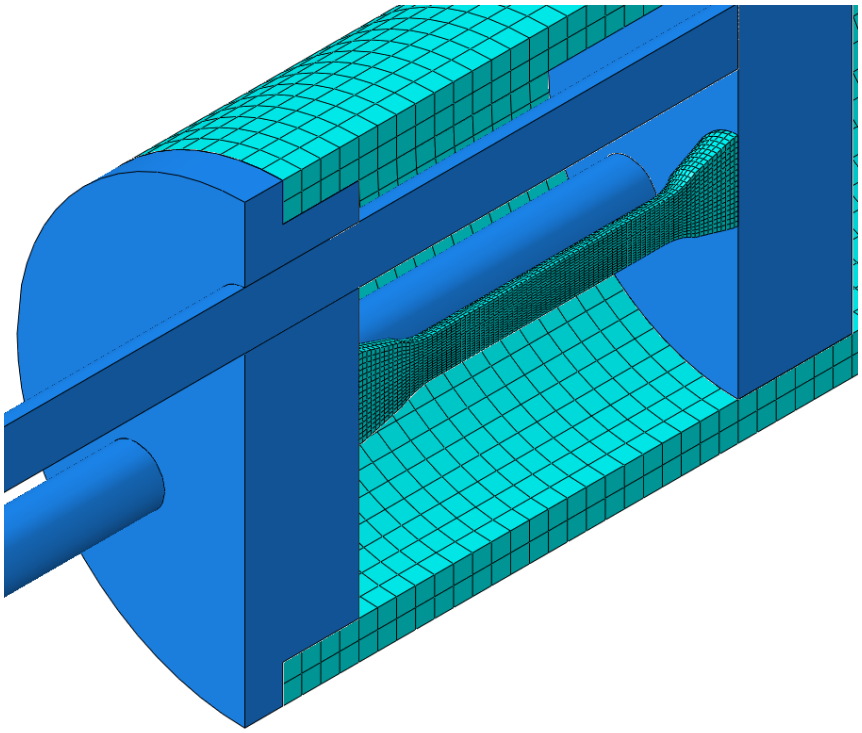

Figure 6.7 11,592-Node Tensile Specimen and 108,972-Node Hopkinson Bar

The mesh settings were finally selected as defined in Table 6.1. As a good compromise between the mesh density and computational time, the mesh seed sizes of 0.05 inches on the tensile specimen and 0.15 inches on the Hopkinson bar were selected over the smaller mesh seed sizes of 0.03125 inches on the tensile specimen and 0.125 inches on the Hopkinson bar. The larger seed sizes were chosen since the difference in solution between the two mesh densities for both components were very small, being 0.5% for the tensile specimen 0.05% for the Hopkinson bar. Meshing the Hopkinson bar at 0.15 inches ensured at least two elements went through the thickness of the bar to accurately capture slight bending effects. Additionally, meshing the Hopkinson bar with a seed size significantly lower than 0.125 inches caused the node limit to be exceeded, so 0.15 inches provided the most optimal mesh density, reduction in computational time, and ensuring the node count was not exceeded. Figure 6.8 shows the final mesh settings applied to the entire model.

Table 6.1 Selected Mesh Settings

Component	Element Type	Seed Size (in)
End Cap	C3D10M	0.08
Strike Plate	C3D8I	0.125
Full Tension Yoke Rod	C3D8I	0.5
Halved Tension Yoke Rod	C3D8I	0.1
Transfer Plate	C3D8I	0.125
Tensile Specimen	C3D8I	0.05
Hopkinson Bar	C3D8I	0.15
Total Number of Nodes		127,171

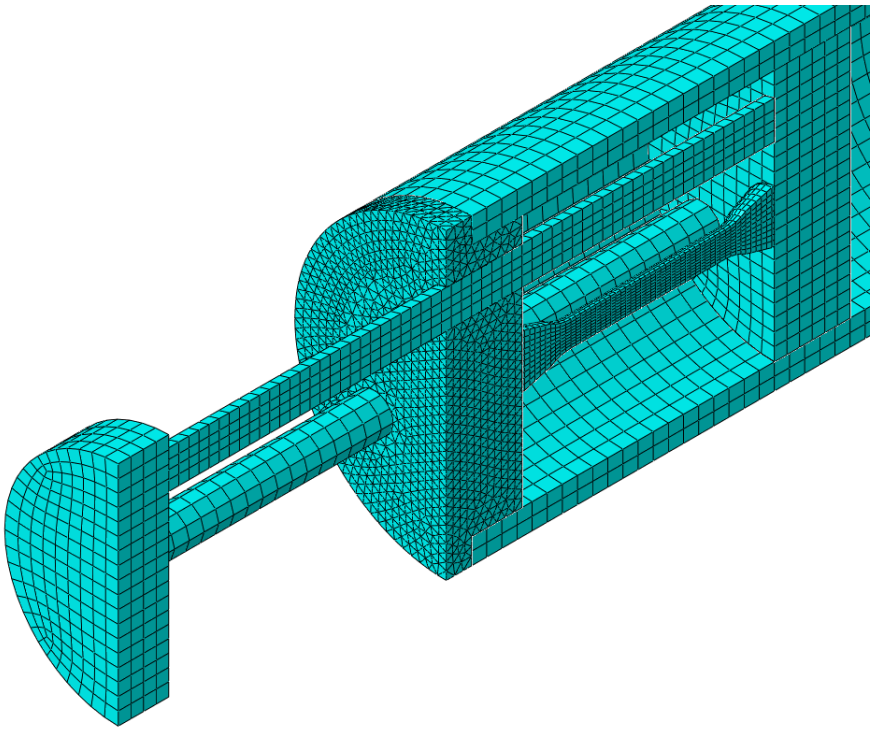

Figure 6.8 Full-Model Mesh with Selected Settings

6.3 Postprocessing

The final stages of research involved analyzing the elastic and plastic response of the primary components, then checking for the satisfaction of the force equilibrium condition of Equation (8) between the tensile specimen and Hopkinson bar, since the primary goal of the analyses was to determine if the Hopkinson bar accurately captured the forces developed in the tensile specimen. In the following sections, data was postprocessed as done in the earlier stages of the thesis, then conclusions were made to determine the feasibility of the proposed design. Since comparing the wave speed was much more complex in the tension yoke, this aspect was ignored and comparison of the peak forces and stress-strain behavior in the tensile specimen and Hopkinson bar were discussed instead.

Visualization of the strain response in the model due to the triangular pulse is shown in Figure 6.9. It was assumed the strain behavior of the model would be similar even if the magnitude of the loading or pulse shape were to be changed. Compressive strain was seen propagating from the strike plate through the yoke rods, while the transfer plate reflected the compression wave as a tension wave, which caused the specimen to experience tensile strain. The end cap reflected the tension wave back into a compression wave through the Hopkinson bar, which experienced compressive strain. Thus, Figure 6.9 shows that the model followed the tension yoke action defined by the schematic in Figure 5.5.

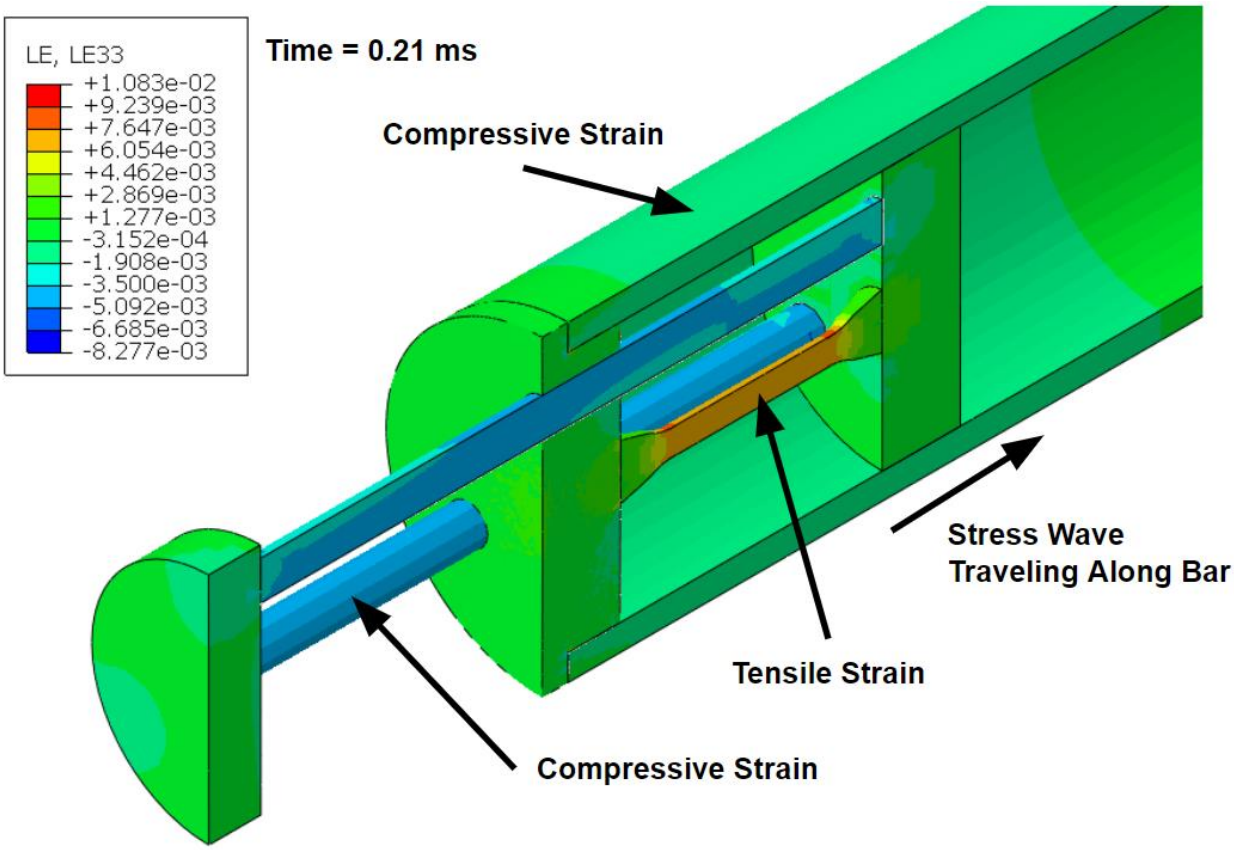

Figure 6.9 Strain Response in Finite Element Model

6.3.1 Elastic Response to a Triangular Pulse

To induce only elastic behavior in the model, the applied pressure was set to a magnitude of 1,000 psi. For the triangular pulse, Figure 6.10 shows the resulting forces induced in the specimen and Hopkinson bar, while Table 6.2 summarizes the results to check if the force equivalence condition was met. The times at which the peak forces occurred for all three curves show that the strike plate achieved its peak force at 0.2 ms, followed by an approximate 0.1-millisecond delay until the peak force was achieved in the specimen, and then another 0.1-millisecond delay for the peak force to be achieved in the Hopkinson bar. The forces between the two components differed by 1.67%, which was a good indicator that the Hopkinson bar could be used as an accurate measure of the forces developed in the tensile specimen for elastic behavior.

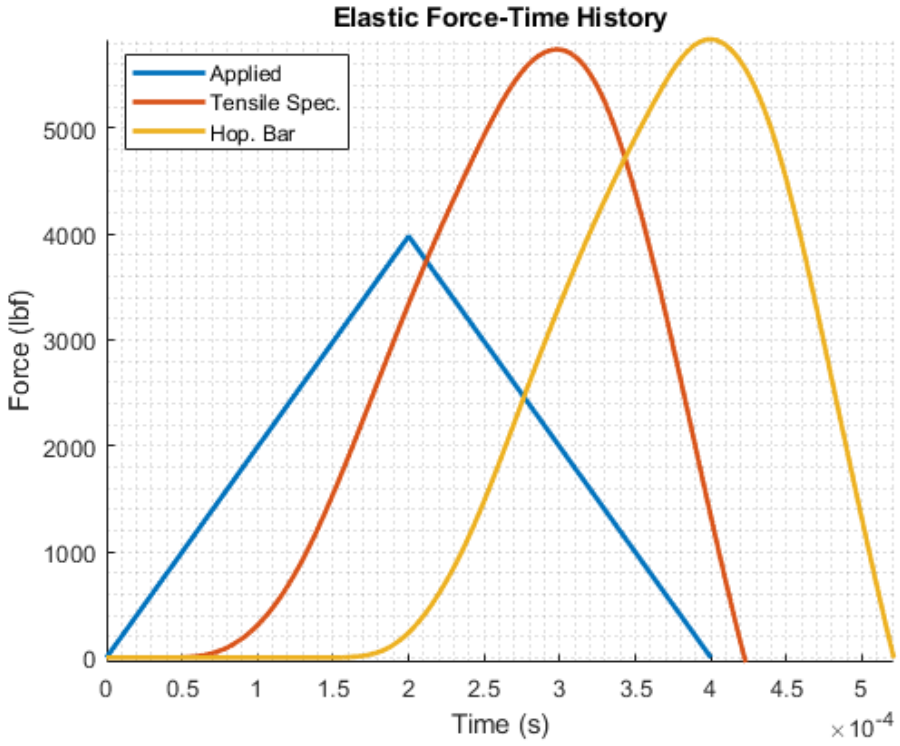

Figure 6.10 Elastic Force Wave Data, Triangular Pulse

Table 6.2 Elastic Analysis Summary, Triangular Pulse

Curve	Peak Force (lbf)	Difference from Applied Pulse	Difference from Specimen	Time to Peak (ms)
Applied	3,976	--	--	0.2
Tensile Specimen	5,739	44.33%	--	0.298
Hopkinson Bar	5,835	46.74%	1.67%	0.4

Despite the strong correlation between the peak forces of the primary components, interesting observations were: 1) the tension yoke modified the shape of the pulse between the applied pulse and what developed in the specimen, 2) the peak force in the specimen was larger than the peak applied force, and 3) the force curves showed no sign of dispersion. This was at first thought to be a physically impossible mechanical event. The applied loading should be the highest load, with some dissipation of loading due to signal loss before propagating to the primary components, which should lead to a small decay in the peak forces calculated for the tensile specimen and Hopkinson bar. Additionally, dispersion should be more prevalent with the triangular pulse due to the sharp rise time of strain it induced. The literature explored in Chapter 2 did not reveal a reason as to why this occurred analytically. However, it was hypothesized that the higher force developed in the specimen was due to the momentum of the tension yoke system. The tension yoke is comprised of three rods that connect the strike plate and transfer plate, as well as the specimen itself. The mass of the tension yoke is accelerated by the impact, and while force is transmitted through the system, the momentum of the yoke is subsequently decelerated by the tensile specimen, thereby inducing more force than the applied pressure pulse.

To explore this hypothesis further, the material properties of the tension yoke, including the end cap, were modified so that their densities were reduced by a factor of 1,000. The densities of the tensile specimen and the Hopkinson bar were retained at their original values. The results of this analysis are shown in Figure 6.11 and Table 6.3.

The plotted force waves showed significant effects of dispersion compared to the applied pulse, as expected for the triangular pulse. The tensile specimen and Hopkinson bar showed an improved correlation with the applied pulse, as evident by the matched shape and small difference in peak forces between all three waveforms. The observed time to the peak force in the tensile specimen and Hopkinson bar was reduced due to the density of the tension yoke and end cap being set to values 1,000 times lower than the aluminum material. This led to a significant increase in the wave speed within the tension yoke, leading to a near-instant wave transmission through the yoke and into the specimen. Since the density of the Hopkinson bar was kept as its original value, the previously observed 0.1-millisecond delay until its peak force was also retained. Additionally, the peak forces in the tensile specimen and Hopkinson bar correlated much more strongly than the previous elastic response shown, differing by only 0.91%.

The conclusion of this side study is that higher peak forces do realistically develop in the specimen, to levels higher than the applied loading, due to the momentum effects of the tension yoke. The force pulse as measured by the Hopkinson bar being different than the applied force pulse is not a concern, as long as the forces in the specimen match the forces measured by the Hopkinson bar, which they do. Also, the low difference in peak force between the Hopkinson bar and tensile specimen showed that quantitatively, the equilibrium condition in Equation (8) was met, but qualitatively, it is not useful for interpretation since the artificial reduction of the densities in the tension yoke and end cap analytically is not physically possible to achieve for the aluminum 6061-T651 material.

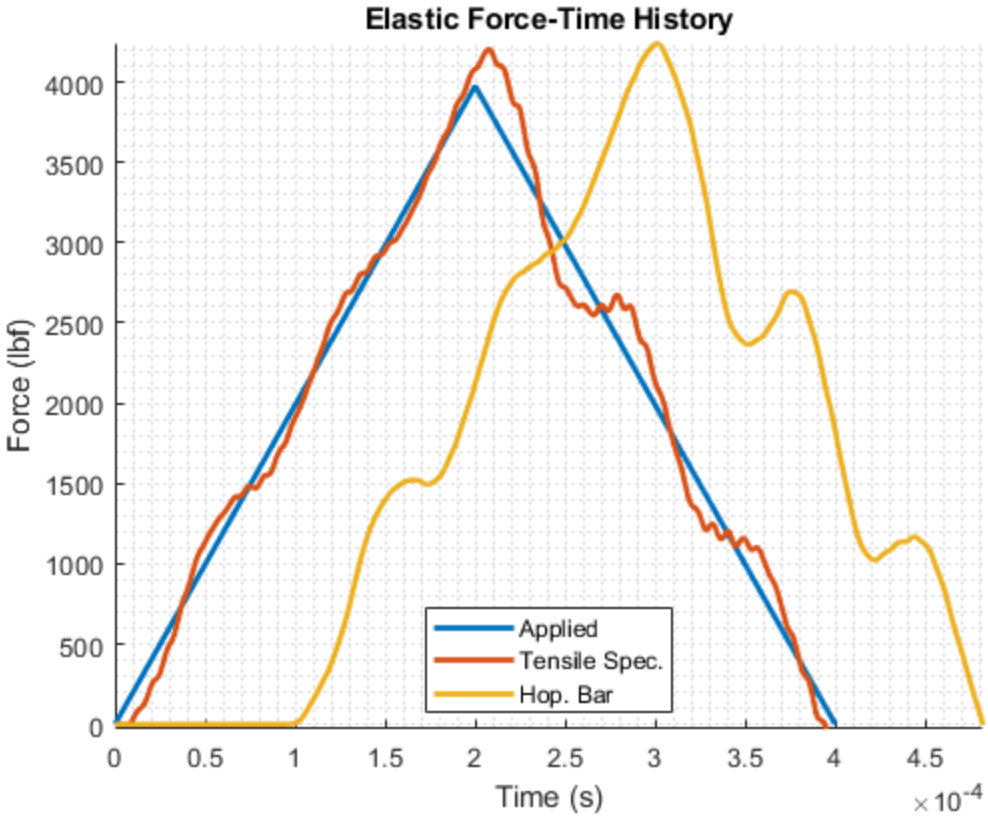

Figure 6.11 Elastic Force Wave Data for Low-Density Model, Triangular Pulse

Table 6.3 Elastic Analysis Summary for Low-Density Model, Triangular Pulse

Curve	Peak Force (lbf)	Difference from Applied Pulse	Difference from Specimen	Time to Peak (ms)
Applied	3,976	--	--	0.2
Tensile Specimen	4,205	5.77%	--	0.208
Hopkinson Bar	4,244	6.73%	0.91%	0.301

6.3.2 Elastic-Plastic Response to a Triangular Pulse

By increasing the applied pressure from 1,000 psi to 3,000 psi, this would induce plasticity in the finite element model of the specimen. Since fracture effects were not implemented in the finite element model, the data including the effects of plasticity was postprocessed slightly differently from the purely elastic data of the model. Most significant to this postprocessing was

omitting waveform data pertaining to the large-strain necking of the tensile specimen and omitting the corresponding waveform data in the Hopkinson bar after the specimen has reached the expected failure strain of 0.08 (8%), since at those strain levels, the specimen would have physically fractured.

The Hopkinson bar and yoke system components by design were assumed to act purely elastically, so these components were modeled as linearly elastic. In contrast, the tensile specimen was expected to deform plastically, as previously described in Chapter 2. To understand the development of plastic deformation in the specimen, the stress-strain data was extracted and used to plot its stress-strain curve, which can be seen in Figure 6.12. The perfectly-plastic behavior that was user-defined from the yield stress data sets can be visualized in the plot, showing that the model produced the desired plastic effects consistent with Figures 3.26, 3.29, and 4.5 pertaining to the test specimen benchmark model.

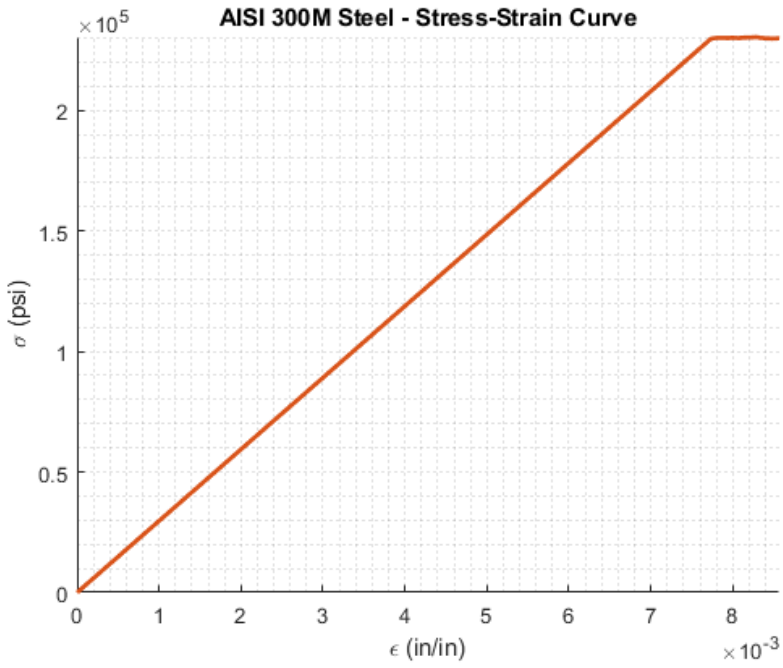

Figure 6.12 AISI 300M Steel Material Behavior for Tensile Specimen, Triangular Pulse

Upon verification of the stress-strain behavior in the specimen, the force-time histories were plotted as seen in Figure 6.13. The plastic force histories showed much different behavior than what was seen in the elastic-only response. The tensile specimen force contained a linearly-declining wave propagation zone corresponding to its perfectly-plastic behavior, followed by the drop in force due to the wave propagating past the elements that were queried for data acquisition. The Hopkinson bar force plateaued briefly before rising to its peak force and then oscillating down and back up to a slightly lower peak than the first before decaying as expected. The observed waveforms were a result of the plastic effects in the tensile specimen.

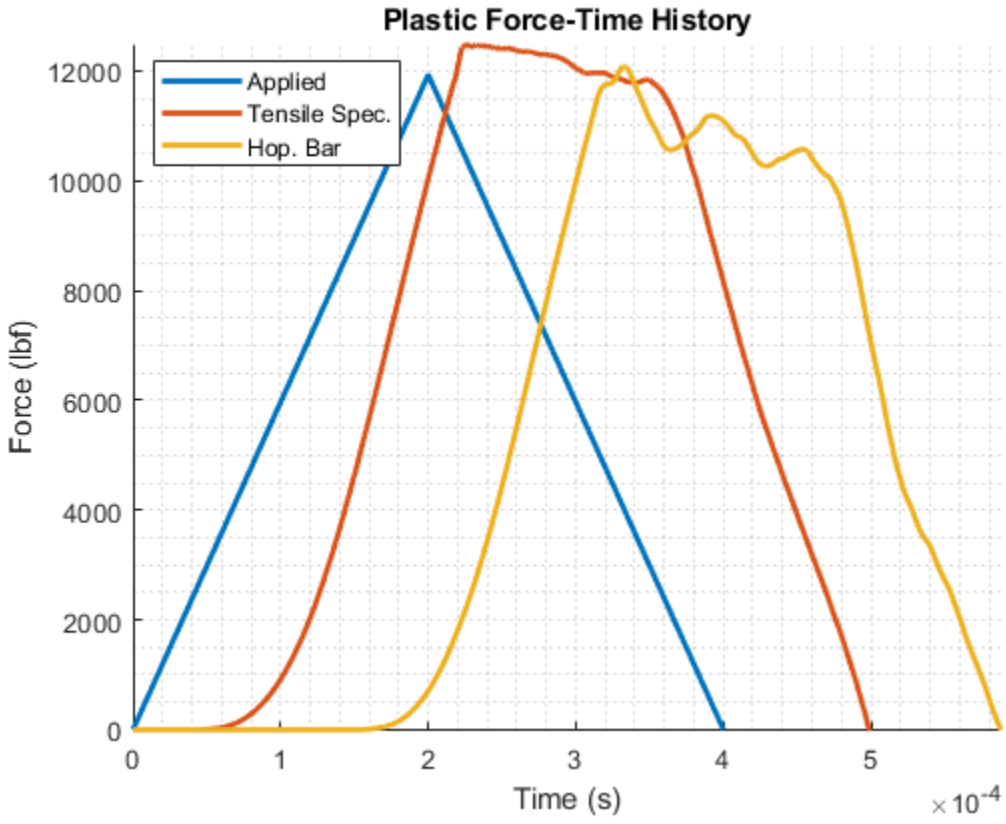

Figure 6.13 Plastic Force Wave Data, Triangular Pulse

Looking at Figure 6.12, the tensile specimen was expected to rupture past its failure strain of 8%, but this strain does not appear to be achieved based on Figure 6.14, where the peak strain was observed to be 0.00857, occurring at a time of 0.226 ms. After reaching the peak, the strain starts to decay (see Figure 6.14) while the specimen is continuing to deform plastically, including localized necking at locations away from where data was queried. Due to this localized necking of the specimen, the strain increases within the necking region instead. At the same time, the reducing cross-sectional area of the necking region causes an unloading of the specimen at the data query locations, thus giving an apparent decrease in strain after the 0.00857 peak as seen in Figure 6.14. In fact, the strain is increasing greatly within the localized necking regions.

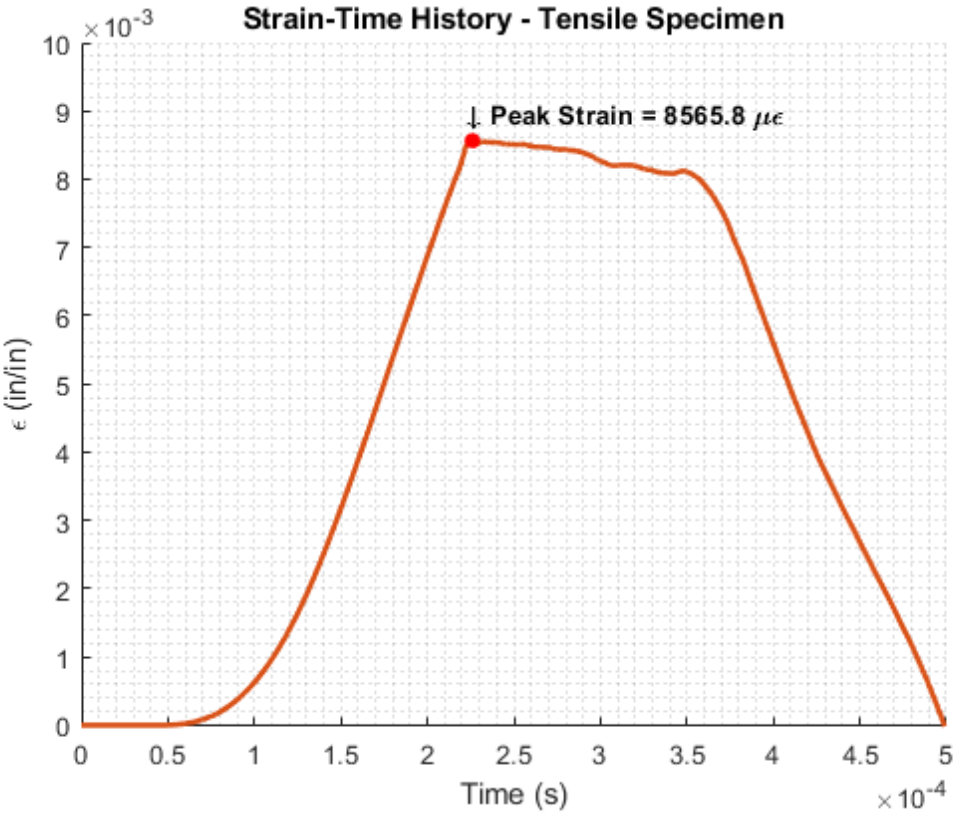

Figure 6.14 Strain-Time History of Tensile Specimen, Triangular Pulse

The necking of the specimen can be seen more clearly in Figure 6.15 and Figure 6.16. Figure 6.15 shows the strain in the specimen at 0.226 ms, which was the time when the peak force was achieved in the specimen at the locations of data extraction. Figure 6.16 shows the strain in the specimen at 0.3 ms, which was the time when the peak strain within the necked region reaches ~0.08 (8%) and when the specimen would be expected to fail. The two figures show how over the course of the analysis, the necking becomes much more prominent in regions away from the specimen center where the data on the tensile specimen was extracted, as evident by the red contours indicating higher tensile strain than the surrounding contours. The strain is reduced at the locations outside of the necking regions, including where the data was extracted, due to the necking-induced reduction of the cross-sectional area combined with increased localized elongation within these zones. Figure 6.15 shows that potential necking regions begin to form, but the failure strain of 0.08 has not yet been reached, since the peak strain shown in the contour plot legend is only 0.0122 (1.2%).

In Figure 6.16, the necking becomes much more prominent. It is seen in the contour plot legend that the peak strain at 0.3 ms was calculated as 0.081 (8.1%), which just exceeds the failure strain of 8% as previously mentioned in Chapter 3 for AISI 300M steel. Therefore, the necking region shown in Figure 6.16 of the specimen at the time of 0.3 ms should be considered as the time corresponding to the component rupturing before the end of the analysis would have been reached, which goes until 0.65 ms.

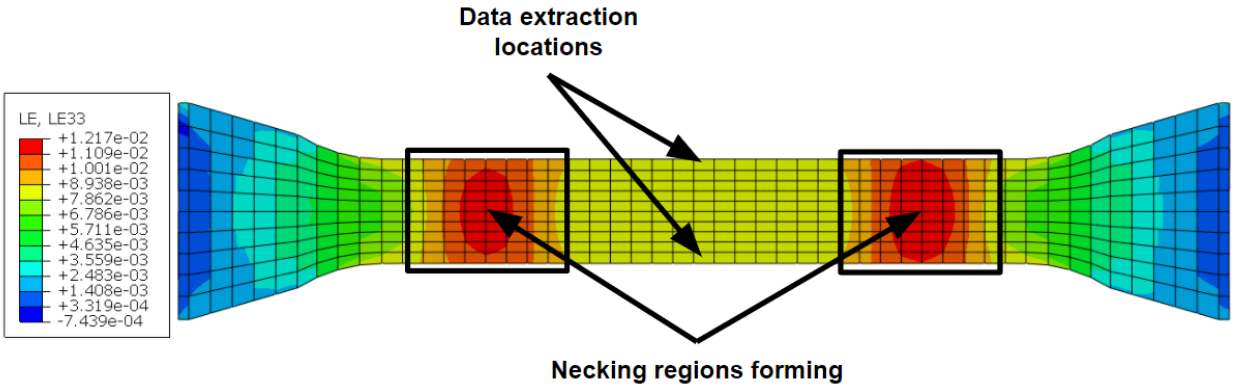

Figure 6.15 Strain Response in Tensile Specimen at 0.226 ms

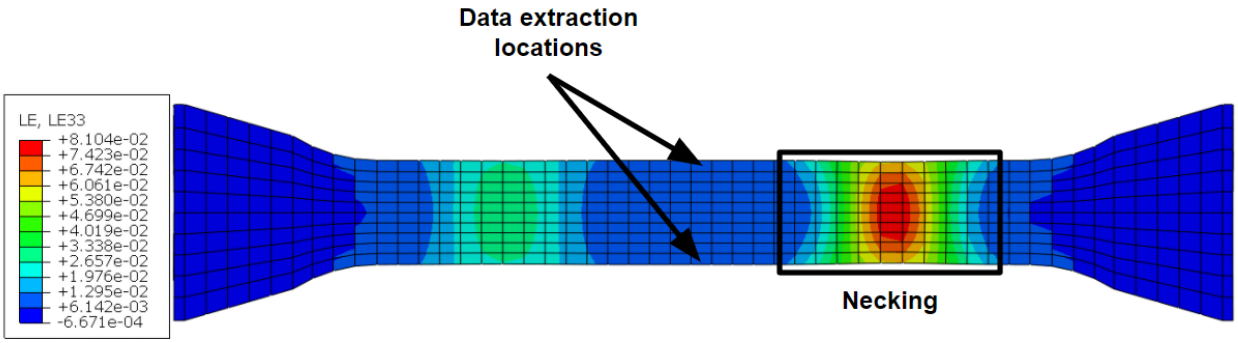

Figure 6.16 Strain Response in Tensile Specimen at 0.3 ms

Since the specimen would have failed at 0.3 ms, the postprocessed waveforms had to be cropped after that time. This meant that any data past that point was assumed to be non-physical and thus, insignificant for discussion. However, since the data was queried at locations away from the necking region, omitting the data accurately was much more difficult since the strains were different at those locations. Instead, the peak forces achieved where the data was extracted was used as the point to cut off the data since after the peak force is achieved at those locations, the elements begin to unload, signifying necking has begun as shown in Figure 6.16. This provides a simpler point of comparison of the peak forces of the specimen and Hopkinson bar in order to

check if the force equivalence condition shown in Equation (8) is satisfied. The cutoff of the plastic forces can be seen in Figure 6.17. Peak forces and time delays were compared per the same procedure as the purely elastic case, with the results summarized in Table 6.4. An interesting observation was that the differences in the peak forces of the primary components relative to the applied pulse were much more acceptable compared to the elastic-only response, with the peak difference being 4.69% between the applied pulse and the specimen. Additionally, the difference between the peak forces of the primary components themselves was 3.23%, an acceptable difference that showed that the Hopkinson bar can still accurately quantify the forces in the tensile specimen, despite effects of plasticity, while still remaining within reasonable error limits. However, the peak force of the applied pulse was still lower than the peak force in the specimen, which leads back to the hypothesis that the momentum effects of the tension yoke may be amplifying the forces in the specimen. The time delay to the peak force in the tensile specimen was much lower, having a delay of 0.026 ms from the time the peak force on the strike plate was achieved. Regardless, the Hopkinson bar consistently achieved its peak approximately 0.1 ms from the time the peak force was achieved in the tensile specimen, owing to the consistency of how long it took for the transmitted wave to propagate from the end cap to the location of the strain gauges 18 inches away from the end cap and Hopkinson bar interface.

An important takeaway of the postprocessing for the elastic-plastic behavior of the model is that although the strain-time history in Figure 6.14 shows that the tensile specimen reaches a peak strain at the locations where the data was extracted, this value may not be indicative of failure in the specimen. This is a significant aspect related to the experimental implementation of this testing apparatus, as strain gauges applied to the specimen would likely be located at the specimen's center and it is generally unknown where localized necking would develop. The data

produced by the model with strain read from the specimen center, while missing the actual peak strains in the localized necking zones, is representative of the experimental response, which is a key motivation of these analyses.

Even though the failure strain may not be reached where the data was extracted, the strain-time history seen in Figure 6.14 indicates that the specimen has begun necking and that the strain may be increasing elsewhere within the specimen, hinting that failure could occur. Data extraction can be conducted on elements different from the ones highlighted in Figure 6.2 to yield different results. Nevertheless, the next few sections will consistently compare the peak forces of the specimen and the peak forces of the Hopkinson bar where the data was queried as it provides a much more convenient point of comparison to check if Equation (8) is satisfied for the force equivalence condition.

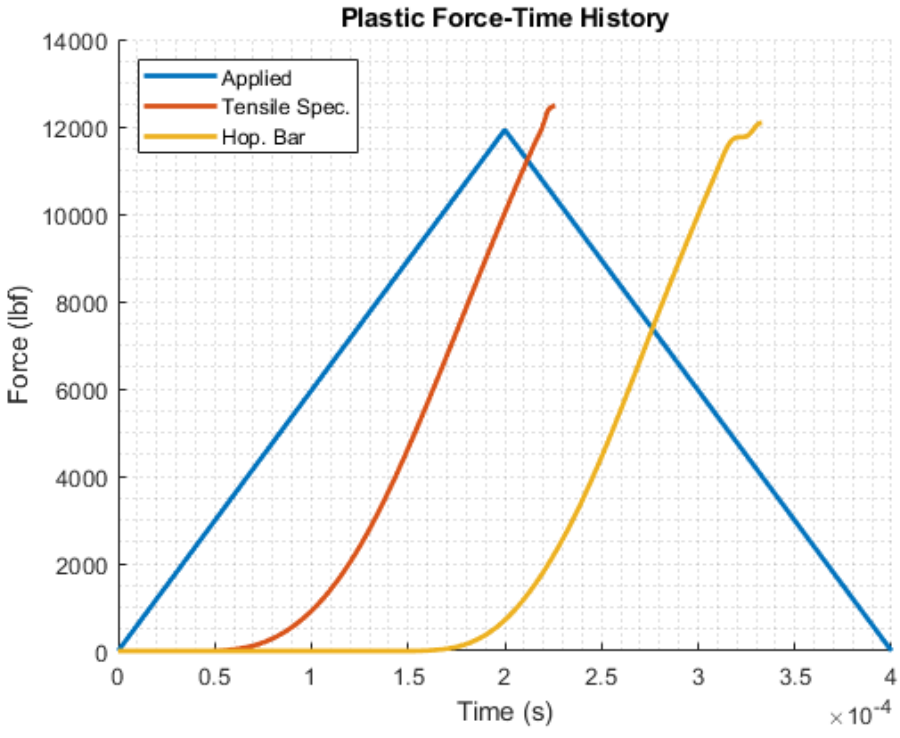

Figure 6.17 Adjusted Plastic Force Wave Data, Triangular Pulse

Table 6.4 Plastic Analysis Summary, Triangular Pulse

Curve	Peak Force (lbf)	Difference from Applied Pulse	Difference from Specimen	Time to Peak (ms)
Applied	11,928	--	--	0.2
Tensile Specimen	12,150	4.69%	--	0.226
Hopkinson Bar	11,834	1.31%	3.23%	0.333

To quantify the effects of momentum as was done in the case of the elastic-only response, data was obtained for the modified finite element model at an applied pressure of 3,000 psi, which utilized the artificial low-density materials for the tension yoke and the end cap (1,000 times lower than the actual density). The resulting forces are shown in Figure 6.18. Similar to the elastic-only response in the model with the low-density tension yoke components and end cap, dispersion strongly affected the waveforms propagating through the two primary components. It was also observed that despite reducing the density of the tension yoke components and end cap, the peak force in the specimen was still higher than the peak force of the applied pulse.

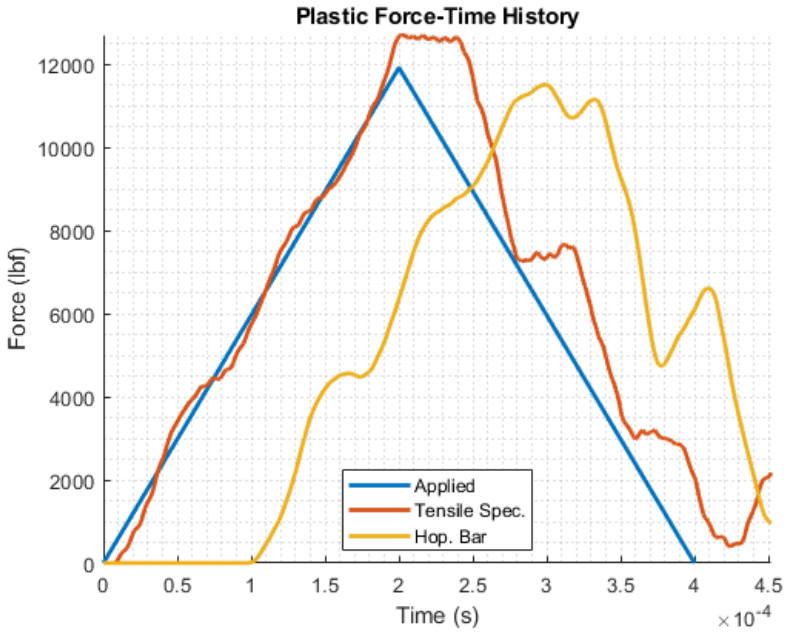

Figure 6.18 Plastic Force Wave Data for Low-Density Model, Triangular Pulse

The cutoff points for the forces in the tensile specimen and Hopkinson bar were determined by first looking at the strain-time history of the tensile specimen, which is shown in Figure 6.19. The peak strain was observed to be 0.00872 occurring at 0.2 ms, which differed by 1.8% from the peak strain of 0.00857 in the model which had the original densities of the tension yoke components and end cap. This difference was due to the effects of dispersion from the triangular pulse slightly affecting the peaks of the strain waveform. Nevertheless, the decay in the strain values past the peak strain can be seen in Figure 6.19, indicating that the specimen is unloading and that necking has begun at a region away from the locations of data extraction.

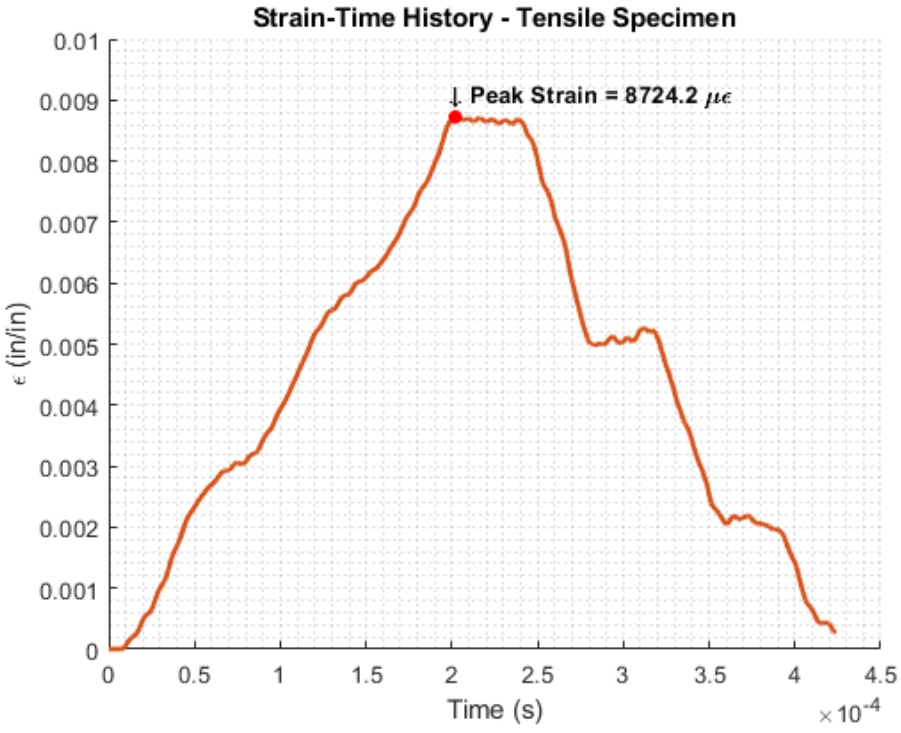

Figure 6.19 Strain-Time History of Specimen in Low-Density Model, Triangular Pulse

Using the peak strain as the cutoff point, the portions of the force curves of the tensile specimen and Hopkinson bar past their peak forces were omitted from the plot since this

corresponded to the peak strain on the tensile specimen's strain-time history and provided a more convenient point of comparison to check if the force equivalence condition shown in Equation (8) was satisfied. This was done to remain consistent with the postprocessing conducted for the elastic-plastic behavior of the model shown in Figure 6.17 if the densities of all the components were retained at their original values. The adjusted curves are shown in Figure 6.20, while Table 6.5 shows the results of the analysis. Peak force results still showed a weak correlation to the applied triangular pulse, yielding a peak difference of 6.63% in the tensile specimen. The forces between the tensile specimen and Hopkinson bar also differed largely by 9.43%. Thus, it was shown how dispersion due to the sharp rise time of the triangular pulse led to the generation of unreliable wave signals in the tensile specimen and Hopkinson bar, which compounded and led to unreliable force correlations between the applied pulse and the calculated pulse responses. As a result, the force equivalence condition shown in Equation (8) was not achieved between the tensile specimen and Hopkinson bar for the elastic-plastic response of the model with the low-density tension yoke and end cap. Nevertheless, since this test case was fictitious, the difference in peak forces between the tensile specimen and the applied pulse did not have much significance. The waveforms associated with the specimen and applied pulse for the case of the low artificial densities had little interpretation beyond understanding how artificially reducing the densities of the tension yoke and end cap altered the wave propagation behavior in the model and affected the differences in the peak forces of the tensile specimen and Hopkinson bar relative to the applied pulse.

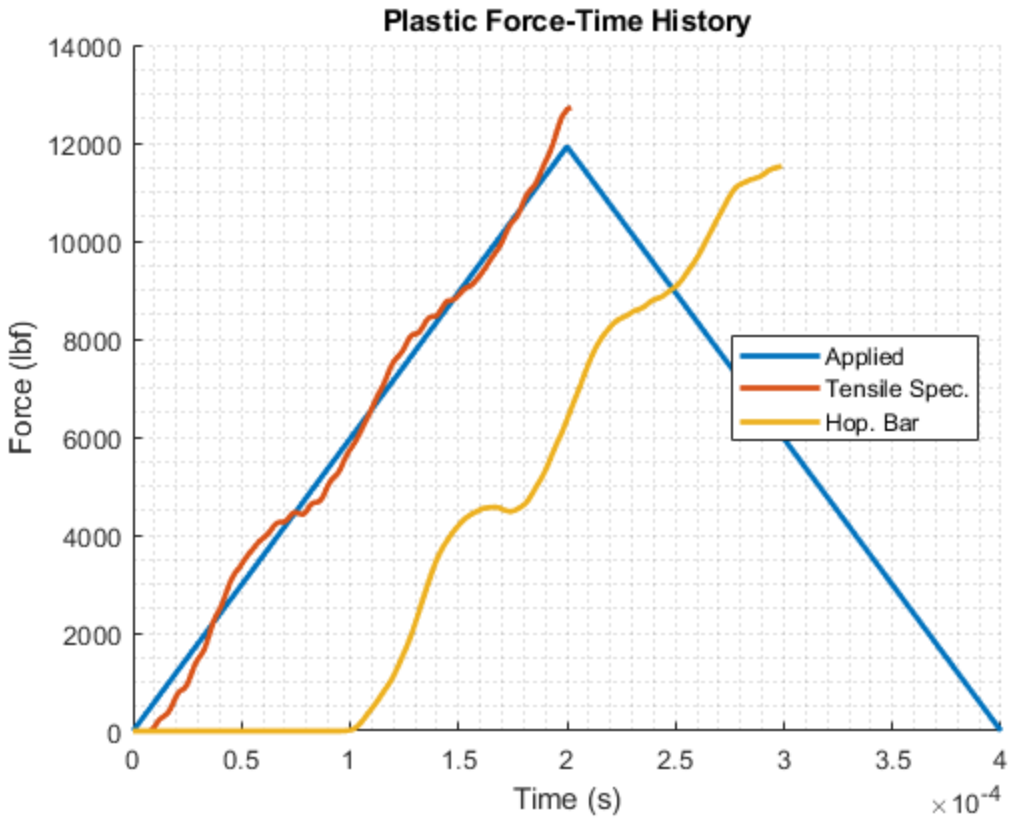

Figure 6.20 Adjusted Plastic Force Wave Data for Low-Density Model, Triangular Pulse

Table 6.5 Plastic Analysis Summary for Low-Density Model, Triangular Pulse

Curve	Peak Force (lbf)	Difference from Applied Pulse	Difference from Specimen	Time to Peak (ms)
Applied	11,928	--	--	0.2
Tensile Specimen	12,719	6.63%	--	0.202
Hopkinson Bar	11,519	3.43%	9.43%	0.299

The strain response of the primary components relative to the triangular pulse, using the artificial, low-density values of the tension yoke and end cap, showed how pulse shapes with sharp rise times lead to the generation of undesirable oscillations that increased dispersion. This affected how well the force waves matched between the tensile specimen and Hopkinson bar, thus leading to larger differences as a result. To address this issue, the remaining sections of this chapter will

discuss the strain response of the primary components if the pulse was modified in shape from triangular to sinusoidal as shown in Figure 3.28.

6.3.3 Elastic Response to a Sinusoidal Pulse

Figure 6.21 shows the forces induced in the two primary components due to the sinusoidal pulse, while Table 6.6 summarizes the results of the elastic response. The sinusoidal pulse produced behavior similar to the triangular pulse when the density of each component in the model was maintained at their original values during analysis. Most notably, the peak applied force was still lower than the peak force in the specimen, differing by 60%. Despite the large difference in force between the applied pulse and the tensile specimen, the strong correlation between the peak forces in the tensile specimen and Hopkinson bar was retained just like the triangular pulse in the elastic-only response, with a difference of 1.3%. Additionally, the shapes of the curves correlated much more strongly compared to the triangular pulse, with the force curves all appearing as sinusoids. The time delays to the peak force in the two primary components behaved similarly to the case of the triangular pulse, with approximately 0.1-ms delays from the peak applied force to the peak specimen force, then from the peak specimen force to the peak Hopkinson bar force.

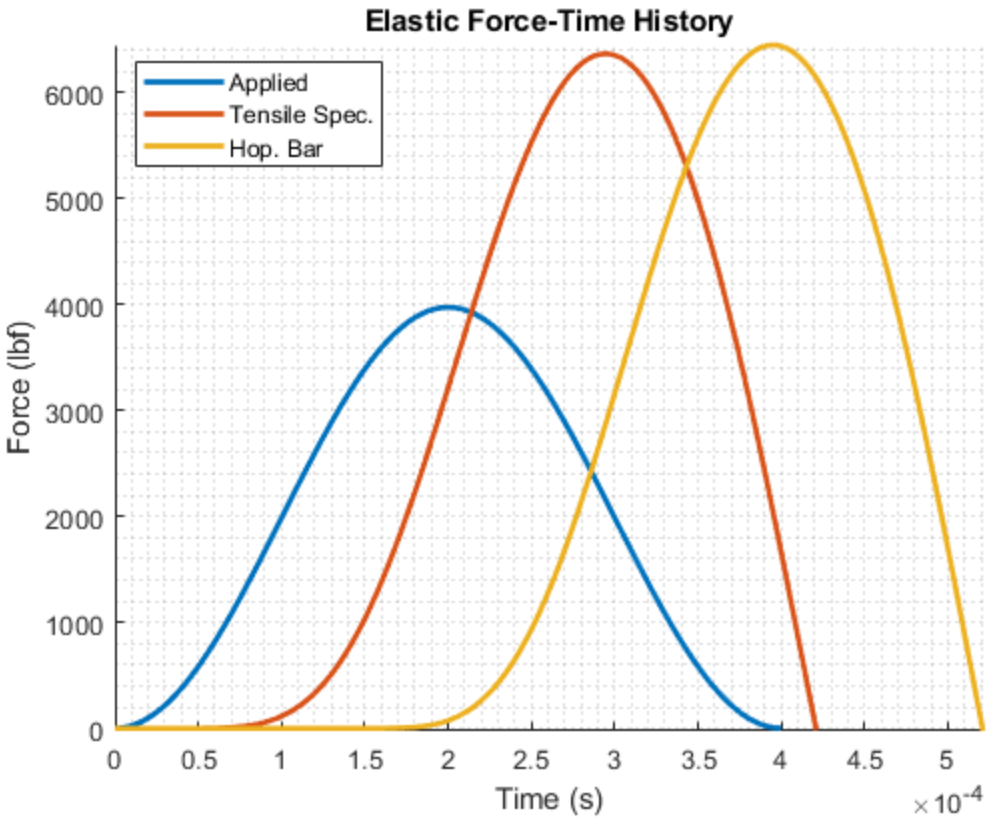

Figure 6.21 Elastic Force Wave Data, Sinusoidal Pulse

Table 6.6 Elastic Analysis Summary, Sinusoidal Pulse

Curve	Peak Force (lbf)	Difference from Applied Pulse	Difference from Specimen	Time to Peak (ms)
Applied	3,976	--	--	0.2
Tensile Specimen	6,370	60.21%	--	0.294
Hopkinson Bar	6,453	62.30%	1.30%	0.395

The effects of momentum were investigated similar to the investigations for the triangular pulse results by setting the tension yoke and end cap densities to artificially low values. The elastic response is shown in Figure 6.22 with results shown in Table 6.7. Dispersion was significantly reduced by inducing a much more gradual rise time in the case of the sinusoidal pulse. This produced a much more desired wave propagation from the yoke into the specimen, and then from

the specimen into the Hopkinson bar. The shape profiles of the curves also correlated well in this model. The differences of the peak forces were under the acceptable 5% deviation. In addition, the difference in force between the tensile specimen and Hopkinson bar was 0.43%, further solidifying the ideology that the Hopkinson bar in this modified system is a component that can be used to accurately measure the force in the tensile specimen under high strain rate tension.

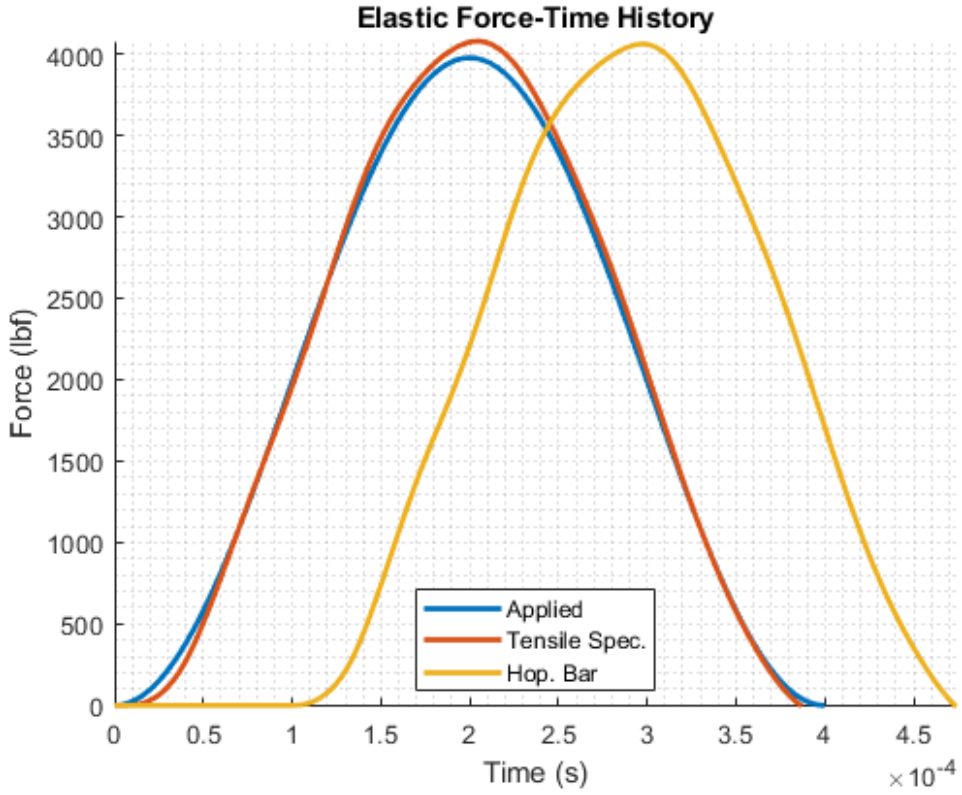

Figure 6.22 Elastic Force Wave Data for Low-Density Model, Sinusoidal Pulse

Table 6.7 Elastic Analysis Summary for Low-Density Model, Sinusoidal Pulse

Curve	Peak Force (lbf)	Difference from Applied Pulse	Difference from Specimen	Time to Peak (ms)
Applied	3,976	--	--	0.2
Tensile Specimen	4,078	2.57%	--	0.204
Hopkinson Bar	4,061	2.13%	0.43%	0.297

6.3.4 Elastic-Plastic Response to a Sinusoidal Pulse

Using an applied pressure of 3,000 psi, the elastic-plastic behavior of the tensile specimen was checked by plotting its stress-strain data as seen in Figure 6.23. The perfectly-plastic behavior can be seen near the end of the stress-strain curve, showing that the model under the influence of the sinusoidal pulse was able to produce the user-defined plastic effects similar to the model analyzed with the triangular pulse.

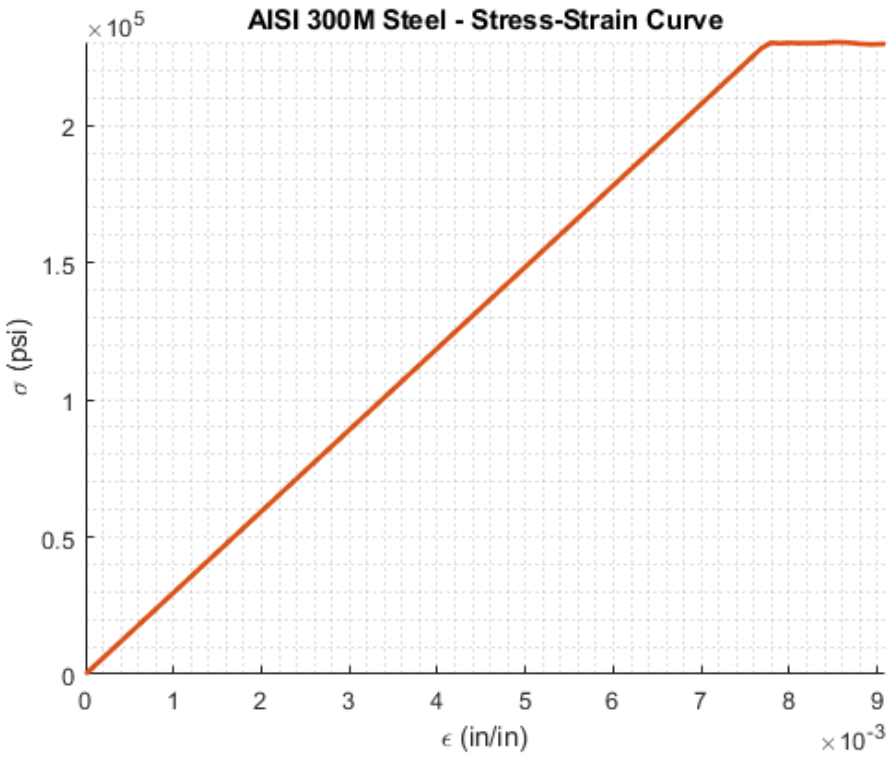

Figure 6.23 AISI 300M Steel Material Behavior for Tensile Specimen, Sinusoidal Pulse

Figure 6.24 shows the plastic force data for the model due to the sinusoidal pulse. The force curves exhibited similar characteristics to the plastic forces of the model from the case of the

triangular pulse, such as the decaying waveforms past the peak force that was related to the necking and eventual rupturing of the tensile specimen.

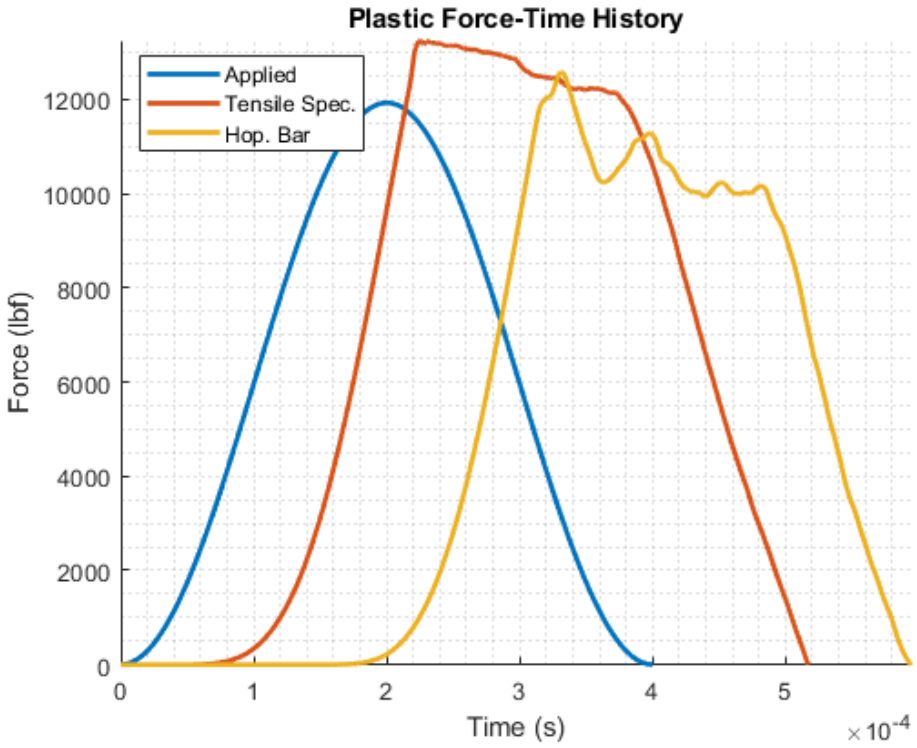

Figure 6.24 Plastic Force Wave Data, Sinusoidal Pulse

To determine the cutoff point for the force curves, the strain-time history of the specimen was plotted in Figure 6.25 to determine the peak strain, as this was where the peak forces in the tensile specimen and Hopkinson bar were compared. The peak strain was observed to be 0.00909 occurring at 0.225 ms, so the force curves shown in Figure 6.24 were cut off accordingly and shown in Figure 6.26.

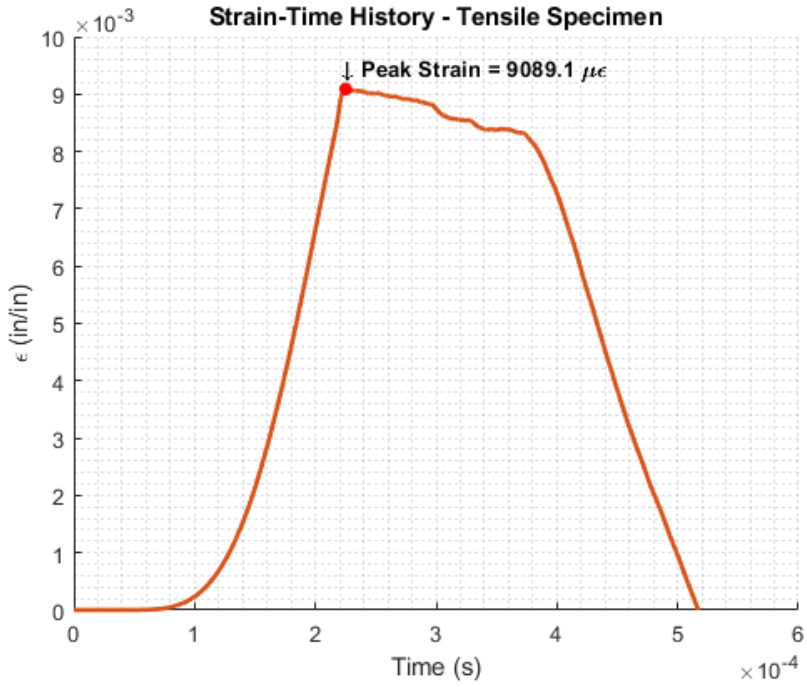

Figure 6.25 Strain-Time History of Tensile Specimen, Sinusoidal Pulse

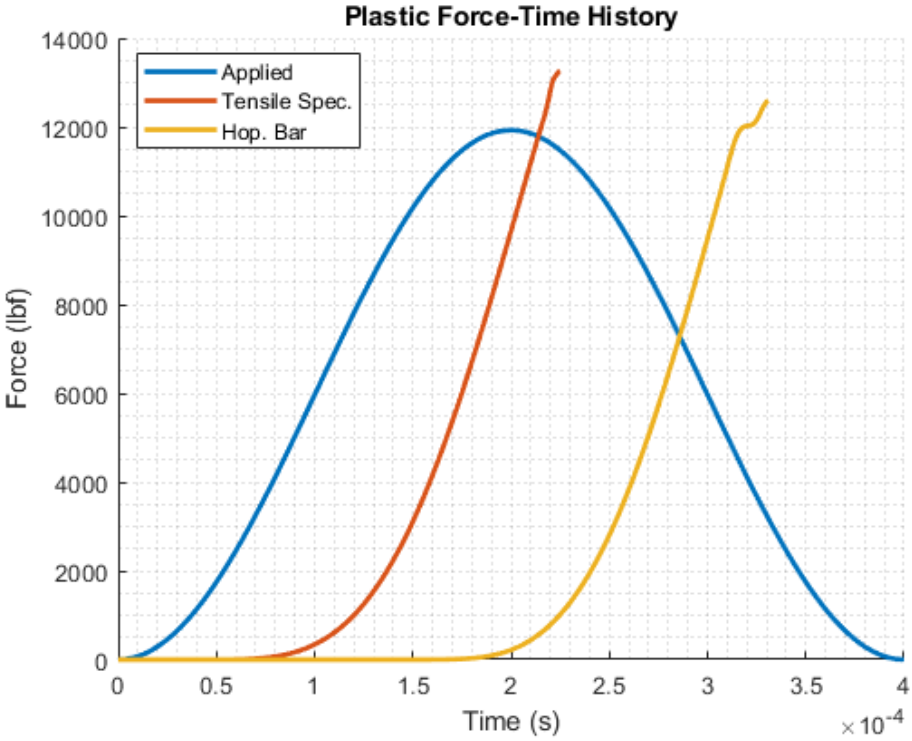

Figure 6.26 Adjusted Plastic Force Wave Data, Sinusoidal Pulse

Table 6.8 summarizes the results of the plastic analysis for the case of the sinusoidal pulse. The differences of the peak forces in the two primary components relative to the applied pulse were above the acceptable 5% difference, strengthening the hypothesis that momentum of the tension yoke could be amplifying the specimen forces, even when the pulse shape was changed. Additionally, the difference between the peak forces of the tensile specimen and the Hopkinson bar was just slightly above the acceptable 5% difference, but this value was considered acceptable and still retained the strong correlation between the peak forces in the two components.

Table 6.8 Plastic Analysis Summary, Sinusoidal Pulse

Curve	Peak Force (lbf)	Difference from Applied Pulse	Difference from Specimen	Time to Peak (ms)
Applied	11,928	--	--	0.2
Tensile Specimen	13,251	11.09%	--	0.225
Hopkinson Bar	12,585	5.50%	5.03%	0.331

The effects of momentum were investigated for the elastic-plastic response by reducing the densities of the tension yoke and the end cap once again by a factor of 1,000. The plastic response of the model is shown in Figure 6.27. There was slight wave distortion in the primary components due to the plasticity of the tensile specimen, making the time delay to the peak force in the specimen appear shorter than the time delay to the peak force in the applied pulse. However, they were assumed to occur at approximately the same time due to the reduced density of the tension yoke transmitting the wave nearly instantly from the strike plate to the transfer plate and into the tensile specimen. Additionally, it was observed that the peak forces in the tensile specimen and Hopkinson bar were lower than the applied peak force. This proved that reducing the effects of momentum produced the expected wave propagation response, with the applied pulse having the largest force, followed by the tensile specimen and the Hopkinson bar having lower peak forces.

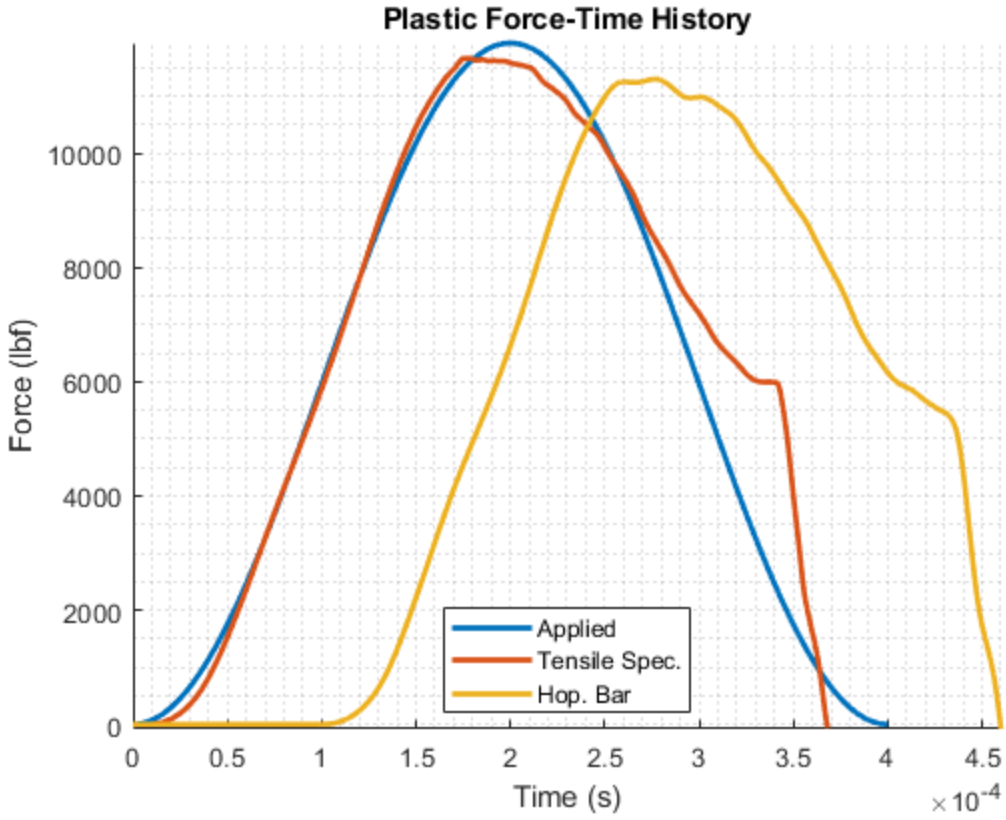

Figure 6.27 Plastic Force Wave Data for Low-Density Model, Sinusoidal Pulse

Similar to the plastic response of the model with the original densities of the tension yoke and end cap, the force curves for the two primary components had to be cut off once the peak force was reached. The cutoff points for the plastic force data of the two primary components were determined by looking at the strain-time history of the tensile specimen shown in Figure 6.28, which had a peak strain of 0.00799 before decaying due to the specimen necking and eventually rupturing. With this peak strain, the adjusted force data is shown in Figure 6.29.

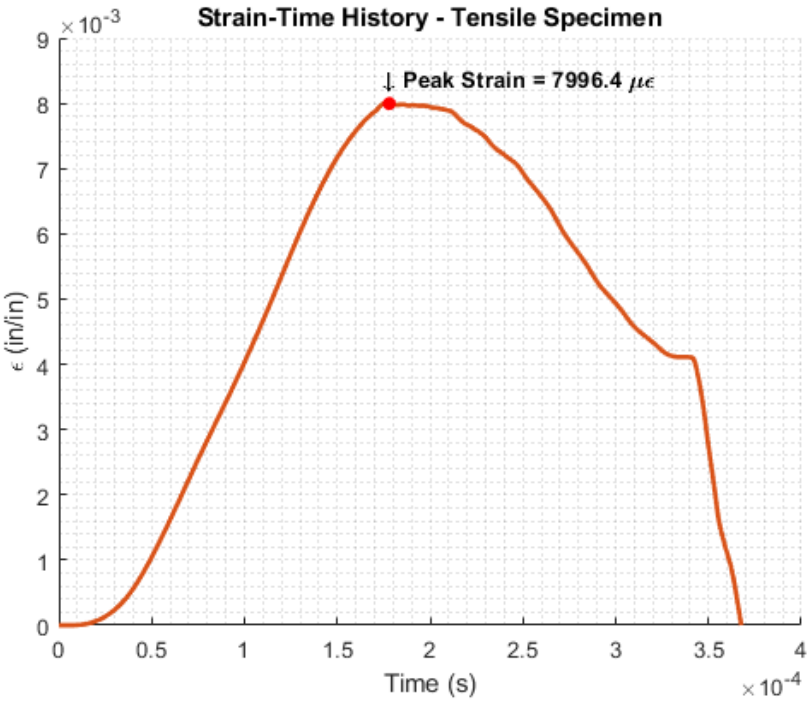

Figure 6.28 Strain-Time History of Specimen in Low-Density Model, Sinusoidal Pulse

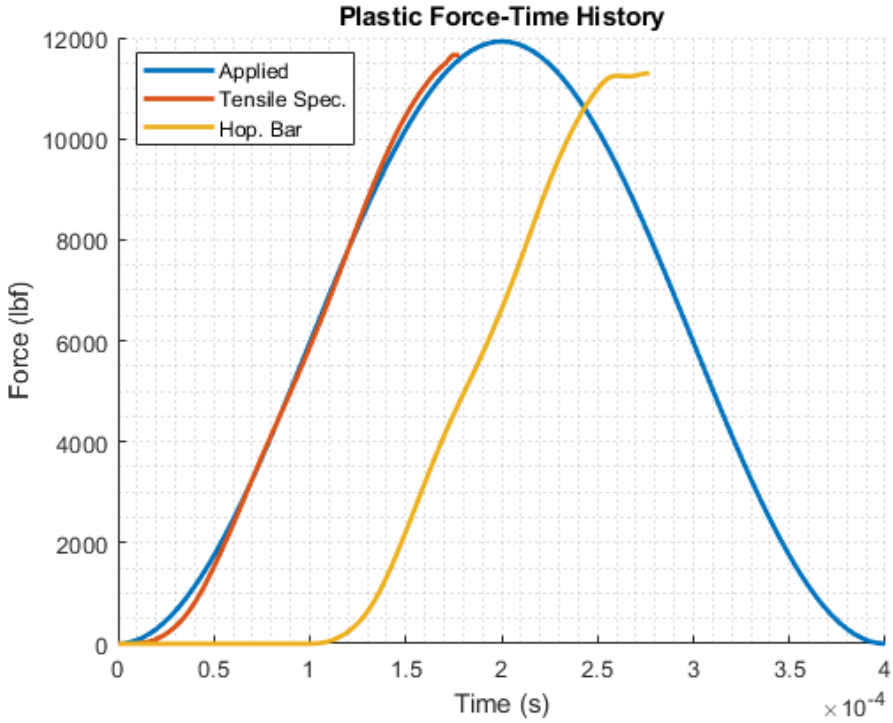

Figure 6.29 Adjusted Plastic Force Wave Data for Low-Density Model, Sinusoidal Pulse

The results of the analysis are shown in Table 6.9. The difference in peak force between the applied pulse and the specimen was 2.27%, which was acceptable. In addition, the difference between the peak force of the two primary components was 3.09%, showing the Hopkinson bar can still be an accurate measure of the forces developed in the tensile specimen.

Table 6.9 Plastic Analysis Summary for Low-Density Model, Sinusoidal Pulse

Curve	Peak Force (lbf)	Difference from Applied Pulse	Difference from Specimen	Time to Peak (ms)
Applied	11,928	--	--	0.2
Tensile Specimen	11,658	2.27%	--	0.178
Hopkinson Bar	11,297	5.29%	3.09%	0.277

It was concluded that the momentum of the tension yoke indeed plays a role in the strains induced in the tensile specimen and Hopkinson bar. By artificially reducing the density of the tension yoke and end cap, the effects of momentum were not as significant and the applied peak force and specimen peak force were closer in magnitude. Additionally, it was proven in this analysis that the force equilibrium condition between the tensile specimen and the Hopkinson bar was satisfied for both the triangular pulse and sinusoidal pulse if the densities of all the components were retained at their original values. This showed that the forces in the Hopkinson bar are a good measure of the forces developed in the tensile specimen if it were to be tested in high strain rate tension.

Chapter 7

Conclusion

The idea of high strain rate tensile testing arose from historical developments leading up to the traditional SHPB system, which has been used to conduct high strain rate compression testing. Various past researchers have presented modified Hopkinson bar systems that allow for high strain rate tensile testing. The developments by these past researchers serve as experimental setups for fundamental material characterization by building a strong foundation for the fundamental research of materials in high strain rate tension. As such, the work presented in this thesis adds to the foundations set by previous researchers and encompasses an area of material testing that can be applied to any industry due to its versatility.

This analytical-based study verified the principles of SHPB systems through the design and analysis of various benchmark models mimicking a Hopkinson bar and test specimen. Cutting the models across planes of symmetry resulted in reduced computational time while still maintaining behavior similar to the full models. Finally, the modified Hopkinson pressure bar system with the tension yoke was analyzed using similar analytical setups established and verified by the benchmark models, and it resulted in desirable wave propagation behavior. This was most apparent due to the strong correlation between the forces developed in the tensile specimen and the forces in the Hopkinson bar, which gave confidence that the response in the Hopkinson bar can be used as an accurate measure of the forces developed in the tensile specimen. Effects of dispersion were also investigated to determine a relation between the applied pressure waveform and the responses in the tensile specimen and Hopkinson bar.

Even with the results presented herein, there are still many unknowns about the modified Hopkinson pressure bar system. Utilizing finite element analysis in an effective way is largely up to the analyst's abilities and experience, and how the problem is converted from the physical domain into the analytical domain. The wide range of options available when conducting finite element analysis leaves a lot of room for modifications to be made to the research presented in this work. Regardless of these improvements, the current studies show potential for the modified Hopkinson bar design with the tension yoke to be used as a functional experimental setup for high strain rate tensile testing.

7.1 Future Studies

Modifying various aspects of the finite element model of the tension yoke, such as including its removed complexities, then reanalyzing its behavior under various pulse shapes can further the validation of the proposed design. Adjusting the pulse durations to be shorter and longer than the durations studied, then analyzing the strain response can also help validate the proposed design. Additional investigations of the effects of momentum on the induced strains in the tensile specimen and Hopkinson bar can be conducted to determine a relation between the amount of force amplification due to momentum to the forces experienced by the two components. Vibrational analysis can also be conducted to determine the input frequency of the applied impact and compare it to the frequency of the tension yoke. Analyzing the input-to-output frequency may offer insight into the larger forces observed in the tensile specimen and Hopkinson bar. Spectral analysis can be conducted to quantify the amount of dispersion and help provide insight into modifications that can be made to the design to shape the pulses propagating through the system during physical experiments or correct effects of dispersion to improve the wave signal output. Finally, future work

would involve the manufacturing and physical experimentation of the modified Hopkinson pressure bar with the proposed tension yoke system. Comparisons with analytical data similar to this research can be made to validate the accuracy of the finite element models and solidify the feasibility of the design.

References

[1] Kaiser, M. A. (1998). *Advancements in the Split Hopkinson Bar Test* (thesis). Virginia Tech, Blacksburg.

[2] Peng, Y., Yin, Y., Xie, P., Wei, X., & Nie, H. (2022). Reliability analysis of arresting hook engaging arresting cable for carrier-based aircraft influenced by multifactors. *Chinese Journal of Aeronautics*. https://doi.org/10.1016/j.cja.2022.01.001

[3] Sharma, S., Chavan, V. M., Agrawal, R. G., Patel, R. J., Kapoor, R., & Chakravartty, J. K. (2011). (rep.). *Split-Hopkinson Pressure Bar: An Experimental Technique for High Strain Rate Tests*. Department of Atomic Energy. Retrieved February 2, 2022, from https://inis.iaea.org/collection/NCLCollectionStore/_Public/42/105/42105051.pdf?r=1.

[4] Harding, J., Wood, E. O., & Campbell, J. D. (1960). Tensile testing of materials at impact rates of strain. *Journal of Mechanical Engineering Science*, *2*(2), 88–96. https://doi.org/10.1243/jmes_jour_1960_002_016_02

[5] Staab, G. H., & Gilat, A. (1991). A Direct-tension Split Hopkinson Bar for High Strain-rate Testing. *Experimental Mechanics*, *31*(3), 232–235. https://doi.org/10.1007/bf02326065

[6] Zhou, J., Pellegrino, A., Heisserer, U., Duke, P. W., Curtis, P. T., Morton, J., Petrinic, N., & Tagarielli, V. L. (2019). A new technique for tensile testing of engineering materials and composites at high strain rates. *Proceedings of the Royal Society A: Mathematical, Physical and Engineering Sciences, 475*(2229). https://doi.org/10.1098/rspa.2019.0310

[7] Zhou, J., Tagarielli, V. L., Heisserer, U., & Curtis, P. T. (2018). An Apparatus for Tensile Testing of Engineering Materials. *Experimental Mechanics*, *58*(6), 941–950. https://doi.org/10.1007/s11340-018-0393-4

[8] Nicholas, T. (1981). Tensile testing of materials at high rates of strain. *Experimental Mechanics*, *21*(5), 177–185. https://doi.org/10.1007/bf02326644

[9] Ellwood, S., Griffiths, L. J., & Parry, D. J. (1982). A tensile technique for materials testing at high strain rates. *Journal of Physics E: Scientific Instruments*, *15*(11), 1169–1172. https://doi.org/10.1088/0022-3735/15/11/011

[10] Lindholm, U. S., & Yeakley, L. M. (1968). High strain-rate testing: Tension and compression. *Experimental Mechanics*, *8*(1), 1–9. https://doi.org/10.1007/bf02326244

[11] Ogawa, K. (1984). Impact-tension compression test by using a split-hopkinson bar. *Experimental Mechanics*, *24*(2), 81–86. https://doi.org/10.1007/bf02324987

[12] Campbell, J. D. (1953). An investigation of the plastic behaviour of metal rods subjected to longitudinal impact. *Journal of the Mechanics and Physics of Solids*, *1*(2), 113–123. https://doi.org/10.1016/0022-5096(53)90015-5

[13] Hopkinson, J. (1872). On the rupture of iron wire by a blow. *Proceedings of the Literary and Philosophical Society of Manchester*, *11*, 40–45.

[14] Hopkinson, J. (1872). Further experiments on the rupture of iron wire. *Proceedings of the Literary and Philosophical Society of Manchester*, *11*, 119–121.

[15] Hopkinson, B. (1914). A method of measuring the pressure produced in the detonation of high explosives or by the impact of Bullets. *Proceedings of the Royal Society of London. Series A, Containing Papers of a Mathematical and Physical Character*, *89*(612), 411–413. https://doi.org/10.1098/rspa.1914.0008

[16] Pochhammer, L. (1876). Ueber die fortpflanzungsgeschwindigkeiten Kleiner Schwingungen in Einem Unbegrenzten isotropen kreiscylinder. *Journal Für Die Reine Und Angewandte Mathematik Band 81*, 324–336. https://doi.org/10.1515/9783112347287-019

[17] Strutt, J. W. (n.d.). On Waves Propagated along the Plane Surface of an Elastic Solid. *Scientific Papers*, 441–447. https://doi.org/10.1017/cbo9780511703973.053

[18] Chree, C. (1886). Longitudinal vibrations of a circular bar. *Quarterly Journal of Pure and Applied Mathematics*, *21*, 287–298.

[19] Chree, C. (1889). The equations of an isotropic elastic solid in polar and cylindrical coordinates, their solutions and applications. *Transactions of the Cambridge Philosophical Society*, *14*, 250.

[20] Gadzhibekov, T. A. (2021). Longitudinal Pochhammer - Chree Waves. Secular Equations and Spectral Analysis. *IOP Conference Series: Earth and Environmental Science*, *666*(2), 022020. https://doi.org/10.1088/1755-1315/666/2/022020

[21] Karpfinger, F., Gurevich, B., & Bakulin, A. (2007). Computing borehole modes with spectral method. *SEG Technical Program Expanded Abstracts 2007*, 333–337. https://doi.org/10.1190/1.2792437

[22] Love, A. E. H. (1911). *Some Problems of Geodynamics*. Cambridge University Press.

[23] Kiełczyński, P. (2018). Properties and applications of love surface waves in seismology and biosensors. *Surface Waves - New Trends and Developments*. https://doi.org/10.5772/intechopen.75479

[24] Bancroft, D. (1941). The velocity of longitudinal waves in cylindrical bars. *Physical Review*, *59*(7), 588–593. https://doi.org/10.1103/physrev.59.588

[25] Achenbach, J. D. (1973). *Wave Propagation in Elastic Solids*. Elsevier.

[26] Tasneem, N. (2005). *Study of wave shaping techniques of Split Hopkinson pressure bar using finite element analysis* (thesis). Wichita State University, Wichita.

[27] Davies, R. M. (1948). A critical study of the Hopkinson Pressure Bar. *Philosophical Transactions of the Royal Society of London. Series A, Mathematical and Physical Sciences*, *240*(821), 375–457. https://doi.org/10.1098/rsta.1948.0001

[28] Kolsky, H. (1949). An investigation of the mechanical properties of materials at very high rates of loading. *Proceedings of the Physical Society. Section B*, *62*(11), 676–700. https://doi.org/10.1088/0370-1301/62/11/302

[29] Kolsky, H. (1964). Stress waves in solids. *Journal of Sound and Vibration*, *1*(1), 88–110. https://doi.org/10.1016/0022-460x(64)90008-2

[30] Krafft, J. M., Sullivan, A. M., & Tipper, C. F. (1954). The effect of static and dynamic loading and temperature on the yield stress of iron and mild steel in compression. *Proceedings of the Royal Society of London. Series A. Mathematical and Physical Sciences*, *221*(1144), 114–127. https://doi.org/10.1098/rspa.1954.0009

[31] Sun, C. T. (2008). Testing methods for dynamic interlaminar fracture toughness of polymeric composites. *Delamination Behaviour of Composites*, 87–116. https://doi.org/10.1201/9781439832677.ch4

[32] Sen, O. (2010). *Analysis of the study of material behavior at impact rates of strain* (thesis). Michigan State University, East Lansing.

[33] Sudheera, Rammohan, Y. S., & Pradeep, M. S. (2018). Split Hopkinson pressure bar apparatus for compression testing: A Review. *Materials Today: Proceedings*, *5*(1), 2824–2829. https://doi.org/10.1016/j.matpr.2018.01.071

[34] *Aluminum 6061-T6; 6061-T651*. MatWeb. (n.d.). Retrieved from http://www.matweb.com/search/DataSheet.aspx?MatGUID=b8d536e0b9b54bd7b69e4124d8f1d20a

[35] ASM. (1990). *Metals Handbook Vol. 2: Properties and Selection: Nonferrous Alloys and Special-Purpose Materials*.

[36] Boyer, H. E., & Gall, T. L. (1985). *Metals Handbook.* American Society for Metals.

[37] Ho, C. Y., Holt, J. M., & Mindlin, H. (1996). *Structural alloys handbook, 1996 edition*. Purdue University, Center for Information and Numerical Data Analysis and Synthesis.

[38] *300M Ultrahigh Strength Steel*. MatWeb. (n.d.). Retrieved from http://www.matweb.com/search/datasheet.aspx?matguid=df0c08b0008749f0b84bf1fa44e49378

[39] *Steel 300M*. Tech Steel & Materials. (n.d.). Retrieved from https://www.techsteel.net/alloy/steel/300m

[40] *300M Alloy Steel*. Dynamic Metals Ltd | Specialist Metal Supplier and Distributer. (n.d.). Retrieved from https://dynamicmetalsltd.com/products/alloy-steel/300m/

[41] Davis, J. R. (1996). *Carbon and Alloy Steels*. ASM International.